Computational studies of electronic and thermal properties of low dimensional materials

DISSERTATION

zur Erlangung des akademischen Grades

Doktoringenieur (Dr.-Ing.)

vorgelegt

der Fakultät Maschinenwesen

der Technischen Universität Dresden

von

M. Sc. Alvaro Gaspar Rodriguez Mendez

Tag der Einreichung: 24. April 2023

Tag der Verteidigung: 16. October 2023

Vorsitzender: Prof. Markus Kästner

Gutachter: Prof. Dr. Gianaurelio Cuniberti

Prof. Dr. Cornelia Breitkopf

Prof. Dr. Vladimiro Mujica

Mitglied: PD. Dr. Vera Hintze

DECLARATION

I hereby declare that the thesis entitled "Computational studies of electronic and thermal properties of low dimensional materials" submitted by me, for the award of the degree of *Doktoringenieur* to Technische Universität Dresden is a record of bonafide work carried out by me under the supervision of Prof. Dr. Gianaurelio Cuniberti, in the Chair Materials Science and Nanotechnology at TU Dresden.

I further declare that the work reported in this thesis has not been submitted and will not be submitted, either in part or in full, for the award of any other degree or diploma in this institute or any other institute or university.

Place: Dresden

Date: 27.02.2023 **Signature of the Candidate**

ABSTRACT

The control of low dimensional materials holds potential for revolutionizing the electronic, thermal, and thermoelectric materials engineering. Through strategic manipulation and optimization of these materials, unique properties can be uncover which enable more efficient and effective materials development. Towards the determination of nanoscale strategies to improve the electronic and phononic devices, computational simulations of modified low dimensional materials have been carried in this research. First, the electronic properties of chemically functionalized phosphorene monolayers are evaluated with spin-polarized Density Functional Theory, as a potential method to tune their electronic properties. The functionalization not only leads to formation of additional states within the semiconducting gap, but also to the emergence of local magnetism. The magnetic ground state and electronic structure are investigated in dependence of molecular coverage, lattice direction of the molecular adsorption and molecule type functionalization. Furthermore, the physical and transport properties of phosphorene grain boundaries under uniaxial strain are evaluated by the use of Density Functional based Tight Binding method in combination with Landauer theory. In both grain boundary types, the electronic bandgap decreases under strain, however, the respective thermal conductance is only weakly affected, despite rather strong changes in the frequency-resolved phonon transmission. The combination of both effects results in an enhancement in the thermoelectric figure of merit in the phosphorene grain boundary systems. Finally, the thermoelectric properties of carbon nanotubes peapod heterostructures are studied and compared to pristine nanotubes using also the Density Functional based Tight Binding method and Landauer theory. It is found that the fullerene encapsulation modifies the electron and phonon transport properties, causing the formation of electronic channels and the suppression of vibrational modes that lead to an improvement of the thermoelectric figure of merit. The results of this thesis highlight the potential of strategic manipulation and optimization of low dimensional materials in improving their unique electronic and thermal properties, revealing promising avenues for improving electronic and phononic devices.

ZUSAMMENFASSUNG

Die Kontrolle niedrigdimensionaler Materialien birgt das Potenzial für eine Revolutionierung der elektronischen, thermischen und thermoelektrischen Technologien. Durch strategische Manipulation und Optimierung dieser Materialien können einzigartige Eigenschaften aufgedeckt werden, die eine effizientere und effektivere Materialentwicklung ermöglichen. Um Strategien im Nanobereich zur Verbesserung elektronischer und phononischer Bauelemente zu ermitteln, wurden in dieser Forschungsarbeit rechnerische Simulationen modifizierter niedrigdimensionaler Materialien durchgeführt. Zunächst werden die elektronischen Eigenschaften von chemisch funktionalisierten Phosphoren-Monoschichten mit Hilfe der spinpolarisierten Dichtefunktionaltheorie als potenzielle Methode zur Abstimmung ihrer elektronischen Eigenschaften bewertet. Die Funktionalisierung führt nicht nur zur Bildung zusätzlicher Zustände innerhalb der halbleitenden Lücke, sondern auch zum Auftreten von lokalem Magnetismus. Der magnetische Grundzustand und die elektronische Struktur werden in Abhängigkeit von der molekularen Bedeckung, der Gitterrichtung der molekularen Adsorption und der Funktionalisierung des Moleküls untersucht. Darüber hinaus werden die Transporteigenschaften von Phosphoren-Korngrenzen unter uniaxialer Belastung mit Hilfe der auf Dichtefunktionen basierenden Tight-Binding-Methode in Kombination mit der Landauer-Theorie untersucht. In beiden Korngrenzentypen nimmt die elektronische Bandlücke unter Dehnung ab, die jeweilige Wärmeleitfähigkeit wird jedoch nur schwach beeinflusst, trotz ziemlich starker Änderungen in der frequenzaufgelösten Phononentransmission. Die Kombination beider Effekte führt zu einer Erhöhung der thermoelektrischen Leistungszahl in den Phosphorkorngrenzensystemen. Schließlich werden die thermoelektrischen Eigenschaften von Kohlenstoffnanoröhren-Peapod-Heterostrukturen untersucht und mit denen von reinen Nanoröhren verglichen, wobei auch die auf Dichtefunktionen basierende Tight-Binding-Methode und die Landauer-Theorie verwendet werden. Es wird festgestellt, dass die Fullereneinkapselung die Elektronen- und Phononentransporteigenschaften modifiziert und die Bildung von elektronischen Kanälen und die Unterdrückung von Schwingungsmoden bewirkt, was zu

einer Verbesserung der thermoelektrischen Leistungszahl führt. Die Ergebnisse dieser Arbeit verdeutlichen das Potenzial der strategischen Manipulation und Optimierung niedrigdimensionaler Materialien zur Verbesserung ihrer einzigartigen elektronischen und thermischen Eigenschaften und zeigen vielversprechende Wege zur Verbesserung elektronischer und phononischer Bauteile auf.

ACKNOWLEDGEMENT

I would like to express my sincere gratitude to Prof. Dr. Gianaurelio Cuniberti, for providing me the position and financial support (IMPRS and Straintronics project) and encouragement throughout my PhD project. Without his admission, I would not have been able to start this journey.

With a deep sense of gratitude, I would like to express my sincere thanks to my day-to-day supervisor, PD. Dr. Rafael Gutierrez, for his tireless efforts in providing me with the necessary resources and feedback to help me carry out my research. His guidance has been instrumental in helping me to stay focused on my research goals and to complete this thesis.

Also I would like to thank my co-supervisor Dr. Arezoo Dianat and collaborator Dr. Leonardo Medrano, for valuable discussions and for providing insightful ideas to keep progressing through the research project.

A special thanks to Sylvi and Grit for their kind support with all the help to go through the PhD-bureaucratic process as well as some other external german processes.

I express my gratitude to my actual and former colleagues David, Elif, Steffen, Solmar, Mayra, Antonis, Huang-Hsiang (Bob), Jonathan, Phil, Alexander K., Antonie, Li, Thomas, Shirong, Antonio, Muhannad, Rafael, Arezoo, Sylvi, Grit, Massimo, Robert, Alexander C. and Nadia, for their company during my time as a PhD student, either for a small talk, doing sports together, taking part into an activity from the institute or sharing the time during lunch. I will treasure all the time that I had in the institute.

I had the opportunity to meet a lot of people during this time and would like to thank them all for their company and support during this time. Specially to Pablo, Gonzalo and Stefan for their great support. Also I thank to Markos, Christian, Alex, Isi, Najmeh, Sahar, Tim, Tobias, Marco, Bart and the other members of the climbing+ group, to Antonis, Daniel, Nacho, Bruno and the rest of the Altemensa/Sports groups, and to Tania, Manik, Eduardo, Marisol, Raul, Luz, Marilyn and other friends back home who constantly showed me their support.

To my family, I owe a debt of gratitude that cannot be fully expressed in words. Their love, encouragement, and unwavering support have sustained me through the ups and downs of this journey. Their belief in me and my abilities has been a constant source of inspiration and motivation. Muchas gracias, los quiero mucho.

Finally, I would like to acknowledge the contributions of the many other individuals who have helped me in various ways along the way. Without their help, this thesis would not have been possible.

Thank you all from the bottom of my heart.

Place: Dresden

Date: 27.02.2023 **Alvaro Gaspar Rodriguez Mendez**

TABLE OF CONTENTS

LIST OF FIGURES

LIST OF ABBREVIATIONS

OD	Zero-Dimensional
1D	One-Dimensional
2D	Two-Dimensional
AC	Armchair
AFM	Anti-Ferromagnetic
BFGS	Broyden-Fletcher-Goldbarf-Shanno
BMS	Bipolar Magnetic Semiconductor
CB	Conduction Bands
CBM	Conduction Band Minimum
CISS	Chiral-Induced Spin Selectivity
CNT	Carbon Nanotube
DFT	Density Functional Theory
DFTB	Density Functional based Tight Binding Theory
DOS	Density of States
FM	Ferromagnetic
GB	Grain Boundaries
GGA	Generalized Gradient Approximation
IP	In-Plane
KS	Kohn-Sham
LCAO	Linear Combination of Atomic Orbitals
LDA	Local Density Approximation

OP	Out-of-Plane
PBE	Perdew-Burke-Ernserhof
PDOS	Projected Density of States
SCC	Self-Consistent redistribution of Mulliken Charges
VB	Valence Bands
VBM	Valence Band Maximum
ZZ	Zigzag

CHAPTER 1

Introduction

1.1 Motivation

In the last decades, there has been a significant increase in interest in the physics and applications of low-dimensional structures, also referred as nanostructures. "Nano" is a greek prefix that means "dwarf" or something of small size and is used to represent one thousand millionth of a unit (1×10^{-9}). Norio Tanaguchi was the first person who used and defined the word "nanotechnology" in 1974 by expressing "nanotechnology mainly consists in the processing of separation, consolidation, and deformation of materials by one atom or one molecule".[1]

But the advent of this topic was previously foreseen as early as in 1959 in the famous lecture "There's Plenty of Room at the Bottom" by Richard Feynman at the California Institute of Technology.[2] In his talk, he gave a vision of manipulating and controlling things on a small scale, beyond the thickness of a human hair, which could be meaningful for explaining strange phenomena that occur in complex situations and, most importantly, it would have a vast number of technical implications. His pioneering contributions in the field earned him the tittle of the father of modern Nanotechnology. A third outstanding figure who have made a signficant contribution to nanotechnology is Eric Drexler, who popularized the concept of molecular nanotechnology and introduced the idea of atomically precise manufacturing of technology, to structure complex structures starting from the molecular level. His first thoughts on the field were published in 1981,[3] where he describes the molecular manipulation and their potential application from a biochemical perspective. In his books "Engines of Creation" and "Nanosystems: Molecular Machinery, Manufacturing and Computation" he provided a detailed analysis of key physical principles, devices and systems necessary for the implementation of atomic and molecular manufacturing.

Following the emergence of this discipline, various techniques for synthesizing nanostructured materials have been developed and grouped into two broad categories: top-down and bottom-up methods.[4, 5] The fomer one reefers to the methods that use as prime resource bulk materials and then breaks down its

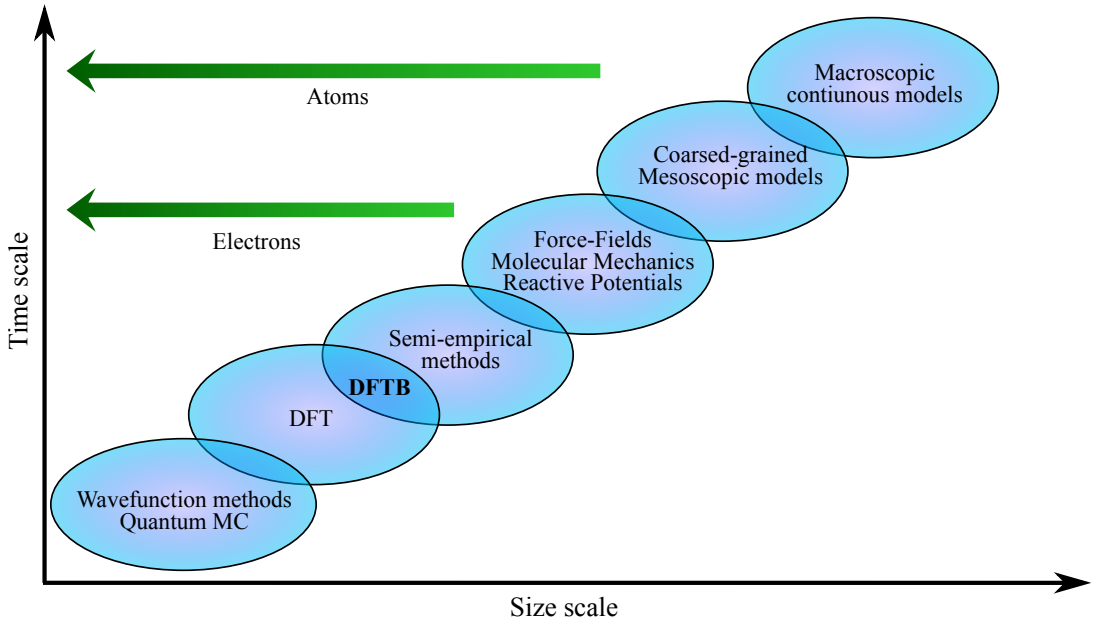

Fig. 1.1 Graphic representation of different computational methods for the study of nanostructured systems across spatial and temporal scales.

structure into nanosized structures or particles. This includes methods such as mechanical exfoliation[6, 7] and lithography.[8, 9] The second category, bottom-up, includes methods with the opposite approach to reach the final product, meaning that the production of nanostructures starts with atoms, molecules or clusters and scale up into the formation of the desired nanomaterials, *e.g.*, sol-gel method[10, 11] or the physical/chemical vapor deposition technique.[12–14] The development and refinement of synthetic methods moves towards generating nanostructured materials with precised control over size, morphology and functionality.

Besides the synthetic route to study novel properties of nanomaterials, high-performance computer simulations, based on mathematical, chemical and physical models, represent a tool in the development, design and understanding of nanostructured systems, even beyond the limits of the experimental work.[15] The widely accessible computational tools to model micro- and nanoscale systems by means of continuum, molecular and quantum mechanics disentangle the gap between the atomic and the macroscopic world, opening up new opportunities in research and technology development. Computational methods have played a critical role in the growth and development of nanotechnology, because they can cover different length and time scales to fit important nanoscale systems and processes (see Figure 1.1).

Starting with ab-initio or first principles quantum mechanical methods, based on the solution of the complex quantum many-body Schrödinger equation, they

provide an accurate description of materials limited to few atoms.[16, 17] The workhorse of current ab-initio simulation methods of nanoscale materials is Density Functional Theory, which is explained with more details in the Chapter 2. Then, for molecular systems between few hundred and thousand atoms, semi-empirical quantum mechanical based methods, such as the tight-binding method, have been developed, providing a bridge between the ab-initio approaches and the classical force-field based methods. The efficiency of this type of methods derives from the fact that they rely on a parametrization of the system's Hamiltonian, considerably increasing the computational speed.[18–20] This topic is briefly explained in the Chapter 2. In the next size scale, when the molecular system reaches over thousand atoms, classical molecular dynamics simulations are employed. The fundamental principle of this type of simulations is to consider the particles as in a classical system, employing Newton's equation of motion to compute the velocity and position of the particles.[21–23] This approach allows exploring the properties of larger molecular systems such as biomolecules, and also to study mechanical and thermal properties of the materials over length scales that cannot be reached by pure quantum mechanical based methodologies.[24] The interaction between the different atom types is implicitly described in many-body force field functions.[25] Different force field sets have been developed to study different type of materials, like the Tersoff potential for carbon systems,[26] the Airebo potential for hydrocarbons,[27] the Embedded Atom Method for metals,[28] and the Stilinger-Weber for semiconductors.[29] A more recent approach, which is gaining considerable relevance in the field of materials discovery and property prediction, is machine learning, which provides a route to scan with high computational speed complex highly dimensional chemical spaces in order to identify specific materials compositions with targeted functionalities. This technique focuses on the use of experimental or ab-initio data and algorithms to construct accurate and computationally low-cost statistical models.[30–33] Common machine learning methods include artificial neural networks,[34, 35] Gaussian regression[36, 37] and decision trees.[38]

As a multidisciplinary field, nanotechnology has gained recognition across various industries due to its potential to enhance and replace or complement existing technologies. Thus, in the medical field, Nanotechnology plays a significant role in the advancement of diagnostic techniques, imaging methods and drug delivery systems. The technology improves detection of pathogens and biological markers related to diseases, as well as it leads to more targeted and efficient treatment through improved drug delivery systems which have a specific focus and reduced likelihood of unintended immune responses.[39] Nanotechnology also has

a significant impact in the improvement of standard construction materials, by developing stronger structures, promoting energy efficiency, and creating surfaces with antibacterial and self-cleaning capabilities.[40, 41] In the area of environmental remediation, nanotechnology offers the potential of developing effective materials for degradation and removal of pollutants and other biological hazards. Materials with enhanced adsorbent capability, catalytic activity or high detection capability can be used as sensors or removal agents of gases, contaminated chemicals, organic pollutants and biological substances.[42] The reduced dimensionality of nanomaterials also offers diverse unusual size-dependent transport properties, which can be employed for the development of materials towards the improvement of energy efficiency and generation, technology miniaturization and heat dissipation. For instance, the emergence of new materials for thermoelectric generators have the potential to improve their performance and make better use of readily available thermal energy that is typically wasted.[43]

Overall, Nanotechnology is a promising field that has the potential to change the world in many positive ways and it has been continuously evolving.

The state of the art of electronic devices is continually advancing, with new technologies and innovations being developed all the time. Some of the most notable recent developments in electronics include foldable and rollable displays, internet of things, 5G networks, artificial intelligence, advance energy-storage technology and quantum computing. The development of nanotechnology in electronics has been driven by several key factors, including the miniaturization of devices through the production of smaller and more compact electronics, the improvement of performance through the creation of more efficient transistors, the extension of battery life through lower power consumption, cost savings through the reduction of materials used in production, the enhancement of functionality and diversification of new device types, and the improved durability due to increased resistance to wear, tear, extreme temperatures, and other environmental factors.[44]

The driving force behind the rapid advancements in technology is driven by Moore's law, which is a prediction made by Gordon Moore in 1965.[45] This law predicts that the number of transistors on a microprocessor, a key component in electronic devices, will double every 18-24 months, and the cost of the transistors will decrease by half during the same period. This prediction has been largely accurate throughout the years, leading to a fast enhancement in the power and reduction in the cost of electronic devices However Moore's Law is facing physical limitation of miniaturization in terms of heat dissipation and power consumption, making it difficult to continue to shrink transistors and improve

performance at the same rate as before. Therefore, research has been carried on alternative technology such as quantum and neuromorphic computing to push the boundaries beyond Moore's Law.[46]

Other branch of science that deals with transport is phononics, which study the manipulation and control of thermal energy on a nanoscale.[47] Phonons are quasiparticles that describe the vibrations of the lattice of a solid and they play a crucial role in many physical phenomena such as thermal conductivity and superconductivity. The state of the art of phononics includes various techniques for manipulating heat, such as thermal metamaterials, phononic crystals, phononic based cooling and nanostructured materials. The interplay between phononics and electronics can converge in a third branch of physics and materials science that also studies transport, known as thermoelectrics. The primary objective of this field is to understand and control the conversion of thermal energy into electrical energy, as well as the reverse process.

The discovery of the Peltier and Seebeck effects led to the development of novel classes of materials and the creation of modern thermoelectric refrigeration and power generation devices. In the Peltier effect, the electrical current flowing through the junction connecting two dissimilar materials will emit or absorb heat at the junction to compensate the difference in the chemical potential between the materials. The Seebeck effect is the reverse phenomenon, in which a gradient of temperature between the two materials of the junction will induce in proportion an electric field, producing a thermoelectric voltage.[48, 49] One current application of this type of materials can be seen in the "Perseverance rover" from the Mars 2020 mission. Perseverance carries a "Multi-Mission Radioisotope Thermoelectric Generator", converting heat from spontaneous radioactive decay of plutonium into electricity.[50] The development of this technology did not happen overnight, however. Researchers have been working for a long time to improve the performance of thermoelectric generators and refrigerators.

Finding a material that would provide a high thermoelectric power and a high ratio of electrical conductivity to thermal conductivity was a challenge, where most of the devices developed were based on semiconductors materials and leaded by alloys of Bi_2Te_3, Bi_2Se_3 and Sb_2Te_3. For 30 years, the development of thermoelectric generators and electronic coolers seemed to have plateaued, until it regained its status as a subject of active research in 1996 after the discovery of the enhanced thermoelectric performance of a two-dimensional (2D) PbTe quantum-well system in comparison to its three-dimensional (3D) counterpart.[51] According to calculations, making a 3D material into a 2D multi-quantum-well superlattice can improve its thermoelectric performance because it increases the

electronic density of states and the scattering of vibrational waves at the boundary between the quantum well and the adjacent barrier of the superlattice. This principle also applies for 3D materials that have poor thermoelectric performance, reducing their dimensionality transforms them into good thermoelectrics. The implementation of low-dimensional systems for thermoelectric applications provide four advantages: the electronic density of states is amplified near the Fermi level, the anisotropic Fermi surfaces can be utilized, the boundary scattering of phonons is increased and the possibility of augmented carrier mobilities when quantum confinement conditions are fulfilled.[52]

1.2 Objectives and outline

The primary aim of this thesis is to exploit different strategies to manipulate the transport properties of low dimensional materials. This is carried out through computational studies of the electronic and phononic transport properties at the level of density functional theory (DFT) and density functional based-tight binding (DFBT) method. The thesis is outlined as follows.

In Chapter 2, the theoretical and computational framework of this thesis is introduced. The electronic structure calculation methods employed in the following chapters, DFT and DFTB, to compute the properties of the systems are described briefly. Additionally the transport calculation method, the atomistic Green's functions, is shortly described to compute the electronic and phononic transport coefficients.

In Chapter 3, the tuning of the electronic structure properties of phosphorene are studied by means of chemical functionalization. The single molecule functionalization, lattice and coverage effects are considered in this study. Then, enantiomeric molecules, D- and L-cysteine, are employed to determine if their chirality can influence the magnetic properties of the system. Finally, the resulting functionalized system is proposed as a bipolar magnetic semiconductor, for which some variables that are characteristic of this class of material are discussed.

In Chapter 4, the study of the low dimensional systems turns into the grain boundary (GB) phosphorene combined by mechanical uniaxial strain. Two specific GB types are used for the calculation of the electronic and thermal transport properties and correlated with their structural changes by the incorporation of the linear defects and the applied strain. This chapter concludes with the discussion of their thermoelectric properties and the thermoelectric figure of merit and potential usage for the design of thermoelectric devices.

In Chapter 5 the electronic and thermal properties of carbon nanotubes (CNT) are studied as hybrid nanomaterials, by hosting fullerene molecules along

their inner cavity. A deeper understanding of how the structural properties of the CNT are affected by the fullerenes is reached, and later, between these two factors, it is determined which one is responsible for the different changes happening in the electronic and thermal transmission. The thermoelectric figure of merit is evaluated and the overall enhancement discussed.

Chapter 6 summarizes and concludes what was achieved in this thesis, it describes open issues, and it proposes an outlook to guide future research in this topic.

CHAPTER 2

Computational Methods

In this chapter, the methodological basis for computing the electronic structure and electronic and thermal transmission functions of the systems studied in subsequent chapters are described. In the first two sections, the methodologies to compute the electronic structure are stated: density functional theory (DFT) and density functional based tight binding (DFTB) method. In the last section of this chapter, the basic equations of Atomistic Green's Functions are explained for the calculation of the electronic and thermal transport.

2.1 Density Functional Theory

The typically used ab-initio method in many computational studies is density functional theory (DFT), which can be described as a theory of electronic ground state structure that is useful for the understanding and the calculation of the ground state density and energy of condensed matter systems. The studied systems range from individual molecules to bulk and complex materials such as proteins and clusters. [53, 54]

In contrast to other ab-initio and semiempirical methods in which the approach leads to calculate molecular wavefunctions, DFT is based on solving the electronic structure of a many-body interacting system through its electron probability density function, also called electron density function ρ.[55] This electron density ρ is the core of DFT and, at difference with other computational methods that depends on the the molecular wavefunction as variable, can be measurable by methods like x-ray diffraction.[56] In the last decades, DFT has become a useful tool for computing the electronic structures of solids for physicists and chemists, either by itself or combined with other methods. Compared against other methods, DFT can be used to perform calculations for small to medium-sized systems on a single computer with standard software packages, reaching up to few hundred atoms, and for larger systems, like solid state materials, DFT calculations are typically performed on supercomputers with high memory and processing power, for which it can be used to study molecular systems with

thousands or ten of thousands of atoms. Other main advantages are that the electronic correlation is computationally less demanding than other ab initio methods like Møller–Plesset second perturbation theory, and the accuracy of the computed results of certain properties, such as energy, charge density and forces on atoms, are reliable, as it has been seen for systems involving d-block atoms, which results are more closely to the experimental values.

To understand better the theoretical background of how this method is based, some preliminary information of basic equations in molecular modelling is reviewed, *e.g.*, the Schrödinger equation and Hamiltonian for a many body particles system. Then it follows up with approximations that simplify the calculation of the systemś energy and describe the main theorems and ansatz of DFT.

2.1.1 The Many-Body System Hamiltonian and the Born-Oppenheimer approximation

The fundamental of the first-principles method in quantum mechanics is condensed in the Hamiltonian of a system, which describes the electrons and atomic nuclei in any situation. The non-relativistic time independent Hamiltonian of a many-body system consisting of nuclei and electrons is expressed as[55]:

$$\begin{aligned} H_{tot} &= -\sum_I \frac{\hbar^2}{2M_I}\nabla^2_{R_I} - \sum_i \frac{\hbar^2}{2m_e}\nabla^2_{r_i} + \frac{1}{2}\sum_{I\neq J}\frac{Z_I Z_J e^2}{|R_I - R_J|} \\ &\quad + \frac{1}{2}\sum_{i\neq j}\frac{e^2}{|r_i - r_j|} - \sum_{I,i}\frac{Z_I e^2}{|R_I - r_i|}, \end{aligned} \tag{2.1}$$

where capital indexes I, J represent the nuclei and small indexes i, j the electrons, $\hbar$ is the reduced Plank constant, M and R and m and r are the masses and positions of the nuclei and electrons, ∇^2 is the Laplacian operator, e is the charge of the electron and Z is the atomic number of the nucleus. The Hamiltonian operator in Eq. (2.1) is composed of kinetic energy and potential energy parts: the first two terms represent the kinetic energy of the nuclei and the electrons, respectively, and the latter three terms correspond to the potential energy of the nucleus-nucleus, electron-electron and nucleus-electron Coulomb interaction.

The energy of a system, E, can be obtained through the solution of the non-relativistic time-independent Schrödinger equation:

$$H_{tot}\Psi(R_I, r_i) = E\Psi(R_I, r_i), \tag{2.2}$$

where $\Psi(R_I, r_i)$ is the total wavefunction of the system. All the information of

a system could be determined by solving the Eq. (2.2) after getting in hand the total wavefunction, from which physical observables could be calculated after applying the appropriate set of operators. However, in practice, even for the simplest molecule, it is impossible to get its solution analytically because of the high correlation between the motions of particles, as it can be seen in the Hamiltonian in Eq. (2.1), which contain pairwise attraction and repulsion terms, implying that particles do not move independently of all the others. The complex nature of the Schrödinger equation and the high computational cost for systems made up of more than one electron makes it almost impossible to obtain the whole description of a molecular system, therefore, some implementations are required to take into consideration to make this problem more approachable. To overcome this difficulty, the Born-Oppenheimer approximation can be invoke.[57]

This approximation takes into consideration the large mass ratio between nuclei and electrons (circa 1800 times), and the consequent velocity difference of each particle type, *i.e.*, electrons move faster than nuclei. Therefore, instead of trying to solve the Schrödinger equation with the Hamiltonian operator for all the particles simultaneously as stated in Eq. (2.1), the calculation can be simplified by computing the electronic energies for fixed nuclear positions. Since it can be assumed that the nuclei have a fixed position, the Eq. (2.1) can be simplified, where the first term corresponding to the kinetic nuclear energy is zero, the third term that concerns the nucleus-nucleus potential interaction becomes constant and the fifth therm, related to the nucleus-electron potential interaction, can be represented as an external potential V_{ext}. These assumptions reduce the electronic Hamiltonian into the following expression:

$$H_{\text{el}} = -\sum_i \frac{\hbar^2}{2m_e}\nabla^2_{r_i} + \frac{1}{2}\sum_{i\neq j}\frac{e^2}{|r_i - r_j|} - V_{ext}. \tag{2.3}$$

Even though the Hamiltonian has been simplified and is only composed of electron-dependant terms, the analytical solution of Eq. (2.3) is still a challenge. Further approximations are required to approach an easy solution for the Schrödinger equation, compute the energy of the system and determine the properties of interest.

2.1.2 Thomas-Fermi-Dirac approximation model

An early approximation to the density functional theory was the Thomas-Fermi model, proposed by the independent work of Llewellyn Thomas and Enrico Fermi in 1927. [58] The Thomas-Fermi model used the electron density $n(r)$ as variable

instead of the molecular wavefunction. So then, the total energy in function of the $n(r)$ of a system under an external potential V_{ext} can computed as:

$$\begin{aligned} E_{TF}[n(r)] &= C_1 \int n(r)^{(5/3)} d^3r + \int V_{ext}(r) n(r) d^3r \\ &\quad + \frac{1}{2} \int \frac{n(r) n(r')}{|r - r'|} d^3r d^3r', \end{aligned} \tag{2.4}$$

where the first term is the local approximation to the kinetic energy with the constant $C_1 = \frac{3}{10}(3\pi^2)^{(2/3)}$, the second term is the electrostatic energy of the nucleus-electron Coulomb interaction and the third term is the classical electrostatic Hartree energy.

This model lacked the contribution of the exchange and correlation among electrons, and failed to described molecules, which, according to the results, they would not be stable and, hence, dissociate in the individual elements.

In 1930 this model was extended by Paul Dirac as:[59]

$$\begin{aligned} E_{TFD}[n(r)] &= C_1 \int n(r)^{(5/3)} d^3r + \int V_{ext}(r) n(r) d^3r + \\ &\quad \frac{1}{2} \int \frac{n(r) n(r')}{|r - r'|} d^3r d^3r' + C_2 \int n(r)^{(4/3)} d^3r, \end{aligned} \tag{2.5}$$

where the last term represents the local exchange, being $C_2 = -\frac{3}{4}(\frac{3}{\pi})^{(1/3)}$. After Dirac's contribution to this model, it became to be known as the Thomas-Fermi-Dirac model.

The ground state density and energy can be computed by minimizing the functional $E[n]$ in Eq. (2.5) for all possible n(r) subject to the constraint on the total number of electrons

$$\int n(r) d^3r = N_e. \tag{2.6}$$

By using the method of Lagrange multiplier it is possible to reach the minimum of energy

$$\delta E_{ETF}[n(r)] - \mu \left(\int n(r) d^3r - N_e \right) = 0, \tag{2.7}$$

where μ is the Lagrange multiplier and physically represents the chemical potential. A variation with respect to the $n(r)$ yields to the solution:

$$\frac{5}{3}C_1 n(r)^{2/3} + V_{ext}(r) + \int \frac{n(r')}{|r-r'|} d^3r' + \frac{4}{3}C_2 n(r)^{1/3} \quad = \quad \mu, \tag{2.8}$$

which is known as the Thomas-Fermi-Dirac equation and determines the equilibrium distribution of the electron density.

The Thomas-Fermi-Dirac approach became very attractive by simplifying the many-body Schrödinger equation that involves 3N degrees of freedom for N_e electrons. Nevertheless, this approach fails by omitting essential physical and chemical properties such as shell structures of atoms and binding of molecules, which, according to some of their approximations, they would not be stable and, hence, dissociate in the individual elements

2.1.3 The Hohenberg-Kohn theorems

The nowadays DFT calculations were set by two main theorems published by P. Hohenberg and W. Kohn in 1964.[60] The goal of such theorems was to formulate DFT as an exact theory of many-body systems in an external potential V_ext and to solve any problem of electrons and fixed nuclei, where the Hamiltonian is expressed as in Eq. (2.3).

The first Hohenberg-Kohn theorem is an existence theorem, which says that all the properties of a ground state electronic system are determined by a functional of the electron density. For instance, the ground state energy, E_0, can be calculated by a functional of the ground state, which can be represented as:

$$F[n(r)] \longrightarrow E_0. \tag{2.9}$$

This theorem is an existence theorem because it states that a functional F exists but does not describe how to find it. Regardless of being the main problem with DFT, it is still significant by itself, since it assures us that there is, in principle, a way to calculate molecular properties from the electron density.

The second Hohenberg-Kohn theorem is a variational theorem, which gives a variation principle for the density functionals, which states that any trial electron density function will give an energy equal (in case of matching the exact true electron density function) or higher than the true ground state energy.

$$E_T[n_t(r)] \geq E_0[n_0(r)]. \tag{2.10}$$

The trial electron density $n_t(r)$ has to satisfy two conditions. The first one that the integral over the space of this trial electron density has to be equivalent to the number of electrons in the electronic system, $\int n_t(r)d^3r = N$, and the second condition declares that the number of electrons can not be negative, $n_t(r) \geq 0$.

In principle, it is possible to keep choosing different trial densities until a pretty low energy is obtained in relation to the other estimations, which means that the approximation is closer to be the correct ground state energy. However, the difficulty of this approach is related to the nature of the functional itself, since the exact functional is unknown. Moreover, a methodology in which the density can be used as an argument in some general characteristic variational equations was not yet suggested, but this changed after the Kohn-Sham theorem.

2.1.4 The Kohn-Sham orbitals equations

The next major step in the development of DFT came up with the derivation of a set of one-electron equations from which the electron density could be obtained.

Considering a system in which paired electrons are described by the same spatial one-electron orbitals, W. Kohn and L.J. Sham proved that the exact ground-state energy of an N electron system can be written as: [61]

$$\begin{aligned} E[n(r)] &= -\frac{\hbar^2}{2m_e}\sum_{i=1}^{N_e}\int \psi_i^*(r_1)\nabla_1^2\psi_i(r_1)dr_1 - j_0\sum_{I=1}^{N_N}\frac{Z_1}{r_{Ii}}n(r_1)dr_1 \\ &\quad + \frac{1}{2}j_0\int\frac{n(r_1)n(r_2)}{r_{12}}dr_1dr_2 + E_{XC}[n(r)], \end{aligned} \tag{2.11}$$

where the one electron spatial orbitals ψ_i are the Kohn-Sham orbitals. The exact ground-state electron density is given by

$$n(r) = \sum_{i=1}^{n}|\psi_i(r)|^2\,. \tag{2.12}$$

where this sum goes over all the occupied Kohn-Sham (KS) orbitals and the the n(r) can be known after the computation of these orbitals.

The first term in Eq. (2.11) represents the kinetic energy of the electrons, the second term represents the electron-nucleus attraction over all N_N nuclei with Z atomic number, the third term represents the Coulomb interaction between the total charge distribution at position r_1 and r_2, and the last term $E_{XC}[n(r)]$ is the exchange-correlation energy of the system, which is a functional of the electron

density and takes into account all non-classical electron-electron interactions. All the previous terms can be known except of the last one and, even though the Hohenberg-Kohn theorems state that the E and E_{XC} must be functionals of the electron density, the exact analytical form is unknown, therefore an approximated expression is used as an alternative.

The Kohn-Sham equation (Eq. (2.11)) can be solved by the variational principle to the electronic energy with the charge density given by Eq. (2.12) and then find the KS orbitals. The the KS equations for the one-electron orbitals get the shaped of:

$$\left\{-\frac{\hbar^2}{2m_3}\nabla_1^2 - j_0\sum_{I=1}^{N_N}\frac{Z_I}{r_{Ii}} + j_0\int\frac{n(r_1)}{r12} + V_{XC}(r_1)\right\}\psi_i(r_1) \;=\; \epsilon_i\psi_i(r_1), \quad (2.13)$$

where ϵ_i are the KS orbital energies and V_{XC} is the exchange-correlation potential, which is the functional derivative of the exchange-correlation energy:

$$V_{XC}[n(r)] \;=\; \frac{\delta E_{XC}[n(r)]}{\delta n(r)}. \quad (2.14)$$

The KS operator depends on the orbitals by the density and must be solved self-consistently. This mathematical approach can be seen similar to the Hartree-Fock equation, but the major difference lies in the fact that the first one includes the electron-electron correlation. This difference reduce the degree of freedom from R^{3N} to R^3. Therefore the resolution of the KS equations is exponentially simpler to compute and more efficient that previous methods. The KS equations can be solved in a self-consistently methodology as follows:

1. Assume an initial testing $n(r)$, typically by using a superposition of atomic densities.

2. Compute V_{XC} as a function of r by using a approximate form for the functional $E_{XC}[n(r)]$.

3. Get an initial set of KS orbitals after solving the KS equations.

4. Use the KS orbitals to compute an improved $n(r)$ as in Eq. (2.12).

5. Compare the computed $n(r)$ with the testing $n(r)$ and determine if the $n(r)$ and E_{XC} converge to within some tolerance.

    - If those values are outside this tolerance range, then this process is repeated.

- If those values are within the tolerance range, the calculation proceeds with the computation of the electronic energy as stated in the Eq. (2.11).

2.1.5 Exchange-correlation functionals

The calculation of the fourth term in the Eq. (2.11), the E_{XC}, is required to be considered since its approximate nature is the main source of error in DFT. The E_{XC} is a functional of the $n(r)$ and it is often split into an exchange functional and a correlation functional. The functional acts as a way to transform $n(r)$ into the exchange-correlation energy E_{XC}, and this one ideally compensates the classical self-repulsion in the charge cloud of $n(r)$ and for the deviation of the kinetic energy of the non-interacting KS electrons from the energy of real electrons. Therefore a proper functional not only handles the exchange and correlation errors, but also self-repulsion and kinetic energy errors. [55, 62]

In the local density approximation (LDA), the exchange correlation functional is defined as:[55]

$$E_{XC}[n(r)] = \int n(r)\epsilon_{XC}[n(r)]dr, \tag{2.15}$$

where ϵ_{XC} is the exchange-correlation energy per electron in a homogeneous electron gas of constant density. Even though Eq. (2.15) is an approximation, it has shown to be very accurate, specially for the prediction of structural properties. On the other hand, this model presented lower accuracy when dealing in systems with varying electron density and that consisted of many molecules.

To treat the inhomogeneous part of the electron density, a non-local correction factor involving the gradient of the $n(r)$ is frequently considered in the E_{XC} from Eq. (2.15). Among the gradient-correct functionals that have been proposed, the LDA with gradient corrections, so called generalized gradient approximation (GGA), yields accurate ground-state bond distances and binding energies.[63] The GGA-DFT procedure is an accurate and efficient method for calculating systems with d-metal complexes.

Other set of exchange-correlation functionals have been developed for use in DFT calculations, such as PBE,[63] BLYP and B3LYP,[64] which names a particular pairing of an exchange functional and a correlation functional, but also represent hybrid DFT calculations that use Hartree-Fock correction with density functional correlation and exchange. DFT has been also employed to study open-shell atoms and molecules, which required an extension of LDA to

this kind of systems by the formulation of the local spin-density approximation. For this approximation, the exchange-correlation energy depends on the spin density, known as the difference between spin-up electron density and the spin-down electron density, as well as the total electron density. This approach has been employed in the study of magnetic structures based on metals and alloys.[65]

2.2 Density Functional Based Tight Binding method

In the previous section the DFT formalism was explained through and it was highlighted how, within the orbital formulation by KS, its efficiency and accuracy makes it a powerful method of choice for electronic structure calculations. An important part that contributed in the success of DFT was the development of the computational resources in the last decades. But when computational resources were modest and DFT calculations landed in low accurate results, other methods were employed for electronic calculation such as classical force fields and tight-binding methods. [66]

Regarding the last one, tight-binding is a method for modeling band structures with one to several fitted hopping parameters and for calculating total energies. But specially for this task, the density functional based tight binding method (DFTB) is designed, which is parametrized directly using DFT, therefore having a deeper base in first principles than other tight-binding methods (see Figure 1.1.[67] Even though DFT is the main choose for electronic calculations, DFTB can be useful in different ways:

1. DFTB can scaled better for larger systems than DFT.

2. DFTB-Molecular Dynamics can be used to study the time evolution of the system for longer time scales compared to DFT.

3. DFTB can be used to pre-scan trends from structural families to subsequently be computed in DFT.

4. Due to the basis with DFTB, method improvements can be carried first in DFTB and quick tested before proceeding to full DFT methods.

5. In learning and teaching, DFTB is simple for and different phenomena can be studied with real-time simulation that can easily run on a laptop.

In this section the DFTB formalism will be briefly introduced, starting with the Tight binding method, then followed by a more detailed DFTB theory description and finishing with the basis of the Slater-Koster.

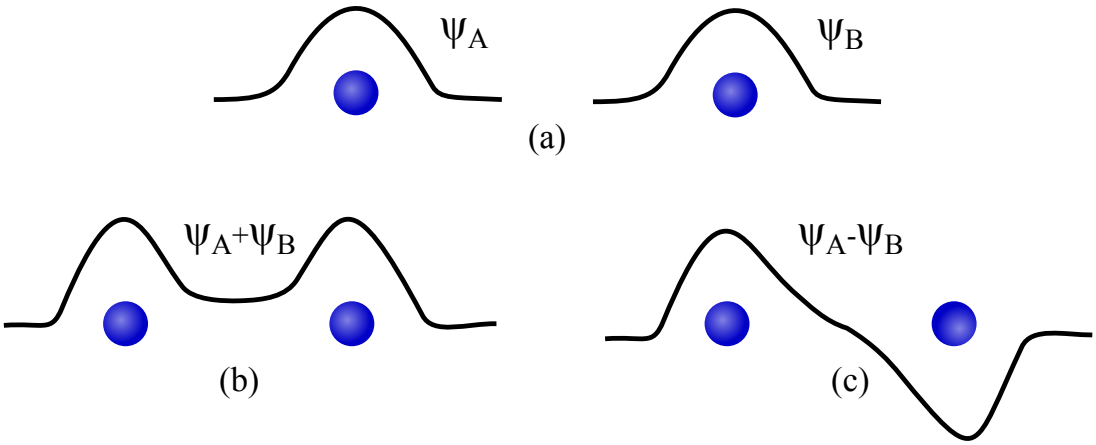

Fig. 2.1 Schematic representation of wavefunctions of electrons on two hydrogen atoms at (a) large separation, (b) ground state closer separation and (c) excited state wavefunction.

2.2.1 Tight-binding formalism

Prior to describe the principles of the DFTB method, a general explanation of the framework of Tight-binding theory is introduced. [68, 69] The description of this model can be initiated by considering two hydrogen atoms, each one with an electron in the 1s state and their corresponding wavefunction ψ_a,ψ_B as depicted in Figure 2.1. Their wavefunctions overlap after bringing closer the atoms, forming two possible combinations $\psi_A \pm \psi_B$ (Figure 2.1 (b) and (c)), where each combination shares an electron with the two protons, but the electron in the $\psi_A + \psi_B$ state has lower energy than the $\psi_A - \psi_B$ state. The electron of the $\psi_A + \psi_B$ state spends part of the time in the region around both protons, which is in the attractive potential of both protons, hence increases the binding energy. On the other hand, the probability of the $\psi_A - \psi_B$ state vanishes midway between the nuclei, which then does not contribute in the binding of the system.

From this is seen that two separated energy levels were formed as two atoms were brought together for each level of the isolated atom. Therefore, for N atoms, N orbitals are formed for each orbital of the isolated atom. The coulomb interaction between the protons an the electrons split the energy levels when the distance between the atoms decreases, which splits the energy levels, spreading them into bands. In each band there is a state of a given quantum number of the free atom, and the band's width is proportional to the strength of the overlap interaction between neighbouring atoms. As this happen for the electrons of s-states, bands are also formed from p, d,... states of the free atoms.

This conjecture that starts out from the wavefunctions of the free atoms is known as the tight-binding or the linear combination of atomic orbitals (LCAO) approximation. In a crystal, the single particle hamiltonian can be taken as

$$H = H_{at} + \Delta U, \tag{2.16}$$

where H_{at} is the hamiltonian of a single atom and ΔU includes all the perturbations between the true potential in the crystal and the potential of an isolated atom. It can be assumed $\Delta U \longrightarrow 0$ at the center of each atom in the crystal. The single particle states in a crystal are $\psi_{nk}(r)$, where the energy-eigenvalues can be found from the time independent Schrödinger equation:

$$H\Psi_{nk}(r) = E_{nk}\Psi_{nk}(r). \tag{2.17}$$

where n is the band index and k is a wavevector in the first Brillouin zone.

The single particle states must follow Bloch's theorem

$$\psi_{nk}(r + T_s) = e^{ik\cdot T_s}\Psi_{nk}(r). \tag{2.18}$$

where T_s is a real space translation vector of the crystal.

A single atomic orbital system does not satisfy Bloch's theorem, but rather this method is employed for systems with periodic potential, *i.e.*, crystals, hence, a linear combination of atomic orbitals can be made as

$$\psi_{nk}(r) = \frac{1}{\sqrt{N}}\sum_{T_s} e^{ik\cdot T_s}\phi_n(r - T_s). \tag{2.19}$$

where N represents the lattice sites in the crystal and the coefficient $1/\sqrt{N}$ ensures that the Bloch states are normalized.

For the calculation of the band structure of a crystal with only s-states (ϕ_s), where a single atom occupies the unit cell and a translation vector T_s is applied, only one band and one Bloch state are present ($n = 1$), this last one can be expressed as:

$$\psi_k(r) = \frac{1}{\sqrt{N}}\sum_{T_s} e^{ik\cdot T_s}\phi_s(r - T_s). \tag{2.20}$$

In means to find the dispersion relation, the expectation value of the energy is calculated,

$$E(k) = \int \psi_k^*(r) H \psi_k(r) dr, \tag{2.21}$$

where the integrals are over all the space. Then substituting Eq. (2.20) in Eq. (2.21) leads to,

$$E(k) = \frac{1}{N} \sum_{T_s} \sum_{T_s''} e^{ik \cdot T_s''} \int \phi_s^*(x_s) H \phi_s(x_s - T_s'') dx_s, \tag{2.22}$$

where $x_s = r - T_s$ was used only as a change of variable and $T_s'' = T_s' - T_s$ is another fixed translation vector. The sum over R gives a factor N which then simplifies the first coefficient. Then, different terms in the sum over T_s'' can be separated by considering the range of the atomic d-orbitals, $\phi_s(r)$. If $T_s'' = 0$, then the integral becomes

$$\int \phi_s^*(x_s) H \phi_s(x_s) dx_s = \epsilon_s \tag{2.23}$$

where ϵ_s is the energy of the atomic s-orbital in an isolated atom. If $|T_s''|$ is too large, the integral will be very similar to zero since the overlap between wavefunctions separated by large T_s'' is very small. Usually, in semi-empirical tight binding calculation, a small $|T_s''|$ is ideally used, for instance, the distance of a translation vector between an atom and its nearest neighbour τ_{nn}. Then

$$E(k) = \epsilon_s + \sum_{\tau_{nn}} e^{ik \cdot \tau_{nn}} \int \phi_s^*(x_s) H \phi_s(x_s - \tau_{nn}) dx_s. \tag{2.24}$$

Finally, through this method, the overlap integral is not only pursued to be solved, but rather to be replaced with a parameter $\gamma_{TB} = \int \phi_s^*(x_s) H \phi_s(x_s - \tau_{nn}) dx_s$, therefore the final expression is stated as

$$E(k) = \epsilon_s + \sum_{\tau_{nn}} e^{ik \cdot \tau_{nn}} \gamma_{TB}(|\tau_{nn}|). \tag{2.25}$$

In the case of a 1D crystal, $\tau_{TB} = \pm a_0 i$, where a_0 is the distance between atoms and corresponds to the lattice constant, and the wavevector $k = ki$ since it is placed along the direction of i. Then the Eq. (2.25) can be rewritten as:

$$E(k) = \epsilon_s + 2\gamma_{TB}(a_0)\cos(ka_0). \quad (2.26)$$

This equation describes how the energy varies with a crystal momentum,k.

Similar approach can be taken for 2D crystals, but for this case there are four vectors: $\tau_{TB} = \pm ai$ and $\tau_{TB} = \pm bi$ that translate to the nearby atoms for significant overlapping integral. Also the wavevector takes the form $k = k_x i + k_y j$ because it varies in both x and y directions. Therefore, Eq. (2.25) can be written as

$$E(k_x, k_y) = \epsilon_s + 2\gamma_{TB}(a)\cos(k_x a) + 2\gamma_{TB}(b)\cos(k_y b). \quad (2.27)$$

2.2.2 From DFT to DFTB

After explaining the formulation of the tight binding model, the base of the DFTB method, the explanation of its adaptation into density functional theory is proceeded. The transition from DFT to DFTB is based on the expansion of the density $n(r) = n_0(r) + \delta n(r)$ around a reference density $n_0(r)$[19, 20]

$$\begin{aligned} E[n(r)] &= E[n_0(r)] + \int \frac{\delta E[n(r)]}{\delta n(r)}\Big|_{n_0} \delta n(r) + \frac{1}{2}\iint \frac{\delta^2 E[n(r)]}{\delta n(r)\delta n(r')}\Big|_{n_0} \delta n(r)\delta n(r')... \\ &\quad + \frac{1}{p!}\iint ... \int \frac{\delta E[n(r')]}{\delta n(r)...\delta n(r^{(p)})}\Big|_{n_0} \delta n(r)...\delta n(r^{(p)}) + ... \end{aligned} \quad (2.28)$$

The superposed density of atoms is taken as starting point $n_0(r)$. A repulsive energy contribution can be defined by collecting only the terms which depend on the $n_0(r)$

$$E^{rep} = E(n_0(r)) - \int \frac{\delta E}{\delta n(r)}\Big|_{n_0} n_0(r) dn(r) \quad (2.29)$$

Using the expression of the Kohn-Sham operator (left side of Eq. (2.13)) the terms that are only depending on the $n(r)$ provide the so-called band-energy, which established the basis for the initial version of DFTB, called DFTB1, which also includes the repulsive term of Eq. (2.29).

$$E^{(1)} = \int \frac{\delta E}{\delta n(r)}\Big|_{n_0} n(r) dn(r) \quad (2.30)$$

DFTB1 is also called sometimes the non-SCC (Self Consistent redistribution of Mulliken Charges) DFTB. The second order dependence upon density fluctuation of the Coulomb and the exchange-correlation energy only appears in the second order term[70]

$$E^{(2)} = \frac{1}{2}\iint\left(\frac{1}{|r-r'|}+\frac{\delta^2 E_{xc}}{\delta n(r)\delta n(r')}\bigg|_{n_0}\right)\delta n(r)\delta n(r')drdr' \quad (2.31)$$

Combining the previous equation, the second order or DFTB2 expansion is defined as

$$\begin{aligned} E^{DFTB2} &= E^{rep}+\sum_i n_i\int\phi_i^* H_0^{KS}\phi_i dr \\ &\quad \frac{1}{2}\iint\left(\frac{1}{|r-r'|}+\frac{\delta^2 E_{xc}}{\delta n(r)\delta n(r')}\bigg|_{n_0}\right)\delta n(r)\delta n(r')drdr', \quad (2.32)\end{aligned}$$

which is also called the self-consistent charge DFTB. The next steps of this method include the expression of molecular orbitals as linear combination of atom orbitals, an approximation by replacing the 3D continuous electronic density by a set of discretized atomic electron populations (Mulliken's charges), and the introduction of the two-electron integrals. These approximations lead to the total DFTB2 energy to be rewritten as

$$E^{DFTB2} = E^{rep}+\sum_i n_i\sum_{a\mu,b\mu}H^0_{a\mu,b\mu}c^i_{a\mu}C^2_{b\mu}+\frac{1}{2}\sum_{a,b}\gamma_a b\Delta q_a\delta q_b, \quad (2.33)$$

where the second term expresses the energy as a linear combination of atomic orbitals, in last term γ_{ab} represents the pair-wise electron integrals, and $\Delta q_{a,b}$ represents the atomic charges fluctuation with respect to the atomic neutral references, which describe the electrostatic situation.

The earlier extensions were even consistently improved with a more accurate Coulomb interaction between atomic partial charges and a complete third-order expansion of the DFT total energy.[71]

$$E^3 = \frac{1}{6}\iiint\frac{\delta^3 E^{xc}[n(r)]}{\delta n(r)\delta n(r')\delta n(r')}\bigg|_{n_0(r)}\delta n(r)\delta n(r')\delta n(r'')drdr'dr''. \quad (2.34)$$

DFTB3 has shown an additional flexibility and better proton affinities for systems involving C, H, O, N, P and other elements relevant for calculations

that includes a gas phase or in solvents.

2.2.3 Parametrization

There are two parts of the DFTB parameters, the necessary parameters of the electronic part of the DFTB model and two-body force field like term that correspond to the parameters that conform the repulsive energy contribution.[67] With the assistance of DFT calculations in means of LDA or GGA functionals, the matrix elements H^{KS} can be parametrized. This starts with the atomic calculations to determine the atomic KS orbitals $\phi_{a\mu}$ and eigenvalues $\epsilon_{a\mu}$

$$H^{KS}_{a\mu,a\mu} = \epsilon_{a\mu}. \tag{2.35}$$

The above atomic orbitals can provide the LCAO basis to span the DFTB Hamiltonian, but these atomic orbitals are constrained by a confinement potential under the form

$$v^{con} = \left(\frac{r}{r_0}\right)^m. \tag{2.36}$$

This confinement potential can produce better transferability. Then, the resolution of the KS equations in the presence of the confinement potential defines the corresponding confined atomic orbitals $\tilde{\phi}_{a\mu}$, which later are used for the actual DFTB/LCAO basis set.

The on-site second order contributions γ_{aa} are computed as

$$\gamma_{aa} = U_a = IP(a) - EA(a), \tag{2.37}$$

where U_a is the Hubbard parameter, which is calculated as the difference between the first ionization potential ($IP(a)$) and the electron affinity ($EA(a)$). The two-center integrals γ_{ab} (where a $\neq$ b) are calculated via an analytical damped Coulomb formula

$$\gamma_{ab} = \frac{1}{R_{ab}} - f(U_a, Ub, R_{ab}), \tag{2.38}$$

which depends on the individual on-site integrals U_a and U_b

Moving to the second part of the parametrization, the repulsive term, this is

certainly the most delicate. This term, for a given pair of atoms, is calculated as

$$u_{ab}^{rep}(R_{ab}) \quad = \quad \Delta E_{ab}^{DFT}(R_{ab}) - \Delta E_{ab}^{DFTB(elec)}(R_{ab}), \tag{2.39}$$

where the repulsive term (U_{ab}) is determined as the difference between the purely electronic DFTB contribution to the interaction energy ($\Delta E_{ab}^{DFTB(elec)}$) and the total DFT interaction energy (ΔE_{ab}^{DFT}) of the given atomic pair.

The main parameters sets available for a wide range of molecular compounds are the mio set,[71] the matsci set,[72] the 3ob set,[73] and the pbc set[74].

2.3 Atomistic Green's functions

Leaving the theoretical background of the electronic structure calculation methods, the focus of this section moves on to the mathematical definitions of the transport method employed along this project, the atomistic Green's functions technique. Below the non-equilibrium Green's function formalism is briefly described. For a more detailed description of the formalism, the book in Quantum transport by S. Datta is suggested for reviewing.[75] In this section the formalism applied for computing the electronic transmission as well as thermal transmission of nanometric systems are outlined in the ballistic regime.

2.3.1 Non-Equilibrium Green's functions for modeling electronic transmission

In the early 1960's, the first developments of the non-equilibrium Green's functions took place, which came as a powerful framework to calculate physical observables in non-equilibrium many particle systems. The Green's function formalism is a useful tool to approximate the interactions of larger bulk system with a finite device both in and out of equilibrium. This method can be employed for different study cases, such as the determination of voltage drop and electron current trough an atomic system under a bias voltage, as well as the characterization of electronic transmission through a device between two contacts. To do so, this formalism uses a many-body concept that is commonly employed to describe complicated interaction, known as the self-energy. The self-energy partitions a finite device from an infinite bulk region, hence the retarded Green's function of a device can be written as

$$G_d(E) \quad = \quad [(E + i\eta)S_d - H_d - \Sigma_d(E)]^{-1}, \tag{2.40}$$

where $\Sigma_d(E)$ is the self-energy, S_d is the device overlap matrix, H_d is the device Hamiltonian matrix and η is a small positive constant that represents the extraction of electrons from the contact.

Assuming that a device is connected to an infinite contact, the hamiltonian H, overlap matrices S and Green's functions for the whole system can be written as

$$H = \begin{bmatrix} H_d & H_{dc} \\ H_{cd} & H_c \end{bmatrix}, S = \begin{bmatrix} S_d & S_{dc} \\ S_{cd} & S_c \end{bmatrix}, G(E) = \begin{bmatrix} G_d(E) & G_{dc}(E) \\ G_{cd}(E) & G_c(E) \end{bmatrix}, \tag{2.41}$$

where H_c and S_c are the contact Hamiltonian and overlap matrices, and $H_{dc} = H_{cd}^{\dagger}$ and $S_{dc} = S_{cd}^{\dagger}$ are coupling matrices between the contact and the device. Then, parting from the following equation

$$[(E + i\eta)S - H]G(E) \;\; = \;\; [I], \tag{2.42}$$

and using matrix algebra, the following expression for the self-energy is achieved

$$\Sigma_d(E) \;\; = \;\; \tau_{dc} G_c(E) \tau_{dc}^{\dagger}, \tag{2.43}$$

where $\tau_{dc} = [(E + i\eta)S_{dc} - H_{dc}]$ is the definition of the coupling, and $\Sigma_d(E)$ usually encodes the electronic structure of both the semi-infinite reservoirs and the reservoir-central region interface. This approximation makes simple the calculations since the dimensions of the matrices are the same. But that is yet not the case for the Green's function of the contact $G_c(E)$, which consists on a semi-infinite matrix and requires some mathematical treatment beforehand. To solve this, for instance, recursive algorithm based on Fourirer transformation can be used to achieve the inversion, as described here[76] (for the sake of simplicity, the mathematical details have been omitted, however, for a more thorough understanding, consulting the provided reference is recommended).

In the same way, self-energies can be introduced for the whole system considering both contacts

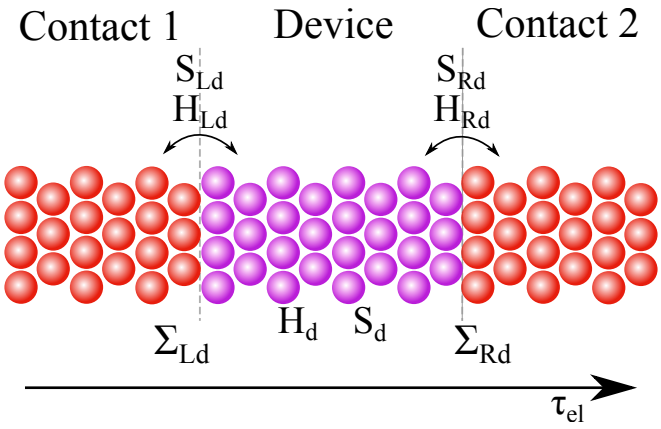

Fig. 2.2 Schematic representation of the contact-device-contact system.

$$
\begin{aligned}
G_d(E) &= [(E+i\eta)S_d - H_d - -\Sigma_{Ld}(E) - \Sigma_{Rd}(E)]^{-1}, && (2.44)\\
\Sigma_{Rd}(E) &= \tau_{Rd}(E)G_R(E)\tau^{\dagger}_{Rd}(E), && (2.45)\\
\Sigma_{Ld}(E) &= \tau^{\dagger}_{Ld}(E)G_R(E)\tau_{Ld}(E), && (2.46)\\
\tau_{Ld,Rd}(E) &= [(E+i\eta)S_{Ld,Rd}([\vec{k}]) - H_{Ld,Rd}([\vec{k}])], && (2.47)
\end{aligned}
$$

where the indexes L and R correspond to the left and right contacts respectively (see fig. 2.2). The typical partitioning of an atomic system for transport calculations consists on a device region that is connected to two contacts or reservoirs. The density matrix $[n(r)]$ in the device, under equilibrium conditions, can be calculated as an integral over the occupied states

$$
[n(r)] = \frac{1}{\pi}\int_{-\infty}^{\infty} A_d(E)f(E-\mu)dE, \qquad (2.48)
$$

where $A_d(E) = i(G_d - G_d^{\dagger})$ is the spectral function and is composed of the imaginary part of the device Green's function. The density of the states (DOS) for the device can be extracted from the spectral function as follow

$$
DOS(E) = \frac{1}{\pi}\mathrm{Trace}[A_d(E)S_d]. \qquad (2.49)
$$

The DOS describe the number of energy eigenstates per unit energy range. The projected density of states (PDOS) for a set of atomic orbitals, from index j to index k, centered on a section of the device can be calculated as

$$PDOS(E) = \frac{1}{\pi}\sum_{i=j}^{k}[A_d(E)S_d]_{ii}. \quad (2.50)$$

where $j \leq k \leq N_O$, and N_O represent the total number of device orbitals.

On the other hand, the density matrix of the device out of equilibrium must involve the fermi-occupations of each contact

$$[n(r)] = \frac{1}{\pi}\int_{-\infty}^{\infty} A_L(E)f(E-\mu_L) + A_R(E)f(E-\mu_R)dE, \quad (2.51)$$

where A_L and A_R are the left and right contact spectral functions. The Fermi function is defined as

$$f(E-\mu) = \frac{1}{q + e^{(E-\mu)/k_BT}}, \quad (2.52)$$

and the contact spectral functions are defined as

$$A_{L/R} = G_d\Gamma_{L/R}G_d^{\dagger}, \quad (2.53)$$

where $\Gamma_{L/R}$ represent the broadening functions of the left/right contacts, also known as reservoir spectral densities, and are equal to its anti-hermitian component:

$$\Gamma_{L/R} = i(\Sigma_{Ld/Rd} - \Sigma_{Ld/Rd}^{\dagger}), \quad (2.54)$$

If $\mu_L = \mu_R$ in the non-equilibrium spectral function integral, then the expression gets reduced to the equilibrium spectral function integral. Hence, to solve the non-equilibrium electron density, the self consistent cycle must require that $\mu_L \neq \mu_R$.

In the end, the calculation of the electronic transmission (τ_{el} through the device at a given energy can be defined as

$$\tau_{\text{el}}(E) = \text{Trace}\big[\Gamma_L G_d \Gamma_R G_d^{\dagger}\big]. \quad (2.55)$$

After measuring the electronic transmission through the device, the total

current between the non-equilibrium electrochemical potentials is given by

$$I = \frac{2q}{h}\int_{\infty}^{\infty}\tau_{\mathrm{el}}(E)[f(E-\mu_L)-f(E-\mu_R)]. \tag{2.56}$$

This expression is just an energy integral over the transmission spectrum bordered by the sample and tip Fermi functions.

2.3.2 Non-equilibrium Green's function for modeling thermal transmission

The study of phonon transport across interfaces, from a theoretical and experimental perspective, has become an important part in the research on nanoscale thermal transport. Influenced by the constant miniaturization of device size to submicron length scales, the understanding of heat transfer across interfaces and boundaries has become critical to application such as the design of phononic devices for thermal interfaces and thermoelectric materials. The Green's function method is an atomistic technique that can be used to also study phonon transport across interfaces. This technique was pioneered by Mingo and Yang in the computation of phonon transport in Si nanowires covered by an amorphous material. [77] This method neglects anharmonic phonon processes, although it can be included by an extension that requires more mathematical formulation than the basic harmonic model. Nevertheless, a previous work has shown that anharmonic scattering can be neglected at room temperature if the characteristic device length is no longer than 20 nm. [77]. Afterwards, several studies have been carried by assuming the system has only harmonic interactions.

The Green's functions method for thermal transmission is founded on a harmonic matrix (K_H) for the system of interest, where its mathematical definition is[78]

$$K_H = \frac{1}{\sqrt{M_p M_q}}\begin{cases} -\frac{\delta^2 U}{\delta u_p \delta u_q} & if p \neq q \\ -\sum_{m\neq q}\frac{\delta^2 U}{\delta u_q \delta u_m} & if p = q \end{cases} \tag{2.57}$$

where $u_{p/q}$ refer to any two atomic vibrational degrees of freedom, U is the total interatomic potential, $M_{p/q}$ are the atomic masses associated with the degrees of freedom $u_{p/q}$ respectively. The dynamical equation can be written as

$$(\omega^2 I - K_H)\tilde{u} = 0, \tag{2.58}$$

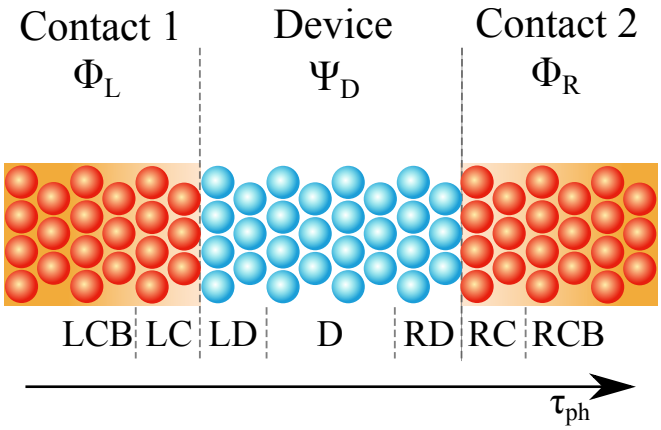

Fig. 2.3 Schematic representation of the contact-device-contact setup for the phonon transmission calculation. Contact 1 includes atom groups LCB and LC, Contact 2 includes atom groups RCB and RC, and Device include atom groups LD, D and RD. Both contacts are two semi infinite thermal reservoirs at constant temperatures T_1 and T_2 and its geometry has to fulfill a periodicity requirement. The geometry of the device region is arbitrary. A column vector Ψ_D represents vibrational degrees of freedom in the device, while $\Phi_{L/R}$ represents vibrational degrees of freedom in left/right contact.

where $\tilde{u}$ is a column vector consisting of vibrational degrees of freedom. Even though the assembled harmonic matrix can contain complex entries, it is always a Hermitian matrix and, therefore, it has only real eigenvalues.

The number of degrees of freedom in the contact approaches infinity, therefore a sufficiently large number n_c is required to approximate the number of degrees of freedom in the contact. On the other hand, the number of degrees of freedom in the device n_d is finite. For the interface, the number of degrees of freedom (LC,LD,RC and RD in figure 2.3) is n_{cd}. Based on Eq. (2.58), the dynamical matrix for the disconnected contacts are defined as

$$(\omega^2 I - K_{HL/HR})\Phi^{\Upsilon}_{L/R} \;=\; 0, \tag{2.59}$$

where $K_{HL/HR}$ are the states for the harmonic matrices of the left and right contacts, and the superscript Υ refers to the disconnected state. The dynamical equation of the connected system (contacts + device) is

$$\begin{bmatrix} \omega^2 I - K_{HL} & -\tau^{\dagger}_{Ld} & 0 \\ -\tau_{Ld} & \omega^2 I - K_{Hd} & -\tau_{Rd} \\ 0 & -\tau^{\dagger}_{Rd} & \omega^2 I - K_{HR} \end{bmatrix} \begin{Bmatrix} \Phi^{\Upsilon}_{L} + \chi_L \\ \psi_d \\ \Phi^{\Upsilon}_{R} + \chi_R \end{Bmatrix} \;=\; 0, \tag{2.60}$$

where $\chi_{L/R}$ changes the original disconnected contact vector to the connected

state to the device, $\tau_{Ld/Rd}$ is the connection matrix between the left or right contact and the device (same principle as in 2.3.1). The solutions to the previous equation can be written as

$$\chi_L = g_L \tau_L d^\dagger \psi_d, \tag{2.61}$$
$$\chi_R = g_R \tau_R d^\dagger \psi_d, \tag{2.62}$$
$$\psi_d = GS. \tag{2.63}$$

The matrices $g_{L/R}$ correspond to the uncoupled Green's functions of their respective contacts and are defined as

$$g_L = \lim_{\delta \longrightarrow 0} [(\omega^2 + \delta i)I - K_{HL}]^{-1}, \tag{2.64}$$
$$g_R = \lim_{\delta \longrightarrow 0} [(\omega^2 + \delta i)I - K_{HR}]^{-1}, \tag{2.65}$$

where δ is a perturbation that correspond to phonon energy dissipation in contacts. The green's function matrix G and source matrix S are defined as

$$G = \left[\omega^2 I - K_{Hd} - \tau_{Ld} g_L \tau_{Ld}^\dagger - \tau_{Rd} g_R \tau_{Rd}^\dagger\right], \tag{2.66}$$
$$S = \tau_{Ld} \Phi_L^\Upsilon + \tau_{Rd} \Phi_R^\Upsilon = S_L + S_R. \tag{2.67}$$

The energy related with any degree of freedom has a kinetic and potential energy components,

$$E_p = \frac{1}{4} \sum_q (u_p^* k_{pq} u_q + u_q^* k_{qp} u_p) + \frac{M_p}{2} \dot{u}_q^* \dot{u}_p^*, \tag{2.68}$$

where

$$k_{pq} = K_{Hpq} \sqrt{M_p M_q}, \tag{2.69}$$

By employing the time derivative and Newton's second law, the energy flux between any two degrees of freedom is derived and has the following form

$$J_{pq} = \frac{\omega}{2i} [\phi_p^* K_{Hpq} \phi_q - \phi_q^* K_{Hqp} \phi_p], \tag{2.70}$$

where $\phi_{p/q}$ are complex wave functions with no time dependence.

The normalization condition for phonons, by using Eq. (2.68) and the degree of freedom $u_{p/q} = \phi_{p/q} e^{iwt}/\sqrt{M_{p/q}}$, can take the form

$$\hbar\omega = \sum_p \left[\frac{1}{4} \sum_q (u_p^* k_{pq} u_q + u_q^* k_{qp} u_p) + \frac{M_p}{2} \dot{u}_q^* \dot{u}_p^* \right] = \omega^2 |\phi_p|^2, \quad (2.71)$$

Therefore, $\sum_p |\phi_p|^2 = \hbar/\omega$.

The total energy flux of the system is the summation of fluxes between individual degrees of freedom by using Eq. (2.70). In the connected system, the heat flux between Contact 1 and Device can be expressed as

$$\begin{aligned} J_1 = & \frac{\omega \text{Trace}[\psi_d^\dagger \tau_{Ld} \Phi_L^\Upsilon - \Phi_L^{\Upsilon\dagger} \tau_{Ld}^\dagger \psi_d]}{21} \\ & - \frac{\omega \text{Trace}[\chi_d^\dagger \tau_{Ld} \Phi_L^\Upsilon - \Phi_L^{\Upsilon\dagger} \tau_{Ld}^\dagger \chi]}{21}, \end{aligned} \quad (2.72)$$

The inflow can be computed by using the Eqs. (2.61), (2.62), (2.63) and (2.67) as

$$\text{Inflow} = \frac{\omega \text{Trace}[S^\dagger G^\dagger S_L - S_L^\dagger G S]}{2i} = \frac{\omega \text{Trace}[S_L S_L^\dagger A]}{2}, \quad (2.73)$$

where $A = G\Gamma_L G^\dagger + G\Gamma_R G^\dagger = A_1 + A_2$ is a matrix defined by convenience to group together the Green's functions. Considering the normalization condition in Eq. (2.71), the number of phonons can be expressed in terms of A_1 as

$$\omega \Phi_L^{\Upsilon\dagger} \Phi_L^\Upsilon \Rightarrow \int \frac{\hbar}{2\pi} N_1(\epsilon_\omega) A_1 d\epsilon_\omega, \quad (2.74)$$

where $\epsilon_\omega = \omega^2$. So then

$$\omega S_L S_L^\dagger = \omega \tau_L d \Phi_L^\Upsilon \Phi_L^{\Upsilon\dagger} = \int \frac{\hbar}{2\pi} N_L(\epsilon_\omega) \Gamma_L d\epsilon_\omega, \quad (2.75)$$

where $N_L(\epsilon_\omega)$ is the number of phonons in Contact 1 at the eigenstate ϵ_ω. Combining previous equation with Eq. (2.73), the inflow in terms of number of phonons can be calculated as

$$\text{Inflow} \;=\; \int \frac{\hbar\omega}{2\pi} N_L(\omega)\text{Trace}(\Gamma_L A)d\omega. \tag{2.76}$$

In similar way, but by using Eqs. (2.72), (2.63) and (2.67), the outflow equation can be expressed in terms of number of phonons as

$$\text{Outflow} \;=\; \int \frac{\hbar\omega}{2\pi}\text{Trace}[N_L(\omega)A_L\Gamma_L + N_R(\omega)A_R\Gamma_L]d\omega. \tag{2.77}$$

Proceeding with the substitution of the inflow and outflow from Eqs. (2.76) and (2.77) into Eq. (2.72) The total energy flux between Contact 1 and Device is

$$\begin{aligned} J_1 &= \int \frac{\hbar\omega}{2\pi}\{\text{Trace}[\Gamma_L A]N_L(\omega) - \text{Trace}[N_L(\omega)A_L\Gamma_L + N_R(\omega)A_R\Gamma_L]\}d\omega \\ &= \int \frac{\hbar\omega}{2\pi}[\Gamma_L G\Gamma_R G^\dagger][N_L(\omega) - N_R(\omega)]d\omega. \end{aligned} \tag{2.78}$$

In the same way, the total energy flux between Contact 2 and Device can be calculated as

$$J_2 \;=\; \int \frac{\hbar\omega}{2\pi}[\Gamma_R G\Gamma_L G^\dagger][N_R(\omega) - N_L(\omega)]d\omega. \tag{2.79}$$

Considering that at steady state, $J_1 = -J_2$, the heat flux can be expressed in the Landauer form as

$$J \;=\; \int \frac{\hbar\omega}{2\pi}\tau_{\text{ph}}(\omega)[[N_R(\omega) - N_L(\omega)]d\omega, \tag{2.80}$$

where τ_{ph} is the transmission function of phonons in the systems and it is expressed as

$$\tau_{\text{ph}} \;=\; \text{Trace}[\Gamma_L G\Gamma_R G^\dagger] = [\Gamma_R G\Gamma_L G^\dagger]. \tag{2.81}$$

The transmission function and the heat flux of the system can be used to calculate the thermal conductance, which is defined as

$$\kappa_{\mathrm{ph}} = \lim_{\Delta T \Rightarrow 0} \frac{J}{\Delta T}, \tag{2.82}$$

where ΔT is the temperature difference between both contacts. Then, by linearly expanding the phononic thermal current in that temperature range ΔT, thermal conductance can be expressed as

$$\kappa_{\mathrm{ph}} = \frac{1}{2\pi} \int_0^\infty \hbar\omega \frac{dN_B}{dT} \tau_{\mathrm{ph}}(\omega) d\omega, \tag{2.83}$$

where N_B is the Bose-Einstein distribution function.

Some relevant thermal properties such as in-plane and out-of-plane thermal conductivity or phonon transmission can be calculated as the sum of the individual elements $(\tau_{\mathrm{ph}}, \kappa_{\mathrm{ph}})_{total} = (\tau_{\mathrm{ph}}, \kappa_{\mathrm{ph}})_{in} + (\tau_{\mathrm{ph}}, \kappa_{\mathrm{ph}})_{out}$.

CHAPTER 3

Tuning the electronic and magnetic properties through chemical functionalization

Functionalization of low dimensional systems is an approach used for modifying their properties to make them excel beyond their ground state, or to counter their drawbacks. In this chapter, chemical functionalization is addressed to induce changes in the electronic and magnetic properties of a two dimensional (2D) system, phosphorene, studied by spin polarized DFT simulations. This chapter discusses the impact of functionalization on electronic structure, specifically focusing on the effects of single molecule, lattice direction, and coverage, as well as the induced magnetism in the system. The magnetic effect of chiral molecules functionalized in phosphorene is also computed and discussed. Even though the transport calculations are not stated in this chapter, relevant changes in the properties of this materials will be addressed that can be relevant for the further development of transport devices in the electronic and spintronic fields.

3.1 Introduction

3.1.1 Black phosphorus as a 2D material

Since the discovery of graphene by mechanical exfoliation in 2004 [79], there has been an accelerated search for novel two-dimensional (2D) materials, motivated by their exceptional physical and chemical properties which are related to the strong quantum confinement originated by the reduced spatial dimensionality.[80–84] The exploration of 2D materials has been carried by experimental and computational methodologies, which has open the path to develop new materials with potential applications in various fields such as electronics, thermoelectrics and spintronics. [85–88]

Among the investigated 2D materials, the mono- and few-layers version of black phosphorus, known as phosphorene, has become a promising candidate for designing electronic and optoelectronic devices due to their mechanical flexibility, tunable direct bandgap, anisotropic electronic structure and transport

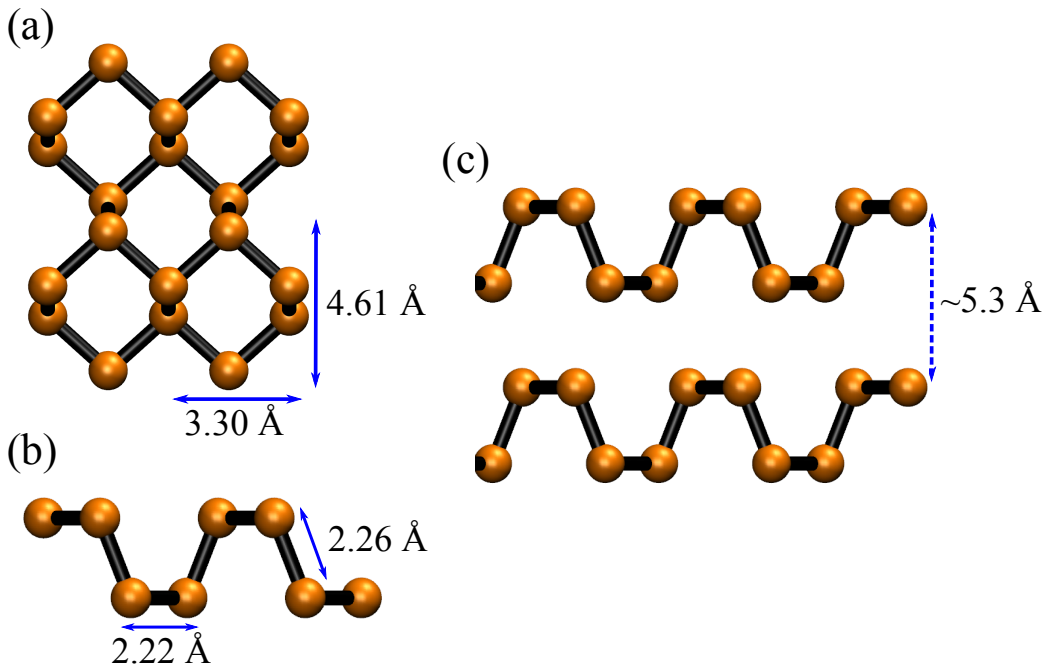

Fig. 3.1 (a) Top and (b) side perspectives of phosphorene monolayer with their corresponding lattice parameters and bond lengths. (c) Side perspective of bilayer phosphorene where the interlayer distance is indicated.

properties.[89, 90] This material was successfully exfoliated in 2014 from bulk black phosphorus, which is the most stable alotropic form of phosphorus. [91]

Phosphorene is composed of phosphorus atoms with sp^3 hybridization, producing a quasi-tetragonal geometry. Each phosphorus atom bonds covalently to two atoms in the same plane and to a third one out of plane, remaining with a non bonding electronic pair. The bond angles between phosphorus atoms are 96.34° and 103.09°, which are very close to the angle of a perfect tetragonal structure, while the lone pair point out of the layer at an angle of $\sim 45°$. This bond arrangement generates its characteristic crystalline puckered non-planar structure, where a single layer resembles a quasi-two layered material of phosphorus atoms. This structure type sets it aside from most of 2D materials, like graphene, boron nitride and transition metal dichalcogenides, which have hexagonal planar structures. The structure of phosphorene is orthorombic (see Figure 3.1) that, from a top perspective, the armchair and zigzag direction can be identified. [92, 93]

Compared with other systems like graphene which has a zero bandgap,[94] or the featured large bandgap of transition metal dichalcogenides,[95] bulk layered phosphorus has a direct bandgap at the Γ point of 0.3 eV, which increases in mono- and few-layered phosphorene up to 2.0 eV.[96–99] From an optoelectronic point of view, the direct bandgap conservation regardless the number of layers of phosphorene represents an advantage because it is experimentally easier to fabricate few-layered instead of monolayered phosphorene. Moreover, the

thickness-dependent bandgap allows the fabrication of devices that vary the optical working range of the electromagnetic spectrum, covering a large region from the visible spectrum down to the middle infrared.[100]

One of the factors that got phosphorene into the attention of the scientific community is its large carrier mobility. This increases in proportion to the number of layers up to a thickness of about ∼10 nm, reaching values exceeding 1,000 $cm^2\ V^{-1}s^{-1}$ along the zigzag direction. Previous studies have shown that the hole mobility reach values of up to 10,000-26,000 $cm^2\ V^{-1}s^{-1}$ for the monolayered phosphorene and up to 4,800-6,400 $cm^2\ V^{-1}s^{-1}$ for the few-layered phosphorene. [90, 101]

But a major drawback of phosphorene comes from the presence of non-bonding electronic pairs, which strongly react with oxygen or water molecules from the environment, causing the oxidation of phosphorus atoms which leads to structural degradation and change of properties. To redeem this situation, previous experimental investigations have developed different methodologies for phosphorene and other 2D materials to improve their environmental stability. Some of these methods involve doping,[102] plasma treatment,[103] chemical intercalation [104] and chemical functionalization.[105–108]

3.1.2 Chemical Functionalization of low dimensional systems

Functionalization of low dimensional materials have a more crucial effect than in conventional bulk materials due to the large surface-volume ratio. It also plays a very important and rapid role to improve their versatility and keep moving the research in the field. The introduction of foreign molecules with functional units into the nanomaterials has proven to be a powerful method to prevent their aggregation in solvents,[109] improve their wettability,[110] improve their environmental stability,[107] tune their physicochemical properties[111] and introduce them new properties that are far from their intrinsic nature.[112, 113]

Chemical functionalization can be classified into two main types in function of the type of interaction: (i) non-covalent interaction, by physisorption of the functional molecules through electrostatic, π-π or hydrophobic interactions, and (ii) covalent interactions, by direct bonding of the functional molecules on the surface of the nanomaterial. Each type of functionalization leads to a change in the properties of the nanomaterial in different perspective. Non-covalent functionalization does not modify its structure and conducts the preservation of most of its intrinsic properties, but its stability requires major attention. On the other hand, covalent functionalization results in a more stable structure and increased range of opportunities to tune their physicochemical properties, but also has as

a result a structural alteration which demands a higher control of the functionalization degree.

Besides the functionalization type, there are other important aspects to consider in the process of functionalization of nanomaterials. One of the is the functionalization site, which is a critical factor because different reaction sites demand different reaction mechanism between the functional groups and the nanomaterial. Some of these sites are grain boundaries, edges and vacancy defects. Other important aspect to consider is the type of functional group to use for the functionalization of the system. To determine this, one has to consider the type of functionalization desired, the chemical nature of the atoms of the surface and of the functional group, and the desire effect to induce after functionalization. [114]

3.1.3 Bipolar Magnetic Semiconductors

Spintronics is an emerging field for the next generation of nanoelectronic devices that, in comparison to conventional electronics, takes use of an additional degree of freedom of the electron, its spin.[115] To improve the performance of spintronic devices, there are several challenges that have to be taken into account, like including spin-polarized carrier injection, long-distance transport and high efficiency spin manipulation. Different classes of spintronic materials have been studied and develop to accomplish devices that can fulfill the first two challenges, like half-metals, diluted magnetic semiconductors and spin gapless semiconductors, but the spin manipulation has not been achieved without having to rely upon an external magnetic field.[116, 117] However, a new class of spintronic materials was defined in a theoretical study of semi-hydrogenated single wall carbon nanotube by Li's group in 2012, which can be the solution to the last problem of spintronic devices. This kind of materials were defined as bipolar magnetic semiconductors (BMS). [118]

In BMS, the valence bands (VB) and conduction bands (CB) approach the Fermi level through opposite spin channels. Therefore, they can provide full spin-polarized currents by applying a gate voltage (V_G) that shifts the Fermi level either to spin-up or spin-down density of states (see Figure 3.2). Three energy parameters ($\Delta 1$, $\Delta 2$, $\Delta 3$) were determined to describe a BMS. $\Delta 1$ defined the spin-flip gap between VB and CB from the different spin channels, while $\Delta 1+\Delta 2$ and $\Delta 3+\Delta 1$ reflect the energy gap in which the spin-conserved channels are polarized. For practical applications, an ideal BMS has a small $\Delta 1$, which enables a low energy shift for changing from the Fermi-level to a spin-polarized current, and large values of $\Delta 2$ and $\Delta 3$ to ensure effective transport of fully

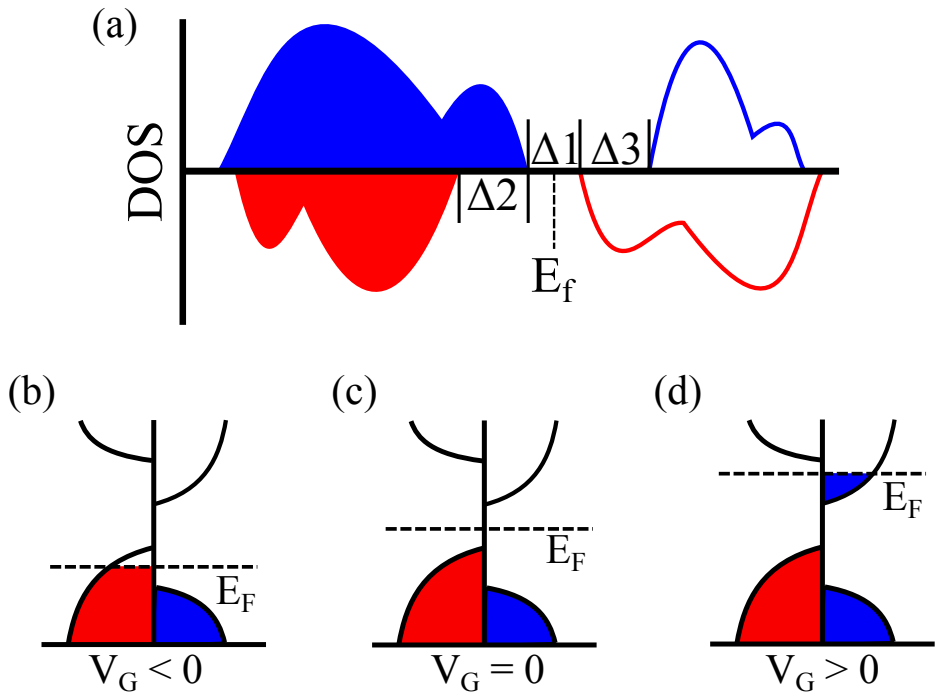

Fig. 3.2 (a) Schematic density of states of a bipolar magnetic semiconductor (BMS), where the $\Delta 1$, $\Delta 2$ and $\Delta 3$ are the energy parameters that are used to describe a BMS. The blue and red colors are used for different spin-polarized density of states. Schematics of the manipulation of external voltage gate (V_G) to control the current of electrons with specific spin polarization. When (b) $V_G < 0$, the Fermi level (E_F) decreases and a current of electrons from the red density of states flows. (c) $V_G = 0$, the output current is nearly zero as a result of the existence of a finite spin-flip gap. When $V_G > 0$, the Fermi level (E_F) decreases and a current of electrons from the blue density of states flows.

polarized electrons when the Fermi level crosses the VB or CB.

Manipulating the spin polarization of currents through BMS by switching the sign of a gate voltage instead of using an external magnetic field expose a new strategy to develop electrically manipulated spintronic devices. It can be used for the design of bipolar field effect spin filters, which can be set up by constructing a sandwich device made of a BMS between two normal metallic leads and it works in the same principle as explained above, where the sign of the V_G defines the spin orientation of the electronic current. Other potential application is to use BMS as a field effect spin valve, which is constructed with a similar setup as the bipolar field effect spin filter is used, but using two BMS instead of one. Different V_G are use for each BMS, where if both have the same sign, then the input current will be led through, otherwise the two BMS will mismatch and the magnetic the input current is prohibited. Another potential application of BMS is to use them to detect and separate entangled electrons from superconductors. This can be done by setting up two BMS as electrodes connecting a superconductor, in which

the V_G of each electrode has opposite signs, which lead to filter the spin by the polarization for each electrode.[116, 117]

In recent years, different types of materials have been explored for potential application as BMS, and can be classified as inorganic metal compounds, metal-free systems and metal-organic frameworks. From the first group, the intrinsic magnetic properties of metallic atoms are taken into advantage for the development of BMS. Some of the materials that have been studied in this direction are the transition metal disulfides,[119] monolayers made up transition metal halurides [120], $CrSiTe_3$ nanoribbons[121] and $CoCl_2$ nanowires.[122] In the second group of BMS materials include B_4CN_3,[123] polyporphyrin nanoribbons[124] and nanotubes based on C_4N_3.[125] In the last group, metal organic frameworks (MOF's) are a type of materials that combine an organic and inorganic part that can made up materials with interesting properties,[126] such as BMS. For instance, MOFś based on tetracyano systems with nickel atoms[127] and metalocarbonates[128] have been identified to have BMS features.

3.2 Computational approach

First principles calculations were performed within the spin-polarized DFT framework, including dipole correction, as implemented in the Quantum ESPRESSO package,[129] to investigate The electronic properties of functionalized phosphorene. The generalized gradient approximation (GGA) within the Perdew-Burke-Ernserhof (PBE) description was employed for the exchange-correlation functional[130], as well as the ultrasoft plane-wave pseudopotentials.[131] After testing for convergence, 680 eV was chosen as the cut-off kinetic energy of the wavefunction and 8 times that value was selected for the kinetic energy for the charge density. A 4 $\times$ 4 super cell of elementary phosphorene unit cells was set up for the simulation, while considering a vacuum space of 20 Å for the hydroxyl functionalized systems and 25 Å for the cysteine functionalized systems in order to avoid interlayer interactions. The Monkhorst-Pack [132] k-mesh 4 $\times$ 4 $\times$ 1 centered at Γ point was employed to sample the Brillouin-zone for the geometry optimization and single point calculations, while a denser mesh of 12 $\times$ 12 $\times$ 1 was used for the density of states and electronic band structure calculations. The energy between iteration, as convergence criterion, was set to 10^6 a.u., and the atomic coordinates were fully relaxed with the Broyden-Fletcher-Goldbarf-Shanno (BFGS) quasi-newton algorithm, until the maximum force on each atom was less than 10^3 a.u.

Our molecular model was built in consideration that oxygen atoms as chemical linkers have proven to be a successful strategy for the covalent functionaliza-

tion of 2D materials. [133] Therefore, the starting approach is to use OH radicals to report the effect on the electronic structure after the covalent bond formation between the P and O atoms. This was planned to distinguish the interface effect by pure covalent functionalization, lattice selection and coverage from effects related to using larger molecules, *e.g.*, long range interaction between functional groups of the molecules and the surface. Then the research moves further by the functionalization with cysteine molecules to explore if chiral discrimination can be reflected in specific features of the spin-polarized electronic structures, as it has been seen in other theoretical and experimental works.[134, 135] The functionalization with OH and L- and D-cysteine molecules were placed in the same P atom with respect to the unit cell, and the molecules are distributed to keep maximum distance between themselves and to maintain high symmetry.

3.3 Interface effects in phosphorene by OH functionalization

3.3.1 Single molecule functionalization

The first step was to investigate the atomic structure and stability of phosphorene functionalized with a single OH molecule in a 4 × 4 supercell, corresponding to a coverage of 6.25%, denoted as 1-OH system. Further, the systems will be compared with 12.5%, 18.75% and 25% coverage and are denoted similarly as 2-OH, 3-OH and 4-OH systems. The optimized lattice parameters in phosphorene are 3.30 Å along the zigzag direction and 4.61Å along the armchair direction, as it can be seen in Figure 3.1(a). Phosphorus atoms in pristine phosphorene has two different bond length distance, 2.22 Å in the in-plane bond and 2.26 Å in the out-of-plane bond (Figure 3.1(b)). [136, 137].

Different OH adsorption positions were tested around a phosphorus atom (denoted as P_O in Figure 3.3 (a)), but it was found that the optimal position of the oxygen atom was found to be on top of P_O. Structural changes are appreciated in phosphorene after the OH functionalization, where several P atoms around the functionalization site slightly change, but the largest modification can be see in the rupture of a bond between the P_O and the phosphorus atom from the bottom layer (denoted as P_B), where this distance changes from 2.26 Å to 2.63Å.

Analyzing the charge transfer in the system, most if it is centered between the OH molecule and the linked P_O, from which can be deduced that the phosphorene charge is drained by the OH group (Figure 3.4). Oxygen is electrophile and pulls an electron from the non-bonding electronic pair of P_O, forming a bond with a

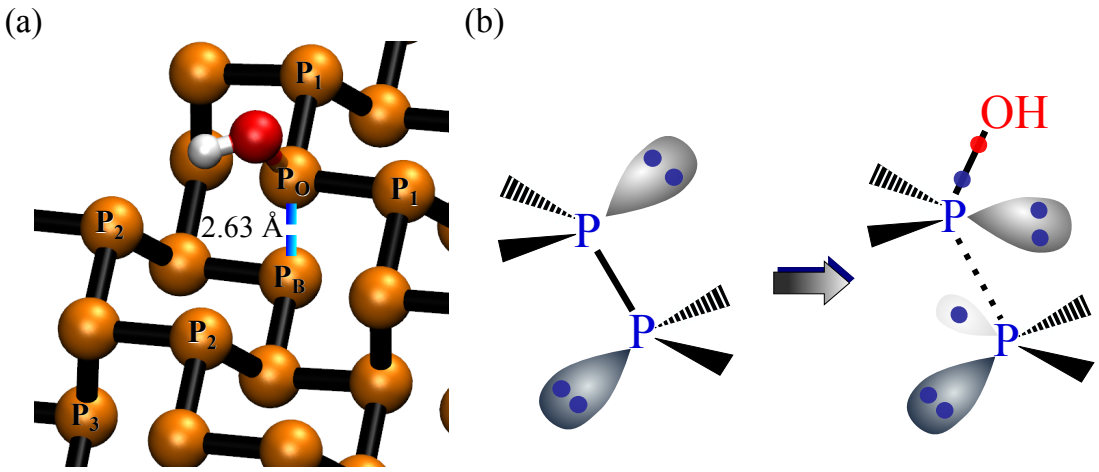

Fig. 3.3 (a) Illustration of phosphorene after OH functionalization, where the phosphorus atoms are showed in orange, the oxygen in red and the hydrogen in white. The most relevant atoms of the phosphorene are labelled. The blue dashed line indicates both phosphorus atoms with broken bond after functionalization. (b) Schematic representation of the bonds and the non-bonding electronic pairs of two out-of-plane phosphorus atoms in phosphorene and schematic after functionalization with a OH molecule, where the bond between the P atoms is broken and remains a dangling bond from the bottom layer phosphorus (P_B).

length of 1.69Å. The remaining electron from P_O gets paired with the electron that was part of the P_O-P_B bond, giving rise to the rupture of that bond and leaving a dangling electron in the P_B, as depicted in Figure 3.3 (b). This local electronic rearrangement changes the local geometry of the phosphorus atoms in the functionalization site, where P_O moves slightly up while on the contrary P_B moves slightly down. This changes the distance between the neighboring atoms, *e.g.*, the distance between P_B and its nearest neighbors decrease from 2.22 Å to 2.18Å. At difference to the local atoms to the functionalization site, atoms located farther away do not display any significant change in their bonding geometry.

Computing the adsorption energy of the system is a method to verify the stability of the system. The energy per functionalizing group (E_B) can be calculated as: [107]

$$E_B = \frac{1}{N_F}\left[E_{Phos+mol} - E_{Phos} - E_{mol}\right], \tag{3.1}$$

where N_F is the number of molecules in the supercell, $E_{Phos+mol}$, E_{Phos} and E_{mol} correspond to the total energy of the functionalized system, the pristine phosphorene and the isolated molecules, respectively. Negative E_B means that the functionalization reaction is thermodynamically stable, whereas positive E_B indicates that it is thermodynamically unstable. The 1-OH system has a E_B of

-2.22 eV, which means that the functionalization is energetically favorable. This result has also been reported in other theoretical studies where the structural and electronic characterization of phosphorene were tested with the functionalization of different biologically relevant molecules. [138]

One of the most interesting outcomes was to find out that the phosphorene, a material without intrinsic magnetism, acquires a total magnetization of 1 μ_B/cell after functionalization. The origin of the magnetization can be understood by analyzing the net spin density of the system (Figure 3.4), where the spin density is localized around the functionalization site, mostly in the P_B atom and, in lower proportion, in the oxygen atom and few atoms phosphorus atoms around P_B. The local magnetization, in correlation with the spin density, centers mostly in the P_B due to the formation of the dangling bond, which is in agreement with other studies in which non-magnetic materials gain magnetism after the formation of dangling bonds or diradicals. [112, 139–141] Therefore, phosphorene functionalization represents an alternative approach to induce magnetism in a non-magnetic system without doping with metallic atoms, as it has been done in other study. [142]

The spin-resolved electronic band structure of the 1-OH system is presented in Figure 3.4(d). The in-gap electronic bands have weak dispersion due to the local structural changes in phosphorene as a functionalization. The weak dispersion results from the large separation ($>$ 1.2 nm) between functionalization sites in the supercell and its images when using periodic boundary conditions. Besides the in-gap bands, the bandgap in the 1-OH system is larger than in pristine phosphorene (Figure 3.4(c), increasing from 0.88 eV to 1.0 eV (computed with the PBE XC-functional). The emergence of the in-gap bands and the increase of the bandgap has also been seen in other studies of functionalized phosphorene. [107, 108, 138]

Moreover, there is a transition from a direct bandgap, present in the pristine form, to an indirect bandgap after functionalization can be seen, where the valence band maximum (VBM) is located at the X point while the conduction band maximum remains in the Γ point. The change from direct to indirect band after functionalization can be related to change in the symmetry in the system. Looking to the highest bands in the valence band from pristine phosphorene (0.05 eV and 0.5 eV at Γ point), the bands change in the path $\Gamma \longrightarrow X$ from being not degenerated to degenerated, and that follows for the rest of the K-path. But in the 1-OH system, these two bands are not degenerate in the X point, rather from the S point. The symmetry changed along the X direction as a result of the broken P_B-P_O bond, causing the change of energy between both bands.

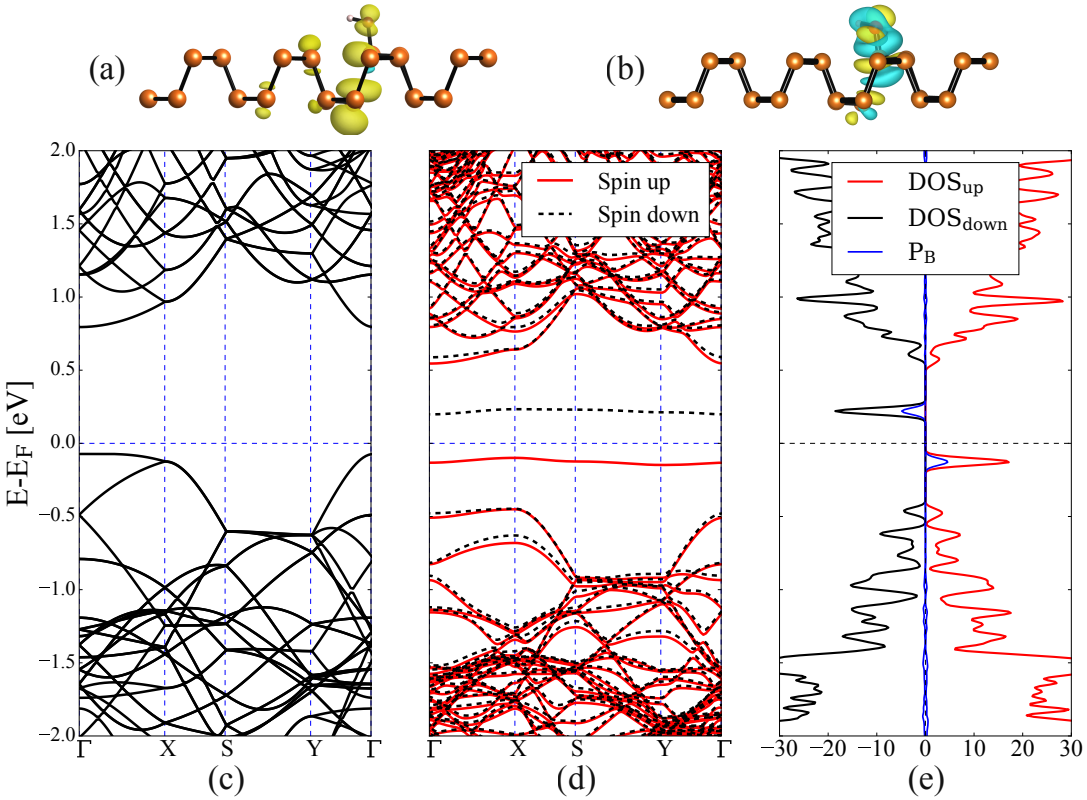

Fig. 3.4 (a) Side perspective of spin density difference ($\Delta\rho_s = \rho_s^{\uparrow} - rho_s^{\downarrow}$ of the 1-OH system after functionalization. The yellow and blue isosurfaces correspond to the positive and negative spin difference, respectively. Most of the positive spin difference lies around the P_B. The isosurface value of this projection is 0.002 e/bohr^3. (b) Side perspective of charge density difference after OH functionalization. (c) Electronic band structure of pristine phosphorene. (d) Spin-resolved electronic band structure of 1-OH system for spin-up (red lines) and spin down (black dashed lines). Two in-gap bands appear after the functionalization, compared with the pristine system. (e) Total density of states of 1-OH system (red and black lines) and resolved density of states of P_B (blue line).

The in-gap spin-up (red lines) and spin-down (black lines) bands have a very strong exchange splitting of about 0.33 eV at the Γ point. Several of the bulk bands also have a weak spin splitting of about 0.3-0.5 eV, being the valence bands closer to the bandgap the ones who have more noticeable splitting. This small splitting of the bulk bands can be seen by a small vertical shift of the spin-up and spin-down components of the spin-resolved density of states (DOS)3.4(e). The spin-resolved DOS clearly reflects a ferromagnetic (FM) state. The projected DOS of the P_B atom is also shown in Figure 3.4, where it can be seen that is the atom yielding the largest contribution to the in-gap states. All the other atoms around the functionalization site have minor contribution to the spin-resolved DOS around the in-gap states, and from that, they have predominant p_z and p_y orbital contribution (see Appendix A.1) In terms of the contributions per atom

to the total magnetic moment, the largest magnetic moments are located on P_B (0.076 μ_B/cell), P_O (0.046 μ_B/cell), Oxygen (0.03 μ_B/cell) and P_2 (0.013 μ_B/cell).

Summing up the discussed information of this subsection, the functionalization of phosphorene with a single OH group leads to the local magnetization of phosphorene. But, does the bond breaking effect and consequent introduction of magnetization will arise for a few-layer phosphorene system? To answer this question, the same calculation was carried out as in the 1-OH system but employing a bilayer phosphorene. It was found that the P_O-P_B bond breaks, a dangling bond is formed and the spin polarized in-gap states appear. From an experimental point of view, employing few-layers system can be an advantage to decrease the exposure of the dangling bond to other components from the opposite side from the functionalization, which could lead to a chemical reaction and eventual loss of the generated local magnetization.

3.3.2 Lattice selection

Phosphorene, as mentioned in the introduction of this chapter, has anisotropic properties, which means that the properties of the materials will depend from which lattice direction it is measured. Hence, it is from our interest to research if phosphorene functionalized along their different lattice directions produce different results concerning their electronic structure and the induced magnetism, as discussed above for the 1-OH system. To do so, 2 OH groups placed in three different arrangements in the supercell were considered (see Figure 3.5), corresponding to diagonal, armachair and zigzag directions, respectively. In this setup, the 2 OH groups are not located in contiguous unit cells, *i.e.*, skipping one phosphorene unit cell, done in this way to avoid additional effects by the interaction between neighboring OH molecules and to keep the internal symmetry in the supercell and with the neighboring supercells.

Additionally, since two broken bonds are expected to happen in theses systems, and with that, two localized magnetic moments, it is necessary to consider the ferromagnetic (FM) or anti-ferromagnetic (AFM) ordering in the supercell. To get that done, the simulation of the system was computed setting the initial magnetization of the P_B atoms with the same or different sign, respectively. The outcome shows that the FM and AFM states of the diagonal configuration are nearly degenerated, with an energy difference of only 0.9 meV in favor of the FM state. And yet, armchair and zigzag configurations have a preferred FM ground state, with a difference of 3.7 meV and 2.5 meV lower than the AFM state, respectively. This energy difference means that, at room temperature,

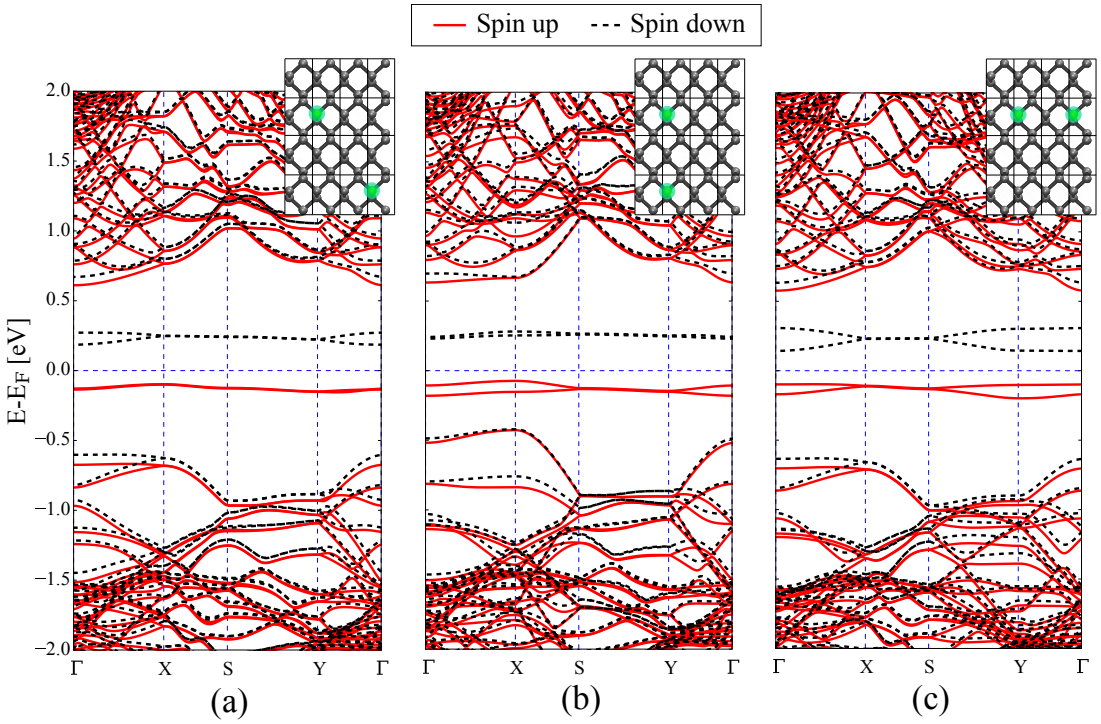

Fig. 3.5 Spin-resolved electronic band structure of (a) diagonal, (b) armchair and (c) zigzag lattice functionalization. The spin-up and spin-down bands are represented by red lines and black dashed lines, respectively. In the upper right corner of each panel there is a sketch of the supercell and, highlighted by green dots, the corresponding phosphorus atoms that serve as functionalization sites.

thermal fluctuations may lead to an overall nonmagnetic ground state, which is preventable if the system is kept at low temperatures, in which the FM state will become stabilized.

Concerning the energy stability of the three lattice functionalization systems in their FM ground state, the zigzag configuration was found to have the lowest energy, while the diagonal configuration lies 4.6 meV above it, and at the end the armchair configuration by 15.95 meV. Regardless the energy difference between the three systems, after calculating their adsorption energy per functionalizing group with the Eq. 3.1, it was found that all of them are thermodynamically stable, with an E_b of -2.22 eV.

Regarding the geometry of the systems, the distance between the functionalization sites is 11.35 Å, 9.23 Å and 6.6 Å in the diagonal, zigzag and armchair systems, respectively. As expected, each OH functionalization cases a break of a P_O-P_B bond and slight structural modifications around the functionalization site, in similar way as discussed in the 1-OH system. The bond distance between the oxygen atom and its respective P_O is 1.69 Å for all the cases. The only structural difference between the three systems is the distance between P_B and P_O, which is 2.62 Å in the diagonal system and 2.603 Å for the armchair and

zigzag systems.

The spin-resolved band structures of these systems are shown in Figure 3.5, where two spin-up and spin-down in-gap bands are present in each system as the consequence of the formation of two dangling bonds. Associated with the dangling bonds induced magnetism, the total magnetic moment in the system is 2 μ_B/cell (for the FM ground state, the AFM states have 0 μ_B/cell). The linear additive behavior of the magnetic moment suggests that the distance between the dangling bonds in all three cases is large enough to prevent any sizeable Heisenberg-type exchange coupling. To figure out if this effect can be seen in phosphorene, different arrangements with shorter distance between functionalization sites was tested, from which it was found that, when the distance order is 2.2 Å, the total magnetic moment of the supercell was found to be 1.5 μ_B.

The spin-up and spin-down in-gap bands from the three systems have different degrees of degeneration along the K-path. The diagonal arrangement (Figure 3.5 (a) has the largest distance between the functionalization sites, therefore, the pair of spin-up in-gap bands are almost degenerated, and comparably the spin-down in-gap bands with the exception of a small splitting in the Γ point. However, the degeneration is almost lifted for the armchair and zigzag systems, as seen in Figure 3.5 (b) and (c), aside from the high symmetry directions of each system, that correspond to $S \longrightarrow Y$ for the armchair system and $S \longrightarrow X$ for the zigzag system.

Regarding the spin-resolved valence and conduction bands, the diagonal and zigzag configurations have larger similarity than the band structure of the armchair system. Both systems have direct bandgap from the Γ point, have similar degree of exchange splitting in the VBM and CBM and their bandgap is $\sim$ 1.2 eV, which is larger than the zigzag configuration, 1-OH system and pristine phosphorene. On the other hand the zigzag configuration has an indirect bandgap from X in the VBM to Γ in the CBM, the VBM exchange splitting is not as large as in the previous two systems and the bandgap is $\sim$ 1.04 eV.

After this brief discussion, it is determined that the electronic structure properties and magnetization of phosphorene can be controlled by the lattice selection along the functionalization takes place.

3.3.3 Coverage

The coverage, or degree of functionalization, it is other parameter of interest when functionalizing surfaces, because one can determine at which extension the properties of a material can be modified in the desired direction without having counterproductive or negative effects. The influence of the coverage was

proceeded by comparing the previously defined four cases 1-OH, 2-OH, 3-OH and 4-OH systems, as it is shown in Figure 3.6, where the highlighted green dots represent the P_O. The 3-OH and 4-OH systems were built up by conserving maximum distance between functionalization sites and to keep the symmetry inside the supercell and with the neighbouring supercells. Consequently, the 2-OH system used in this comparison corresponds to the diagonal configuration that was discussed in the section above, since it has the largest distance between the functionalization sites.

In terms of thermodynamic stability, the adsorption energies remain similar to the previous results obtaining a value of -2.22 eV and -2.21 eV for the 3-OH and 4-OH systems, meaning that the adsorption is still favorable. In regard to the geometry of the systems, the P_O-P_B distance decreases linearly in proportion to the number of adsorbed molecules with average values of 2.63 Å, 2.62 Å, 2.60 Å and 2.58 Å. On the other hand, the average bond distance between the P_B and the first neighbors as well as between P_O and oxygen remain with minor changes. This states that the coverage is relevant for the local structure of the functionalization sites and determines their interaction strength.

Similarly as the case of 2-OH systems discussed above, the total magnetic moment in the supercell is additive and increases as an integer in proportion to the coverage. This, as discussed above, by the formation of a dangling bond per functionalized molecule. Evidently, a deviation of this linear magnetic increase is expected beyond a certain threshold, in which the local magnetic moments start to interact, either because of functionalization site proximity or saturation. Following the same procedure as in the 2-OH systems, the magnetic ground state was evaluated to find if there is a preferred state that differs when the degree of coverage increases. It is important to mention that, in contrast to the 2-OH and 4-OH systems, there is no possibility to set up an AFM state in the 3-OH system, since it is required an even number of functionalization sites in order to set equivalent distribution of parallel and antiparallel magnetic moment in the P_B atoms. Regardless of this limitation, an additional magnetic state with two local parallell and one antiparallel moment was explored and compared with the full parallel configuration. Comparing this two states, it was found that the 3-OH system has a FM ground state, where the former described state leis 7.6 meV above it. Concerning the 4-OH system, the AFM state is preferable, while the FM state is located 5.2 meV above it.

In Figure 3.6 the spin-resolved band structure of the four systems are displayed, where, for the sake of simplicity, only the FM states for all the systems are presented, even though the 4-OH system has an AFM ground state. It can

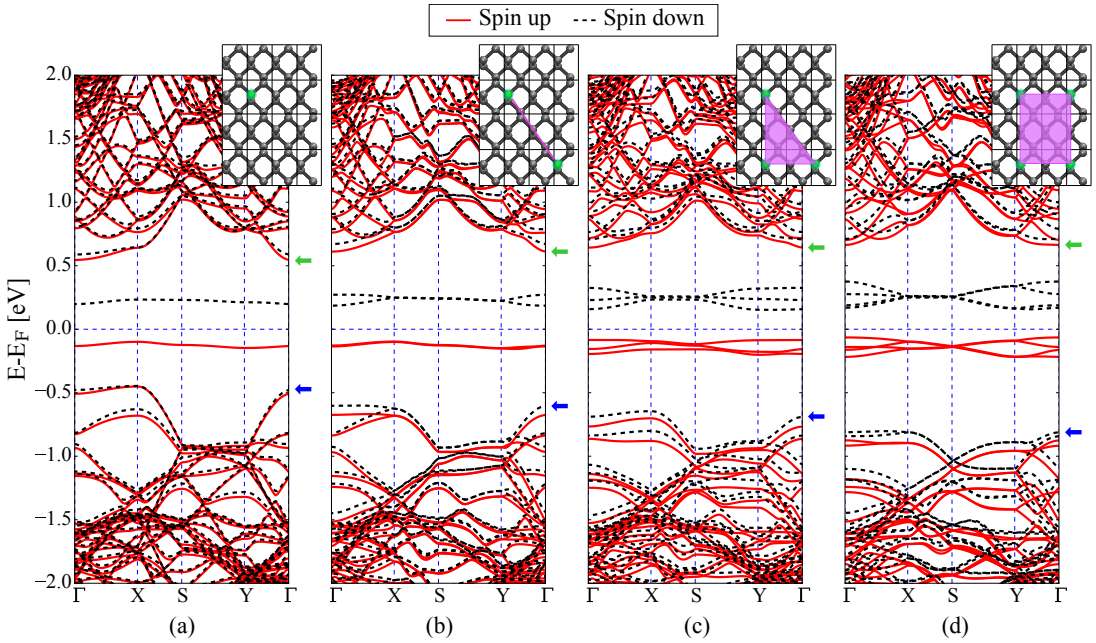

Fig. 3.6 Spin-resolved electronic band structure of (a) 1-OH system (6.25%), (b) 2-OH system (12.5%), (c) 3-OH system (18.75%) and (d) 4-OH system (25%). The spin-up and spin-down bands are represented by red lines and black dashed lines, respectively. In the upper right corner of each panel there is a sketch of the supercell and, highlighted by green dots, the corresponding phosphorus atoms that serve as functionalization sites. The pink line/figure is placed over the supercell only in means of ease the understanding of the location of the functionalization sites. The blue and green arrows indicate the energy position of the VBM and CBM at the Γ point.

be spotted that an increased number of in-gap bands is correlated to the increase coverage of the system. Each functionalized molecule breaks a P_B-P_B bond causing the formation of a dangling bond around the respective P_B and then generating a pair of in-gap bands, which, at this degree of coverage, is conserved. The dispersion of the in-gap bands is increased in relation to the coverage, which is a consequence of the reduction of functionalized lattice sites and the local structural changes around each P_B. Moreover, similar effect can also be seen in the valence and conduction bands when the functionalization degree is high, like the 4-OH system, where a complete separation between the spin-up and spin-down bands in the top of the valence band.

Other property than changes in function of the functionalization coverage is the bandgap. In Figure 3.6 blue and green arrows indicate the positions of the VBM and CBM for each system, where a trend can be seen along the systems, in which the VBM decreases in energy and the CBM increases. The contrast of this trend can be seen by comparing the bandgaps of the extreme cases, where the 1-OH system's bandgap is $\sim$ 1 eV and the the 4-OH system's bandgap is $\sim$

1.5 eV. Other pattern found in the electronic structure is the shift between direct and indirect bandgap. The former one is seen in the 2-OH and 4-OH systems, while the later one is seen for the 1-OH and 3-OH systems. This can be caused by a symmetry effect after OH functionalization or an even-odd effect. From the discussion of this section it is confirmed that the electronic band structure and magnetic properties can be tuned by the functionalization degree in the phosphorene supercell.

3.4 Chiral functionalization effect in phosphorene

In the previous section the changes in electronic structure were correlated to the O-P bonding and, thus, can be considered as an interfacial effect. If this statement is true, at least for small molecules, no further modifications would be expected as far as they are able to bind covalently to phosphorene via oxygen-like linker. After investigating how OH groups can tune the electronic band structure and magnetization of functionalized phosphorene through different variables, in this section the discussion turns into the study of the binding of a more complex molecule that is relevant due to their magnetic properties, cysteine.

Cysteine is a sulfur-containing aminoacid (see Figure 3.7 (a) and (b)) that, as most of the aminoacids, due to their four different groups bonding one of its C atoms, is a chiral molecule. Chiral molecules are pairs of enantiomers that are designated with the prefix right- or D- and left- or L- and the images of such pairs can be seen as the mirror image from the other. These type of isomer, regardless of having the same chemical composition and almost same structure, share pretty different chemical properties. Previous studies with cysteine in spintronic devices have shown an effect called chiral-induced spin selectivity (CISS), where, depending on the chirality of the molecule, the electrons transmitted through the device have a preferred spin oriented, regardless of the initial spin orientation.[134, 135] This subsection aims to disclose whether CISS effect is present in this type of systems by the employment of chiral cysteine molecules, which could play a role with the induced magnetization of phosphorene.

The functionalization setup is similar as the 2-OH system with diagonal arrangement, which later it is also used for comparison. If the interface effect is dominant, then there should not be a major change when considering a double L-cysteine pair (LL-Cys) or an D- and L-cysteine pair (DL-Cys) on phosphorene. As a control test, double D-Cysteine pair (DD-Cys) was included in the simulations.

The adsorption energy of the cysteine molecules on phosphorene was calculated through the Eq. (3.1) and resulted in an E_B = -2.04 eV for the three

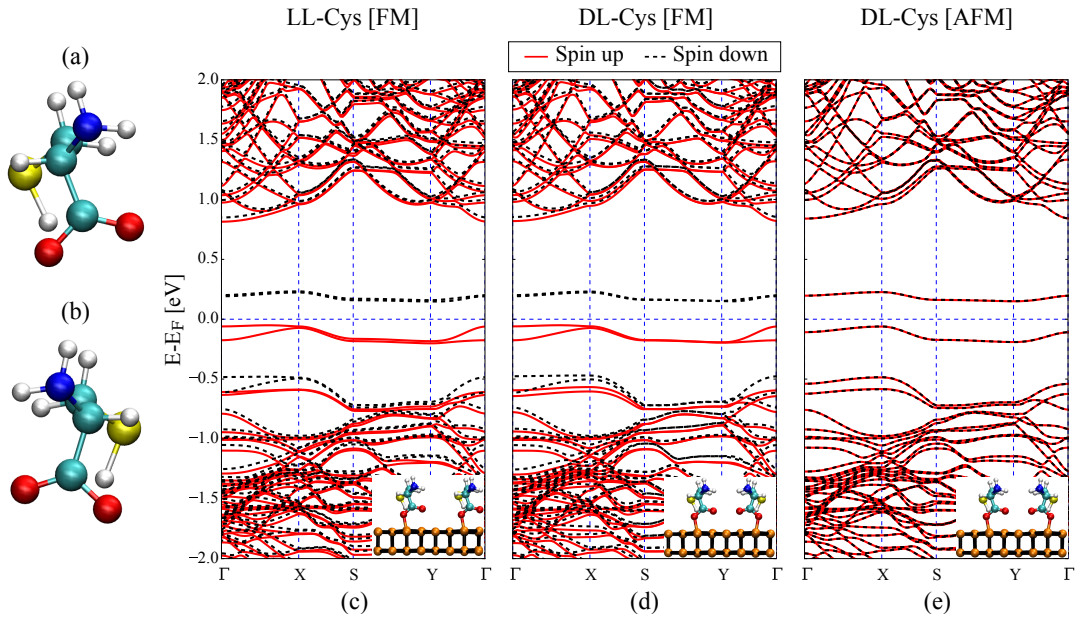

Fig. 3.7 Molecular representation of deprotonated (a) L-cysteine and (b) D-cysteine. From where C atoms are represented with light blue, O atoms with red, S atoms with yellow, N atoms with dark blue and H atoms with white. Spin-resolved electronic band structure of (c) FM state LL-Cys, (d) FM state DL-CYs and (e) AFM state DL-Cys. The spin-up and spin-down bands are represented by red lines and black dashed lines, respectively. In the upper right corner of each panel there is a sketch of the supercell and, highlighted by green dots, the corresponding phosphorus atoms that serve as functionalization sites. At the bottom-left corner of each panel there is an inset of the front perspective of the functionalized systems

systems, showing independence of the molecular chirality. Compared with the OH groups on phosphorene, the obtained E_B for cysteine is higher, but regardless of that, the negative sign means that the adsorption is thermodynamically stable. Structural modifications post-functionalization previously discussed in the OH-systems, such as P_O-P_B bond breaking, are also present in the cys-systems. Nevertheless, some differences have been spotted. For instance, the P_O-P_B distance decreased from 2.62 Å in the 2-OH system to 2.53 Å. Also the bond distance between the oxygen atoms and their respective P_O increased from 1.69 Å to 1.83 Å. The variation of the structural modification can be a consequence of the different partial charges of the oxygen linking atom between the OH group and the -COO group.

Moving on the magnetic properties, dangling bonds are present in the cysteine-based systems after the rupture of the P_O-P_B bonds, therefore the magnetic ground state of these systems had to be determined. LL-Cys and DD-Cys have a FM ground state, whereas the AFM state lies $\sim$ 25 meV above the FM configuration. This energy difference between both states means that the FM state

may survive thermal fluctuations up to nearly room temperature. Nonetheless, the FM and AFM states in the DL-Cys are almost degenerated, with only 1.2 meV difference. This means that its magnetic behavior can disappear at any temperature. Some additional tests were carried out to clarify if one of the two magnetic states could get stabilized. The tests consisted in repeat the calculations but bringing the molecules closer to each other and compute the energy for each magnetic state. The results show that at a separation of 9.3 Å between the molecules, the AFM become more stable with an energy difference of 2.85 meV, from which it can be inferred that at low temperatures, under 35 K, the AFM ground state may get stabilized.

The electronic structure cysteine-based systems are shown in Figure 3.7 (c-e), where, as a matter of simplicity, the results of the DD-Cys were omitted because the band structure is the same as the LL-Cys. The spin-up and spin-down in-gap bands are present as a consequence of the dangling bonds formed after functionalization. These systems have a direct bandgap of $\sim$ 1.3 eV, which is a larger value than for the 2-OH system, meaning that this value can be modulated by the functionalized molecule. A test model in which the phosphorene structure of the optimized geometry after cysteine functionalization was later used with OH groups in the cysteine positions for a single point calculation without optimization. This with the aim to keep the structural changes of the phosphorene caused by the cysteine molecules, but removing the long distance interaction and replicate similar chemical environment as the studied OH-systems. This resulted in a electronic band structure that was very similar to the cysteine-based systems, but with a decrease in energy of the conduction bands of $\sim$ 0.15 meV. Therefore, the change in the bandgap can be attributed to the difference of the structural modification around the functionalization site, the long range interaction of the molecule with the surface and the dipole moment of the molecules.

Furthermore, the valence bands, specially the VBM, show lower degeneracy than the conduction bands. Compared with the 2-OH system, the degeneracy is lower and almost similar to the dispersion reached in the 4-OH system. Regardless the larger dispersion that cysteine molecules can cause in the band structure of phosphorene compared with the changes produced by the larger degree of functionalization coverage by OH molecules, it is worth to mention that cysteine molecules occupy larger spatial volume and have more functional groups than the OH group. This could lead to some steric effects that may limit the degree of functionalization in phosphorene, meaning that can reach less coverage than smaller molecules and, therefore, reach first the limit for tuning phosphorene properties.

On the other hand, the DL-Cys AFM state (Figure 3.7 (e)) have complete degeneration of spin-up and spin-down bands, which, evidently, leads to its AFM state. The bandgap of the system is also ∼1.3 eV, but at difference to its FM state, the bandgap is indirect from X point to Γ point, similar to the previously systems with indirect bandgap. Even though a CISS effect was not found when computing the properties of LL-Cys and DD-Cys, a chiral-dependant magnetic ground state of the functionalized system was found when computing the mixture of both enantiomers in the phosphorene supercell.

3.5 Functionalizing phosphorene towards BMS

In the previous sections the changes in the electronic band structure by molecule selection, lattice direction, coverage and chiral functionalization effects were disclosed. Now the discussion focus on the potential application of this type of materials as the beforehand introduced bipolar magnetic semiconductors (BMS). As presented at the beginning of this chapter, there are three energy parameters, Δ1-3, that can be used to characterize BMS. The possible application of the phosphorene functionalized systems is gonna be evaluated and discussed in function to these energy parameters. The possibility of evaluating Δ1-3 in these systems relay in the formation of the in-gap spin polarized electronic states, therefore, only the FM states of the functionalized systems are considered, ignoring that for some few cases the AFM state was preferable (see Figure 3.8(a)).

The first addressed point to evaluate is the coverage of the system, as shown in Figure 3.8 (b), where a dependence of the Δ1-3 can be seen. There is a decrease of Δ1 and an increase of Δ2 and Δ3 when the number of OH molecules in the supercell increases. The former result can be explained by the accumulation of in-gap states around the Fermi-level due to the increase of dangling bonds. The later result is a consequence of the energy increase of the VBM and energy decrease of the CBM in function of the coverage. These are positive results towards the development of BMS devices, because a low Δ1 ease the gate voltage energy required to transit between spin-up and spin-down current, and the large Δ2 and Δ3 guarantees the exclusive transmission of polarized electrons, *i.e.*, enhances the stability of the half-metallicity in BMS devices.

Then, moving to the molecule selectivity BMS-dependence, the magnitude of the Δ1-3 parameters were compared between the two types of functionalizing molecules. The most comparable configurations correspond to the 2-OH system in diagonal arrangement and the LL-Cys system, since they have the same coverage. The value of Δ2 in LL-Cys is smaller than in the 2-OH system, as a consequence of the higher energy of its VBM, which is a result of the inclusion

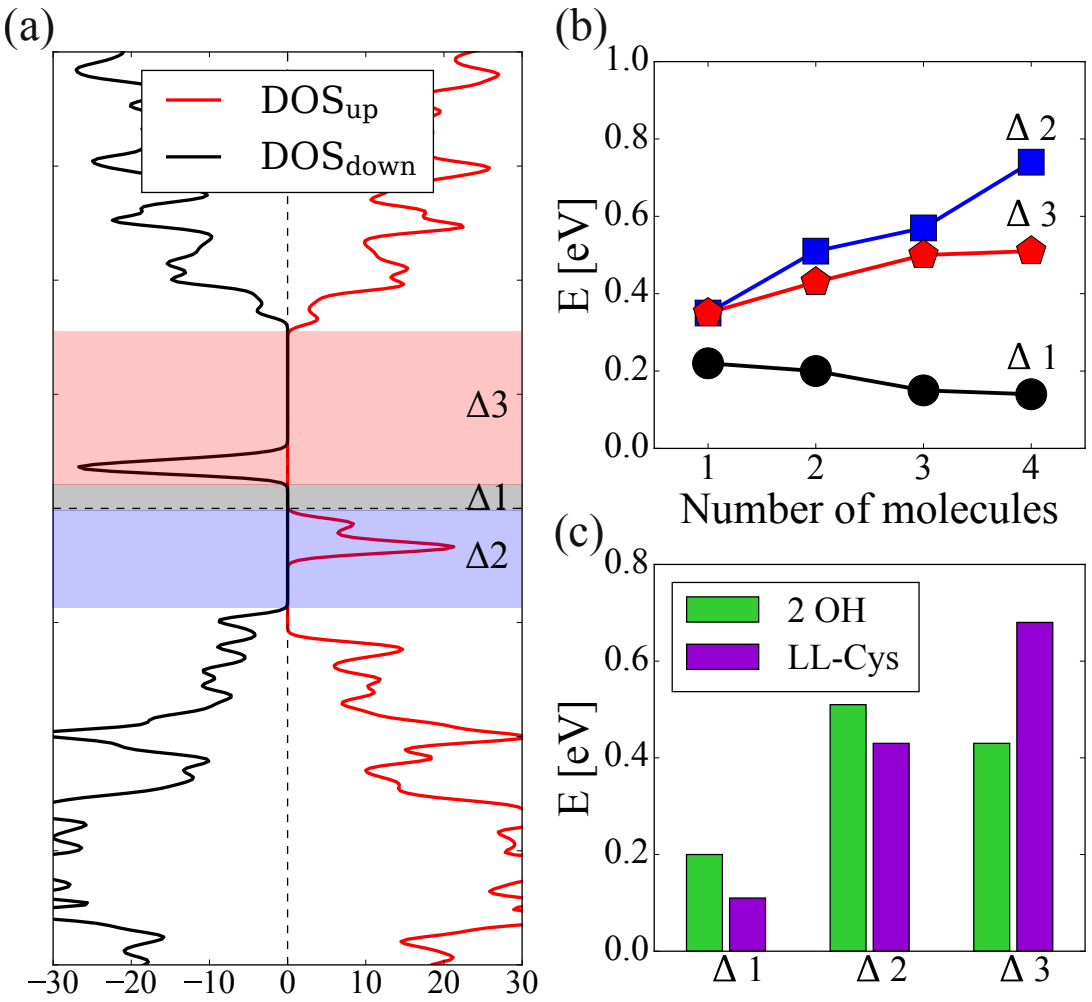

Fig. 3.8 (a) Spin-resolved DOS of FM state LL-Cys. Spin-up and spin-down states are projected with red and black lines respectively. The black, red and blue highlighted regions represent the energy parameters that characterize bipolar magnetic semiconductors (BMS): $\Delta 1$, $\Delta 2$ and $\Delta 3$ respectively. (b) Characteristic BMS energy parameters of OH functionalized phosphorene in function of the number of OH molecules per simulation cell. $\Delta 1$, $\Delta 2$ and $\Delta 3$ are represented with black, blue and red lines. (c) Comparison of the BMS energy parameters between OH system and LL-Cysteine in green and purple bars, respectively.

of larger number of bands in the valence band from the cysteine molecules. On the other hand, $\Delta 1$ of LL-Cys is almost half of the value calculated for the 2-OH system, which is followed by the larger broadening of the spin-up in-gap states in LL-Cys. For last, the largest difference between both systems correspond to the $\Delta 3$ parameter, in which LL-Cys surpasses the 2-OH system by $\sim 50\%$. This difference is directly correlated to the energy of the CBM, which is higher in the LL-Cys, 0.77 eV against 0.61 eV in the 2-OH system.

In literature, the possibility of using phosphorene as a BMS was previously reported. In this study, phosphorene was doped with different type of metals, corresponding to the group 3D in the periodic table, which induced different type

of magnetic properties in phosphorene, leading to a range of magnetic profiles and potential applications as different classes of spintronic materials, such as BMS. Nevertheless, the presented results discussed in this chapter show insights into developing BMS materials independently of doping phosphorene with transition metals, by approaching the modification of phosphorene through a systematic functionalization in terms of coverage and lattice selection, where it can reach similar values of Δ1-3 as in the former study, and, with the further research towards the selection of functionalization molecules, these values may be further improved.

3.6 Summary

In this chapter, the electronic and magnetic properties of phosphorene after OH and cysteine functionalization by means of spin-polarized DFT calculation was investigated. The values of E_B for all the functionalized system showed that they are thermodynamically stable. One of the main contributors to the discussed properties in this chapter was the formation of a dangling bond in the P_B atom as a consequence of the P_O-P_B bond rupture followed by the molecular adsorption. This was the origin of the spin-up and spin-down in-gap bands, hence, phosphorene, a non-magnetic organic system, acquired magnetic properties.

The magnetic ground state for each studied system was determined, finding that most of the systems have an FM ground state, with the exception of the 4-OH system and DL-Cys, which both are degenerated. In regard to the lattice functionalization, the zigzag configuration has lower energy than the diagonal and armchair configurations. Several parameters of the electronic band structure, such as bandgap energy and direction and in-gap degeneration, can be modulated with the molecular arrangement and coverage of the functionalized molecules. The total magnetization was found to be proportional to the number of functionalized molecules in phosphorene, even though this trend is expected to fall after crossing a threshold.

A correlation between the chiral functionalization and CISS effect was not found in this study, but, the employment of a enantiomers mixture could lead to a diversification of the magnetic ground state. Also the distance between the functionalized molecules could lead into a more stable magnetic ground state. Finally it was proved that phosphorene functionalized systems can engineered, either by lattice direction, coverage or molecule type selection, to design bipolar magnetic semiconductors, as the trends towards enhancing the Δ1-3 parameters were presented in this investigation, which can be a step-stone leading to the development of spin-based devices.

CHAPTER 4

Tuning transport properties through strain and grain boundaries

Diverse properties of low dimensional materials, such as electronic and thermal transport, can be modulated by strain engineering, ultimately with the goal of achieving high-performance low dimensional based devices. Other structural approach that influences the mechanical behaviours and properties of low dimensional materials are the introduction of various defects types. This has become a research field for the emergence and development of topological design and defect engineering devices.

In this chapter, the mechanical strain and a specific structural defect, the grain boundaries (GB), are addressed as variables for modifying the electronic, thermal and thermoelectric properties of phosphorene. In a DFTB framework, phosphorene GB are studied under applied strain to understand the potential effects that these two structural-mechanical variables can influence their electronic, thermal and thermoelectric properties. This chapter relies on Ref.[143]

4.1 Introduction

4.1.1 Strain in low dimensional materials

Strain engineering, among various methods to tune the quantum mechanical effects of low-dimensional materials, has emerged as a powerful tool for modifying lattice spacing and symmetry, hence changing electronic band structures, electron correlations and topological orders in lattices. Strain-induced manipulation of quantum properties is not a new approach, research in this field has been carried for over 50 years, starting with the reported spatial condensation of electrons in silicon and cuprous oxide systems in the 1970s,[144, 145] and later on, in the 2000s, this strain engineering was employed in the semiconductor, in which the uniaxial or biaxial tensile strain applied to silicon transistors cause the electron and hole mobility to be greatly enhanced.[146] However, unlike the bulk counterparts, strain engineering in low dimensional materials is highlighted by the

outstanding mechanical resilience and strain sensitivity, offering a wider range of application, since they can withstand greater elastic strain before finding fracture, enabling improved efficiency and versatility.[147] For instance, graphene can withstand 25% elastic strain, which is 250× the breaking limit for the most of graphite materials.[148]

The method selection to induce strain in the system is a relevant step in this field, since it can define the stability of the tensile force, the type of induced forces, the axial deformation, and the potential applications. For instance, lattice mismatch method consists in inducing strain in single crystals due to the mismatch of lattice constants between the desired crystal to growth and the employed substrate. This method permits the induction of tensile or compressive strain in the material and can be used to stack up lateral heterojunctions. But this method becomes more complex by having inhomogeneous strain along the different layers, because the strain is the largest at the center of the mismatched interface and decreases in the region fat away from the interface. This could lead to thickness-dependent properties, which require further study but it can also lead to different applications.[149] Other method to induce strain in the low-dimensional system is by the employment of flexible substrates such as polydimethylsiloxane and polystyrene. The advantage of this method is that the strain can be induced and adjusted by applying an external force to the substrate, at difference to the lattice mismatch that is fixed to the lattice of the substrate. The strain induced through this method can be caused by the production of wrinkles in the substrate, thermally expanding or contracting the polymer or using a direct applied strain on the upper surface that bends the material.[150]

Recent theoretical and experimental work has demonstrated that mechanical strain can play an important role in manipulating the electronic and thermal properties of low dimensional materials. The electronic properties of a material is linked to the changes of its electronic band structure and orbital character of the valence band maximum (VBM) and conduction band minimum (CBM), which can be induced by external strains. For instance, the bandgap in monolayer MoS_2 decreases when increasing the applied tensile strain, which suggest that a semiconductor-to metal phase transition can happen under large strains.[151] Additionally, theoretical studies have proved that strain not only influence the bandgap, but also change the carrier mobility. Other study with few-layer MoS_2 flake compared the carrier mobility of the flat device with the wrinkled device at low temperatures, resulting in the strained device being two times higher than the former one.[152]

In regard to the thermal properties, they can be also exploited by using strain

engineering. For instance, a theoretical study of 2D hexagonal BAs showed that applied strain can enhance thermal conductivity by a factor of two.[153] An experimental study based on multilayer graphene showed that the thermal conductivity is highly strain-dependent, finding a decrease of $\sim 70\%$ after applying only 0.1% strain.[154] Similar results have been seen in MoS_2 and hexagonal BN, where thermal conductance continuously decreased upon increasing the strain level.[155]

As a consequence of the changing of the electronic and thermal properties, modulation of thermoelectric properties have also been reached by strain engineering. That is the case of 2D InSe monolayer, which has shown that, upon tensile strain, its anharmonic phonon scattering increases and gives rise to enhancing phonon scattering rate, reduction of phonon group velocity and heat capacity, which leads to the decrease of lattice thermal conductivity and enhancement of the thermoelectric figure of merit ZT.[156] Other example can be seen with an organic semiconductor based on tetracyanoquinodimethane, which showed a strain-dependent bipolar behavior. When a negative strain is applied, there is a high increase of electron mobility and small increase of the power factor PF and ZT, but when the system is under a positive strain, there is la large decrease of thermal conductivity and high increase of ZT.[157]

4.1.2 Grain boundaries

It is well known that most of the bulk or 2D materials, either produced in-situ or extracted from nature, are not composed of single crystal units, but rather they are polycrystalline materials in a network of multiple interfaces. To make use of the intrinsic properties of low dimensional materials, it is important to control both interlayer interfaces and intralayer dislocations. Some methods and techniques have been developed to avoid the formation of crystalline disorders and produce single-crystalline materials with atomically clean interfaces. However, the understanding of the consequences of structural defects and interlayer interfaces offer a path to tune their properties by a controlled fabrication of the crystal boundaries. The interfaces between the crystal units are known as grain boundaries (GB), which can significantly affect the properties of the material when compared with the pristine counterparts.[158]

GB can be classified within two main types: the structural defects that rotate out-of-plane, named stacking GB, and dislocation that rotate in-plane, named stitching GB. The main difference between the stitching and stacking GB is that the former one involve strongly distorted covalent bonds at the interfaces. Under controlled kinetic and energetic conditions, the boundary structure can be main-

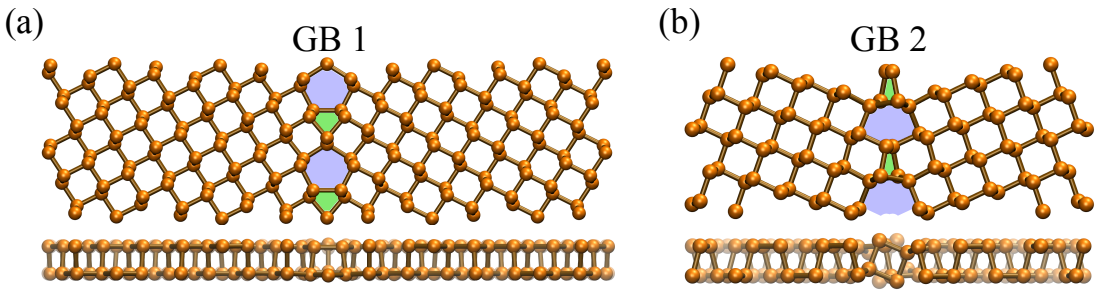

Fig. 4.1 Atomistic representation from top and side view of the two phosphorene grain boundaries studied in this chapter: (a) GB1 system (5|7 defect) and (b) GB1 system (4|8 defect). Both systems were designed with two zigzag and armchair phosphorene monolayers, respectively. The blue and green shades highlight the regions of the grain boundaries in the middle of the system.

tained, which also means that GB are not formed randomly, but only at specific rotation angles, depending on the material's lattice, GB are thermodynamically stable. As it follows for the rest of the chapter, only stitching GB are addressed.

The most common method to describe GB geometry is through the misorientation angle θ_M, which is defined as an angle through one lattice is rotated in reference to a common axis between two single crystals.[159] In a study about electrical properties of graphene GB, the θ_M was found to be a variable that can influence the average electrical conductivity, where a minimum value was reached at a GB θ_M of 30°.[160] Other method employed to describe the GB geometry is by stating the number of edges of the repeated units along the grain boundary. For instance, Figure 4.1 displays two types of phosphorene GB denoted as 5|7 and 4|8, which comes from the number of edges of the repeated units highlighted with blue and green shades.

Material's properties are strongly influenced by the GB type, as it was seen in a multiscale study of silicene GB, where the Kapitza thermal conductance varies according to the GB type and size, ranging the thermal modulation up to one order of magnitude of difference.[161] Other example of how GB induce changes in the properties of a material is with borophone, which, by the introduction of GB, the electronic states around the Fermi level are modified by backscattering, without loosing its metallic character.[162] The properties of phosphorene can be also modulated by GB, for instance, the θ_m and the GB lattice direction can modify their energetic,[163–165] mechanical stability,[166, 167] and electronic and thermal properties.[163, 168, 169] Moreover, it is interesting that the formation energy of GB phosphorene is lower as the required formation energy of other 2D GB, such as in graphene and MoS_2, as it was shown by a theoretical study where 19 different phosphorene GB were thermodynamically analyzed.[163] Also, in this study the authors highlighted that no major variations were found in the

electronic structure compared with pristine phosphorene, specially the absence of in-gap states and that the bandgap remained direct from Γ point to Γ point.

4.2 Computational approach

4.2.1 Molecular systems

As depicted in Figure 4.1, two phosphorene GB were considered for the investigation of their electronic, thermal and thermoelectric properties. The system denoted as GB1 (Figure 4.1 (a)) consists of two zigzag phosphorene monolayers with a θ_M of 26.8° forming a GB containing 5|7 defects. The second system, named GB2 (Figure 4.1 (b)), consists of two armchair phosphorene monolayers with a θ_M of 31.8° forming a GB containing 4|8 defects. These types of GB were selected because they are the most reported in experimental studies for other 2D materials[170–172] as well as in theoretical works of phosphorene GB.[164, 166]

DFTB method as implemented in the DFTB+ code[173] was used to carry the geometry optimization, electronic Hamiltonian matrix and interatomic force constant calculations. This method has been previously used for the simulation of the electronic and thermal properties of diverse low-dimensional materials.[174, 175] The Slater-Koster parameter set Mio-1-1[176] was used for the calculations, the geometry optimization was performed using the conjugate gradient method with a convergence threshold in forces of 10^{-5} a.u. and periodic boundary conditions were considered along the in-plane axis perpendicular to the transport direction (*i.e.*, GB direction). The strain in both systems was introduced along the transport direction, crossing the grain boundary.

4.2.2 Electron and phonon transport and thermoelectric figure of merit

The electronic and thermal transport properties where computed using the Atomistic Green's function formalism, introduced in Chapter 2. As described before, this formalism requires the usage of the common partition scheme which splits the system into three regions: two contacts and a device region, as shown in Figure 4.2. Each GB1 and GB2 contact consisted of 128 atoms and 50 atoms respectively, whilst 172 atoms and 92 atoms were included for each system in the device region.

The rows of atoms from the device region that are next to the contacts have the same unit cell as the contacts themselves, therefore the scattering is only expected to happen around the GB. This situation holds for systems with and without strain. The geometry optimization of the GB systems with applied strain was carried in a two-step calculation: first the atoms in the extremes of the device

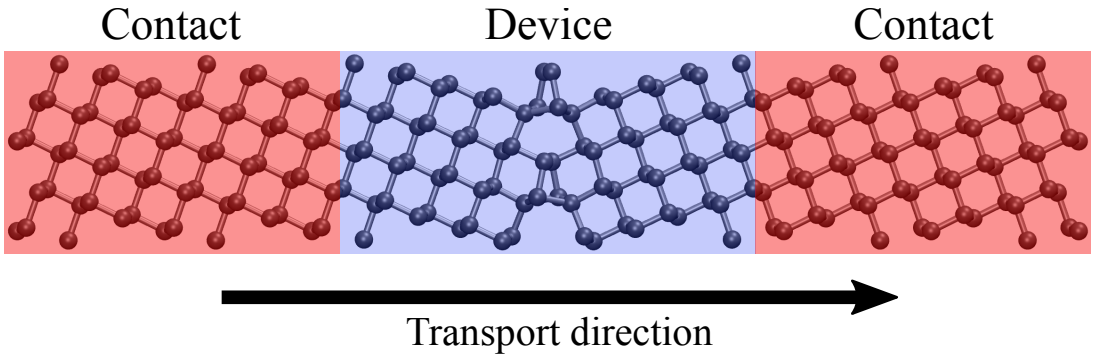

Fig. 4.2 Representation of the common partition scheme for electronic and phononic transmission calculations for phosphorene GB. Each contact region contains 128 atoms for GB1 and 50 atoms for GB2, while the device region includes 172 atoms and 92 atoms respectively.

were stretched along the transport axis and optimized the geometry, then the coordinates of the atoms in the transport axis were fixed and the structure went under a second geometry optimization to avoid additional strain. The strain level of the system is defined as $s = (L_s - L_0)/L_0$, where L_s and L_0 are the length of the whole system (device and contacts) along the transport direction with and without strain, respectively. The transport calculations were carried with periodic boundary conditions in the direction perpendicular to the transport axis.

Within the framework of nonequilibrium thermodynamics along the Landauer approach for transport, the thermoelectric transport properties of the GB systems were computed. Scattering processes under consideration in this framework are elastic and mediated by structural features of the system, hence, the phonon-phonon interaction is not taken into account through this approach. Additionally, electron-phonon coupling is not addressed, so electronic and phononic transport channels can be dealt separately. The thermoelectric figure of merit (ZT) is the main parameter of interest that defines the performance of a thermoelectric material, which is a dimensionless parameter defined as[177]

$$ZT = \sigma S^2 T/\kappa, \tag{4.1}$$

where ZT involves three parameters determining the efficiency of the energy conversion process: the electrical conductance σ, the Seebeck coefficient S and the thermal conductance κ, the later summing up both the electronic (κ_{el}) and phononic (κ_{ph}) components. Upon expansion of the electrical current under small applied voltage and temperature biases, the electronic transport coefficients that conform the figure of merit ZT can be calculated as

$$\sigma = e^2\Lambda_0, \tag{4.2}$$

$$S = \frac{1}{qT}\frac{\Lambda_1}{\Lambda_0}, \tag{4.3}$$

$$\kappa_{\rm el} = \frac{1}{T}\Big[\Lambda_2 - \frac{\Lambda_1^2}{\Lambda_0}\Big], \tag{4.4}$$

where q is the electric charge of carriers, positive for holes and negative for electrons, and the moments Λ_m involve the electronic transmission function $\tau_{\rm el}$ as

$$\Lambda_m = \frac{2}{h}\int dE(E-\mu)^m\Big[-\frac{\delta f(E,\mu,T)}{\delta E}\Big]\tau_{\rm el}(E), \tag{4.5}$$

with $f(E,\mu,T)$ being the Fermi-Dirac distribution function, μ the chemical potential and h the Planck constant. The μ is used as an independent variable to address the influence of doping on the system, since it can be related with the carrier concentration.

The electronic and phonon channels were framed independently, and the quantities of interest to be calculated where the electronic and phononic trasmission functions ($\tau_{\rm el}$(E) and $\tau_{\rm ph}(\omega)$,respectively). The $\tau_{\rm el}$(E) is computed as defined in Eq. (2.55) and the $\tau_{\rm ph}(\omega)$ as defined in Eq. (2.81, both in Chapter 2. The thermal conductance is then obtained as described in Eq. (2.82). The transport calculations were carried by the use of libNEGF[178] and PHONON[179] modules implemented in the DFTB+ code.

4.3 Structural modification by strain in GB systems

The thermodynamic stability of phosphorene GB1 and GB2 are first analyzed. To do so, the formation energy per atom ($E_{\rm form}$) of both GB systems were computed as[164]

$$E_{form} = \frac{\epsilon_{GB} - N\times\epsilon_P}{2L_0}, \tag{4.6}$$

where ϵ_{GB} is the energy of the GB system comprised by N phosphorus atoms, ϵ_P is the energy per atom of pristine phosphorene and L_0 is the length of the whole system. GB1 has a $E_{\text{form}} = 1.02$ eV/nm and GB2 has a $E_{\text{form}} = 1.56$ eV/nm, hence, GB1 is energetically more favorable and stable than GB2. Regardless of GB2 have a considerable higher E_{form} than GB2, both values range in a low formation energy, which is 0.9 - 2.43 eV/nm as reported in an extensive study about the energetic stability of phosphorene GB.[163] The low E_{form} can be attributed to the sp^3 hybridization of P atoms, which allows larger range of dislocations compared with other system with a sp^2 hybridization such as graphene. This is an insight of experimentally synthesize stable phosphorene GB.

After the information about the thermodynamic stability of the studied phosphorene GB was confirmed, the next step is to analyze the phosphorene GB structure after applying strain (perpendicular to the GB). Figure 4.3 displays the change in relative length $\Delta B_{\text{Fx}} = (B_{\text{Fx}}(s) - B_{\text{Fx}}(s=0))/B_{\text{Fx}}(s=0)$ of some relevant bonds Fx around the grain boundary as a function of the applied uniaxial strain s. In this definition, $B_{\text{Fx}}(s)$ indicate the bond length of bond F_x under strain and $B_{\text{Fx}}(s{=}0)$ is the corresponding equilibrium bond length in absence of any strains. The subindex x defines the number of the relevant bond shown in Figure 4.3 (a) and (c). Positive ΔB_{Fx} means an enlargement of the bond, while negative ΔB_{Fx} represents compression. In addition, two bond types are defined: in-plane (IP) and out-of-plane (OP) bonds, and their corresponding ΔB_{IP} and ΔB_{OP}, which follow the same protocol as ΔB_{Fx}, but by using the average values of B and B_0

In GB1 (Figure 4.3 (a, b)) the average ΔB_{IP} increases gradually with the applied strain (red filled circles), on the other hand a decrease in the OP bonds is seen (black filled circles). This behaviour can be justified by the quasi bi-layered structure of phosphorene and the presence of their voids in its structure, allowing the displacement of phosphorous atoms when the material is uniaxially stretched. The fact that the growth rate of the IP bonds length is larger than the reduction rate of the OP bonds highlights that this systems has a stronger dependence of IP bonds. By analyzing the individual IP bonds (labels F1, F2 and F3 in Figure 4.3 (a)), one can notice that the ΔB_{F2} and ΔB_{F3} has a close behavior to the average ΔB_{IP}, which mostly corresponds to the unit cell structure of the regions next to the GB. On the other hand, ΔB_{F1} has a larger bond enlargement than the average ΔB_{ip} value, justified by being a bond in connection to the GB and along the direction of the applied strain. In regard to the OP bonds (labels F4 and F5 in Figure 4.3 (a))), both bonds display similar strain dependence as the average ΔB_{OP}, but at larger strain (>8%) the ΔB_{F4} as a slightly larger deviation

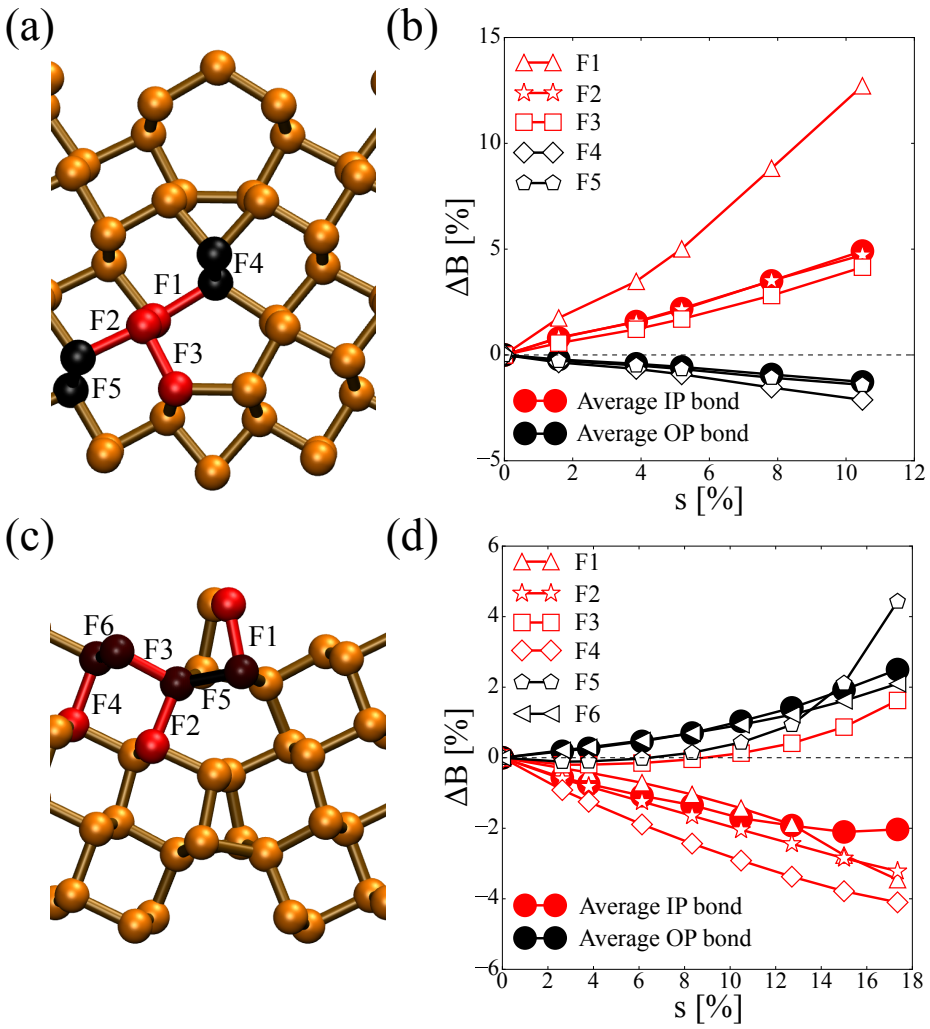

Fig. 4.3 Bond analysis of the device region in (a, b) GB1 and (c, d) GB2 systems with and without strain. Panels (a) and (c) show a top perspective of the GB and display in red and black relevant bonds in-plane (IP) and out-of-plane (OP) for its analysis. Panels (b) and (d) present the relative bond length change (ΔB) upon applied strain. The plotted values in red and black colors correspond to the IP and OP bonds, respectively. The empty markers display the values of the relevant bonds highlighted in panels (a) and (c), while the filled markers correspond to the average values over the whole device region.

of the average, this happens, again, as a consequence of this bond being part of the GB.

The IP and OP bonds of GB2 are displayed in Figure 4.3 (c, d), presenting a different trend as the one found in GB1, where the average ΔB_{IP} decreases with the applied strain and the average ΔB_{OP} increases. This suggest that the anisotropy in phosphorene plays a role in the IP and OP bond deformation under mechanical strain. Taking into consideration a path from left to right side of the GB2 system, which goes under an applied strain along the armchair direction, one can notice that the P atoms are connected by alternating IP and OP bonds, *i.e.*,

it is not possible to define a path that connects phosphorus atoms on the top layer from left to right without crossing through an OP bond. When in fact for the GB1, which strain is applied along the zigzag direction, paths connecting atoms from left to right in the top and bottom layers can be found without requiring any interlayer crossing. Other factor that distinguish GB2 system from GB1 are the positions of the atoms in the GB. Atoms in GB2 are positioned on different heights compared with atoms from the rest of the system, which might cause a different behavior in ΔB_{Fx} as a function of the applied strain. This can be specially seen in ΔB_{F1} and ΔB_{F5} (Figure 4.3 (c)), which show higher values after straining the system above 13%. These structural effects will have an impact on the electronic coupling, orbitals, band structure and force constant between the atoms in various regions of the systems, which then will have consequences in the electronic and phonon transmission properties as well as the thermoelectric properties, as it is presented in the following sections.

4.4 Electronic structure modification by strain in GB systems

The strain dependence of the electronic bandgap E_{gap} of GB1 (red line) and GB2 (blue line) is displayed in Figure 4.4(a). The GB systems initially without applied strain have larger E_{gap} than pristine phosphorene (black arrow), revealing that GB engineering can be used to tune the E_{gap} of the system. The effect on the E_{gap} depends on the synergy between the GB and pristine material, *e.g.*, the electronic bandgap of graphene was reported to open by the presence of GB,[180] while the opposite behavior was seen in GB MoS_2.[181] As displayed in Figure 4.4(a), the E_{gap} of GB1 increased till 2.0 eV and till 2.9eV for GB2, 1.1eV more than pristine phosphorene. After applying uniaxial strain, the E_{gap} of both GB slightly increase due to the compression of the quasi-bilayer structure, but then it decreases for $s \geq 5\%$. In fact, GB1 under strain reaches its highest E_{gap} of 2.1 eV at $s \approx 4$ and its lowest of 1.0 at $s \approx 10\%$, meanwhile GB2 reaches its highest E_{gap} of 3.0 eV at $s \approx 4$ and it goes down to 2.2 eV at $s \approx 18\%$. This implies that strains decrease E_{gap} up to 50% in GB1 and up to 24% in GB2. This strain-induced non-linear change of E_{gap} has been reported on graphene nanoribbons [182] and a hybrid system composed of graphane and fluorographane [183]. This effect can be justified by considering the location of the charge density with respect to the atoms and the elongation or contraction of the bonds after applying strain. When the distance between the atoms changes also does the interaction between their charge densities, causing an energy shift of the valence and conduction bands and an increase or decrease of the E_{gap} [184].

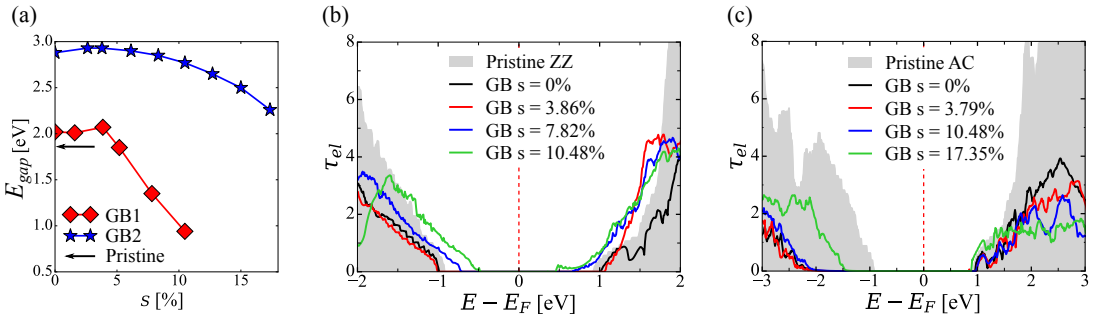

Fig. 4.4 (a) Electronic bandgap E_{gap} of GB1 (red) and GB2 (blue) systems as function of the applied strain. The horizontal arrow displays the position of the E_{gap} of pristine phosphorene without strain. Electronic transmission τ_{el} as a function of the energy for (b) GB1 and (c) GB2 without and with applied strain. The energy is normalized with the Fermi energy E_F. As a matter of reference, the corresponding transmission functions of pristine phosphorene in zigzag (ZZ) and armchair (AC) directions were included in the graphics as a grey background.

Moving to the electronic transmission τ_{el} of the GB (Figure 4.4(b, c)), clear differences are present between pristine phosphorene in zigzag (ZZ) and armchair (AC) directions with their respective GB systems with and without uniaxial strain. It is important to first remark that the absence of in-gap states in the transmission means that there are not unsaturated bonds in the strained system as a consequence of the GB formation, *i.e.*, even at high strain values there are not broken bonds. The suppression of the electronic transmission channels are caused by inclusion of the 5|7 defects to form the GB1 (Figure 4.4(b)). The decrease of the τ_{el} happens as a consequence of the scattering around the 5|7 defects and it comes with a slight increment of the E_{gap}.[185] The combinations of different factors, such as the symmetry change, bond length alteration and charge accumulation around the GB, plays a role to modify the τ_{el} of the system. For the strained systems, the τ_{el} of the GB1 with different strain values shows that the transmission probability closer to the Fermi level E_F, specially notable when the $s \geq 4.0\%$. Valence and conduction bands are shifted towards E_F, reducing the E_{gap}. The decreased E_{gap} of GB1 with $s = 10.48\%$ would be more favorable for doped-based electronic applications compared with its pristine counterpart, because the the system will require lower carrier concentration to reach the transmission channels.

On the other hand, AC phosphorene undergoes by a larger τ_{el} suppression the GB1 when the 4|8 defects are considered (Figure 4.4, where a notable decrease of the electronic channels in both valence and conduction emerges in consequence to the GB. Specially the valence bands are the most affected, leading to the previously presented increase of E_{gap} from 1.8 eV to 2.8 eV. The transmission probability for energies at the band edges are only slightly modified by the small

strain levels, which is similar to the GB1, but , but when $s \geq 10\%$, the transmission probability increases again and the valence band edge is shifted towards E_F. The transmission probability for the energy levels at the conduction band edge ($\sim$ 1 eV) also increase with the strain, but, for levels farther than these ones ($\geq$ 1.8 eV), the probability decreases.

To sum up the presented information of this section, 5|7 (GB1) and 4|8 (GB2) defects bring down the electronic properties of their corresponding pristine counterparts, specially GB2 presented a more remarkable effect by increasing the electronic bandgap by $\sim 50\%$. At low values of uniaxial strain ($s \leq 4.0$ for both systems) both GB have similar effects in their τ_{el}, but at larger values of s, the transmission probability of energy levels in the valence and conduction bands become dependent of the GB topology.

4.5 Thermal transport modification by strain in GB systems

The influence of the in-plane (IP) and out-of-plane (OP) bonds described in Section 4.3 are expected to change the thermal transport properties of both GB. The phonon transmission τ_{ph} and the corresponding thermal conductance κ_{ph} of the GB at different applied strains are displayed in Figure 4.5. Additionally, τ_{ph} and κ_{ph} of the pristine phosphorene along zigzag (ZZ) and armchair (AC) directions are included in the graphic.

There is an overall decrease in the τ_{ph} of GB1 (black line in Figure 4.5 (a)), as expected, as a consequence of the scattering originated by the 5|7 defects. This effect is larger seen at higher frequencies, in the range of the optical branches ($\omega > 250$ cm^{-1}), where also the applied strain causes the largest effect. Even new transmission resonances ~ 300 cm^{-1} emerged, closing the phonon gap found in both the strainless GB1 and the pristine phosphorene (ZZ direction). To reveal the origin of such additional states, a projected phonon density of states was computed for GB1 at different strains (see Appendix B.1, which revealed that these resonances are mainly produced by the strain-induced vibrational modes of atoms in the phosphorene regions excluding the GB atoms. This effect serves as an evidence of how strain can be employed for phonon engineering in GB. On the other hand, regarding the long-wavelength modes of GB1 ($\omega <$ 40 cm^{-1} are moderately affected at small strain levels ($s < 50\%$), but their τ_{ph} is constantly reduced for larger s.

The τ_{ph} in GB2 is suppressed, similarly as in GB1, by the inclusion of the 4|8 defects compared with the τ_{ph} of pristine AC phosphorene (Figure 4.5). But, at difference to the previous GB, there is a considerably larger suppression on

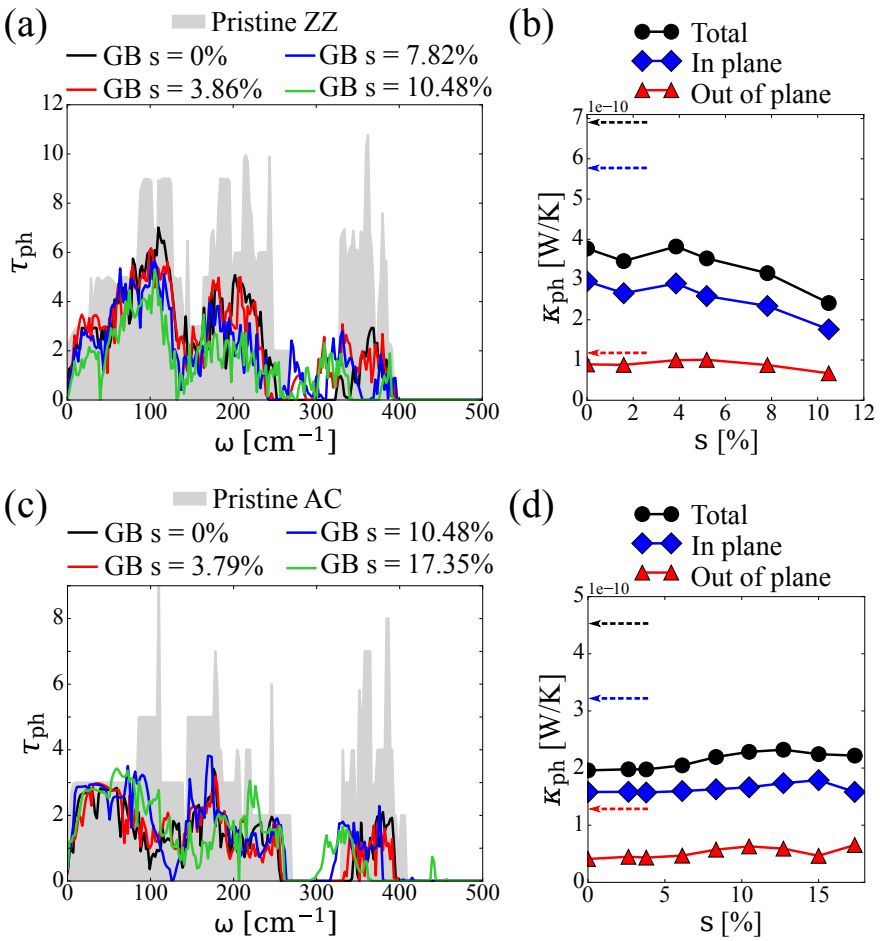

Fig. 4.5 Phonon Transmission τ_{ph} as function of the frequency ω of (a) GB1 and (c) GB2 without and with applied strain. As a matter of reference, τ_{ph} of pristine phosphorene in ZZ and AC directions were also included (gray background). Thermal conductance κ_{ph} as function of the strain for (b) GB1 and (d) GB2. The total κ_{ph} is represented in black lines, while the IP- and OP-conductance are displayed in blue and red, respectively. The κ_{ph} of pristine phosphorene are showed with dashed arrows in the left side of the panels.

vibrational modes with $\omega > 80$ cm^{-1}. Besides the effect generated by the defects, it can be notice that the exerted strain does not affect uniformly the frequency spectrum of GB2 as it was seen in GB1. Nevertheless, there is a reduction of the phonon gap around 300 cm^{-1} because of the constant shift of the optical modes towards lower frequencies when the s of the system increases, which does not close as it was the case for GB1. This strain-induced phonon shift effect has also been reported in materials involving MoS_2 and WS_2.[186]

The total κ_{ph} was projected into their IP and OP contributions, as seen in Figure 4.5(b, d)), to get a better insight of the thermal transport properties of the GB. Compared with pristine ZZ phosphorene (black line), there is a decrease of the κ_{ph} by 40% down to 3.8$\times$ 10^{-10} W/K after including the 5|7 defects to form the GB1 system. When $s > 4\%$ is applied in the system, κ_{ph} remains

almost unaltered, but when $s > 4\%$, κ_{ph} decreases, which is correlated with the corresponding τ_{ph}. There is a notable value that goes out of the trend ($s = 3.86\%$) by increasing slightly, which may correspond to the increase of transmission probability in the low frequency range ($\omega < 50$ cm^{-1}). In terms of IP and OP contribution analysis (blue and red lines respectively) of the total κ_{ph}, the IP-modes dominate the thermal transport properties of both pristine and GB1 systems. For this 5|7 defects decreased the IP-κ_{ph} by almost 50%, while the OP-κ_{ph} is only reduced by ∼10%. Therefore, it is clear that the IP-κ_{ph} of GB1 is largely influenced by uniaxial strain compared to the OP-κ_{ph}, which is in agreement with the IP and OP bond length analysis discussed in Section 4.3.

However, a different trend from the GB1 can be seen for the κ_{ph} of GB2 (Figure 4.5(d). First, the addition of the 4|8 defects decreases the total κ_{ph} by more than 50% compared with the pristine AC phosphorene. Then, κ_{ph} remains almost constant regardless the applied strain, with small variations when $s > 5\%$. This quasi-constant behavior of κ_{ph}in GB2 is correlated with the τ_{ph} at different strain values (Figure 4.5 (c)), where only minimal changes are noticeable in the phonon spectrum, specially in contrast with GB1 (Figure 4.5 (a)), which displays a constant decrease of τ_{ph} in the whole spectrum. Finally, in relation to the IP and OP contributions to κ_{ph}, compared to the pristine AC phosphorene, the formation of 4|8 defects caused a drop to 50% in the IP-κ_{ph} and 65% in the OP-κ_{ph}. Moreover, similarly as the total κ_{ph}, both IP- and OP-κ_{ph} remain almost constant up to s 15%, from which a IP-κ_{ph} decreases and OP-κ_{ph} increases in similar proportion, keeping unaltered the total κ_{ph}.

A deeper explanation of the strain dependence of IP- and OP-κ_{ph} ca be carried by correlating the discussed results with their respective τ_{ph}, as displayed in Figure 4.6. IP- and OP-τ_{ph} of pristine ZZ and AC phosphorene were included as comparison. In both GB, IP-modes have larger transmission probability and cover almost the whole frequency spectrum than the OP-modes, which are mostly located at low and very high ω. This justifies the predominance of the IP-modes in thermal transport properties of both GB. In GB1, IP-τ_{ph} decreased and OP-τ_{ph} stayed almost constant when uniaxial strain is applied in the system, which is expected by the previous discussion of the κ_{ph}. Additionally, the transmission peaks that emerge in the phonon gap at ~ 300 cm^{-1} can be correlated to the IP-modes.

Comparing GB2 with pristine AC phosphorene, the addition of the 4|8 defects highly decreased OP-τ_{ph} above $\omega > 100$ cm^{-1}, increasing the phonon gap located around $\omega = 250$ cm^{-1}. IP- and OP-τ_{ph} of not present strong modification when $s < 10\%$, which is proportional to the almost strain-independent behavior

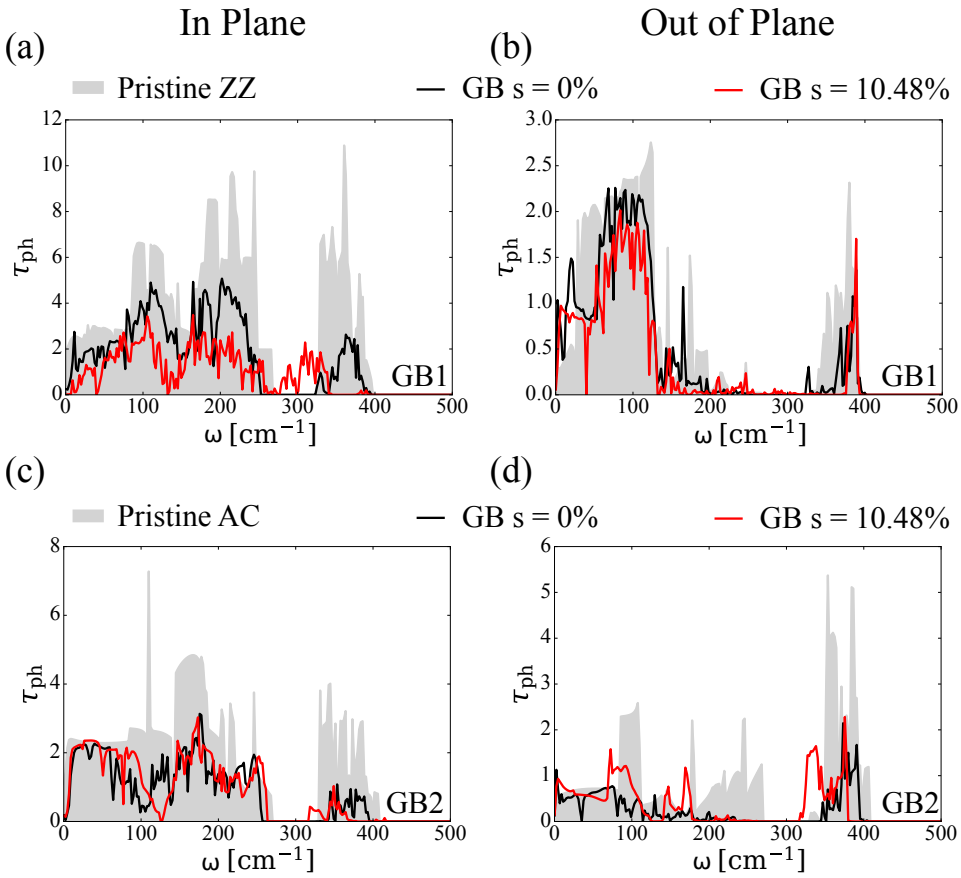

Fig. 4.6 (a, c) In plane (IP) and (b, d) out-of-plane (OP) contributions to the total phonon transmission τ_{ph} as a function of the frequency ω for GB1 and GB2 without and with applied strain. As a sake of reference, the IP and OP contributions to the total τ_{ph} for pristine ZZ and AC phosphorene are included as a gray background.

associated with κ_{ph}. By looking to system when the $s = 10.48\%$, one can notice an enhancement of both IP- and OP-τ_{ph} at low ω ($\sim$100 cm^{-1}), which can cause the small increase presented in the total κ_{ph} in Figure 4.5 (c).

4.6 Thermoelectric figure of merit of strained GB systems

After discussing the effects of the strain on the electronic and phonon transport properties in phosphorene GB, the discussion proceeds towards the analysis of the thermoelectric performance. As introduced in the Section 4.2 and defined in Eq. (4.1), the thermoelectric figure of merit ZT involved three basic quantities that determines the efficiency of the energy conversion: the electrical conductance σ, the Seebeck coefficient S and the thermal conductance κ. The latter quantity is composed by the electronic κ_{el} and phononic κ_{ph}.

The κ_{el}, S and power factor ($PF = \sigma S^2$) of the GB1 with different values of strain as a function of the chemical potential μ at 300 K and 600 K are displayed

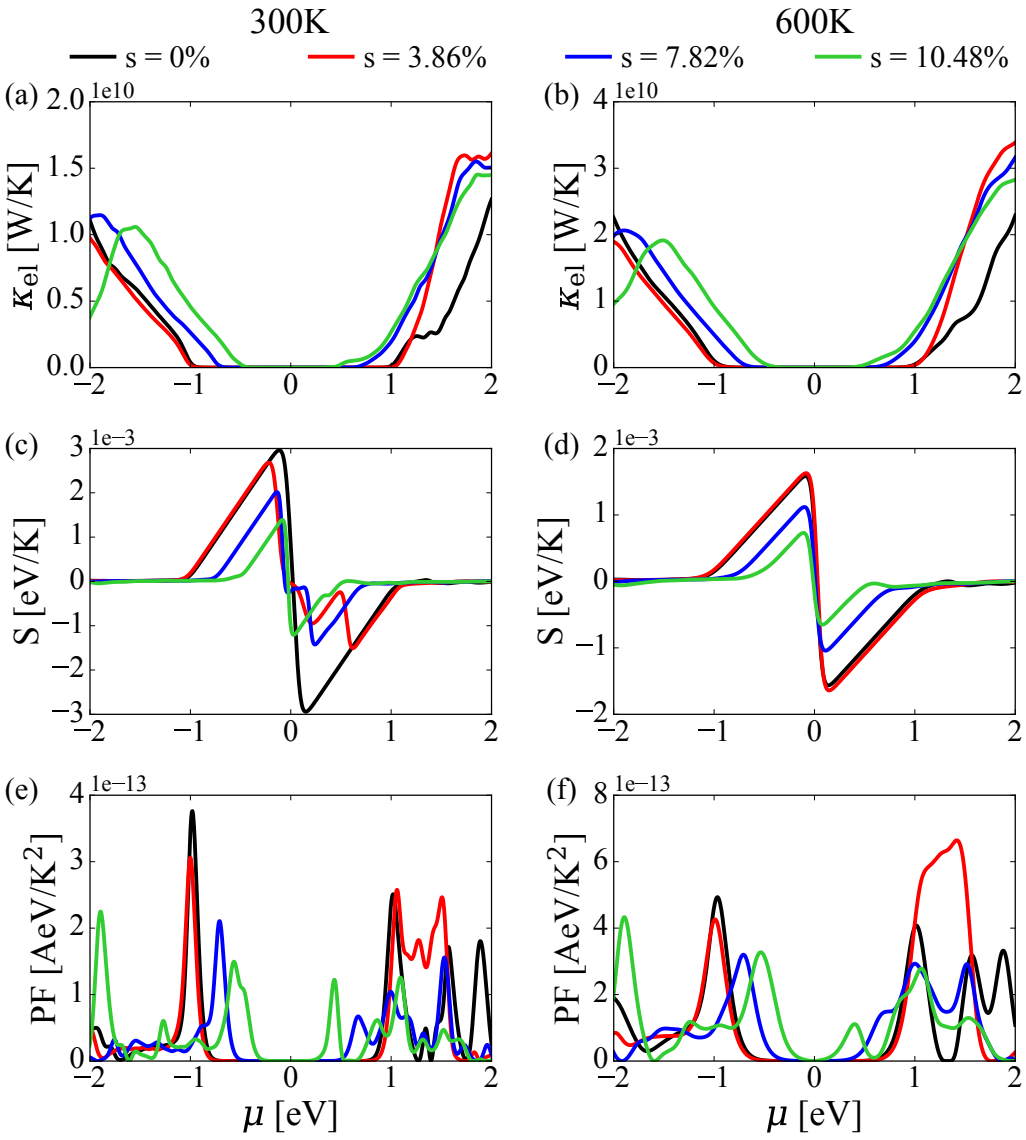

Fig. 4.7 Thermoelectric transport properties of GB1 at 300K (left side) and 600 K (right side) at different values of strain, displaying the variation in the (a, b) electronic contribution to the thermal conductance (κ_{el}, (c, d) the Seebeck coefficient (S) and (e, f) the power factor (PF) as a function of the chemical potential μ.

in Figure 4.7. For the sake of clarity, positive μ corresponds to n-type doping while negative μ to p-type doping. The κ_{el} (Figure 4.7(a, b)) has a similar profile as τ_{el}, discussed previously from Figure 4.4(b). The overall κ_{el} of all the strained systems increases with the raise of the temperature due to the large broadening of the Fermi function derivative under the integrals of the Λ_m moments in Eq. (4.5). A high value of ZT requires a low κ_{el}, and the discussed GB1 systems do not show a considerable decrease of κ_{el} when the strain is modified, only the κ_{el} corresponding to the valence and conduction bands move towards the E_F.

In regard to S of GB1 (Figure 4.7(c, d)), the system at $s = 0\%$ shows a clear

electron-hole symmetry at both temperatures, however, the strained systems display at 300 K a more involved behavior with relatively sharp changes on the n-type doping side (positive μ). But when the temperature raises, the S profile of the strained systems recovers its electron-hole symmetry. Comparing the maximum values at 300 K, the strainless systems have the largest S value (3×10^{-3} eV/K) and then this decreases in proportion to the strain, reaching 1.4×10^{-3} eV/K when $s = 10.48\%$. When the temperature increases in the system, the S decrease for all the systems, but the decrease ratio of the GB1 at $s = 3.86\%$ is lower than the other systems, which can be noticed in the plot at 600 K, where that system and the strainless GB1 have almost the same S profile, with a highest value of 1.7×10^{-3} eV/K.

Moving to the PF (Figure 4.7 (e, f)), the GB1 without strain displays the best performance compared with the strained systems at room temperature, with a value of 3.8×10^{-13} AeV/K^2 at μ = -1 eV. The highest PF near the neutral point (μ = 0 eV) for the other systems decreases in proportion to the strain and shifts towards a lower value of doping concentration, which means that, in practical terms, applying strain to GB1 can facilitate the doping for its use in thermoelectric devices. The PF increases with the temperature for all the systems, but in the system with $s = 3.48\%$ there is a larger enhancement in the negative-doped side of the plot (μ = 1 to 2 eV). On the other hand, the system with higher s are even closer to the neutral point, easing their approach through doping. Similar thermoelectric analysis for GB2 can be found in Appendix B.2.

The maximum attainable value of the ZT (ZT_{rmmax}) as a function of temperature of both GB systems at different uniaxial strain values is displayed in Figure 4.8. For reasons of clarity, the ZT_{rmmax} considered in this discussion is the maximum value obtained at each temperature in the optimal μ. In absence of any applied strain and at room temperature, the optimal thermoelectric performance of GB1 and GB2 is 0.28 and 0.43, respectively. This results is interesting because both GB displays larger ZT than pristine phosphorene, reported to have $ZT \sim 0.2$ at room temperature.[187]

When the temperature increases, the ZT of $s = 0\%$ monotonously increases in a quasi-linear behaviour, where GB2 system shows in general a larger ZT. This trends is most ostensible related to the fact that the τ_{ph} of GB2 is considerable lower than GB1. As it was displayed in 4.5 (a, c), the τ_{ph} in the frequency range around $\sim$ 100 cm^{-1} of GB1 is almost three times larger than in GB2. Although the PF of GB1 is considerably large (Figure 4.7(e)) because of the higher electronic conductance, the ZT is reduced due to the larger impact of the heat conductance denominator in Eq. (4.1).

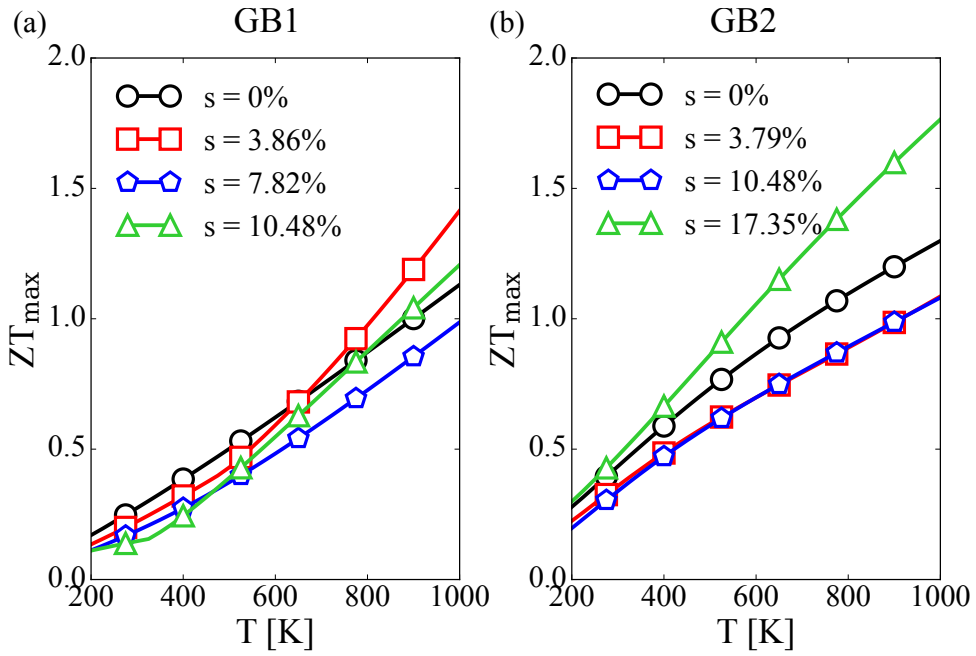

Fig. 4.8 Temperature dependence of the maximum value of the figure of merit (ZT_{max}) of (a) GB1 and (b) GB2 at different values of strain. (ZT_{max}) is considered as the maximum value obtained at each temperature in the optimal chemical potential μ.

After applying uniaxial strain in GB1, ZT decreases in proportion to the strain at room temperature, from 0.28 in the strainless system to 0.15 when $s = 15\%$. There are two effects that can explain this behavior: namely the increase of the κ_{el} around the optimal μ (Figure 4.7(a)) while increasing the strain in the GB, and the decrease of S (Figure 4.7(c)). On the contrary, the strained GB2 system display a different tendency when the uniaxial strain is applied. For the GB2 systems with $s = 3.79\%$ and $s = 10.48\%$, the ZT increases but has nearly the same values over the whole temperature range, when compared to the strainless system. But when the strain goes up to 17.35%, in contrast, GB2 outperforms all other systems.

4.7 Summary

In this chapter, the structural, electronic, thermal and thermoelectric properties of two types of phosphorene grain boundaries, including 5|7 and 4|8 defects, were studied under applied strain along the transport direction (perpendicular to the defects). This was carried by combining a density functional based tight binding approach with the atomistic Green's function method. The structural modification of phosphorene was discussed through a bond analysis, which sowed that in-plane bonds of GB1 have a higher stretch-ratio with the applied strain

compared with the out-of-plane bonds. Contrary, GB2 system showed an opposite and irregular behaviour due to the orientation of the phosphorene layers. In regard to the electronic transport properties, the grain boundary formation rises the electronic bandgap of both systems. Nevertheless, the applied strain tends to decrease the gap. With respect to the phonon transport discussion, 5|7 defects (GB1) considerably decrease the total transmission in the whole spectrum, which then induce a decrease in the thermal conductance that then continue its decrease with the applied strain. On the other hand, GB2 system displayed a decrease of the phonon transmission mostly above 100 cm^{-1}, which also resulted in a decrease of the thermal conductance, but, contrary to GB1, the applied strain increased slightly the transmission. Despite the fact that the electronic transmission and the corresponding power factor of GB1 are larger than GB2, the larger thermal conductance of GB1 promoted an overall small value of the figure of merit than for GB2. Regardless of that, both GB systems outperforms the figure of merit of pristine phosphorene.

The presented results in this chapter are of interest for the potential design of phosphorene GB systems towards thermoelectric devices, since it was shown that the structural defects have a different influence on the electronic and phononic transmission function and, therefore, on the corresponding linear electronic and thermal conductance.

CHAPTER 5

Tuning transport properties through hybrid nanomaterials: CNT peapods

In the previous chapters the transport properties of 2D materials were discussed by means of functionalization, strain and structural defects. There are other nanomaterials of interest due to its transport properties that their scale go below the 2D, such as one-dimensional (1D) nanowires and nanotubes and zero-dimensional (0D) nanoparticles and quantum dots. Moreover, the combination of these types of structures as hybrid nanomaterial may be able to introduce different properties as of the individual components, which makes them of high interest for the research and development of new technology.

In this chapter, the electron and phonon transport, as well as the thermoelectric properties of carbon nanotubes (CNT) modified by C_{60} encapsulation, referred as CNT peapods, are approached. Within a DFTB framework, the influence of C_{60} molecules in the transport properties of CNT are analyzed and compared with its pristine counterpart to resolve whether or not this hybrid nanomaterial can be an outstanding material for the development of thermoelectric devices. This chapter relies on Ref. [188]

5.1 Introduction

5.1.1 Carbon-based nanostructures

Carbon is one of the most widely distributed element in nature that is the basis for life and also is important for many technological applications, ranging from pharmaceutics to artificial materials. Carbon's utility is a consequence of its ability to bind to other carbon atoms as well as almost all elements in large variety, resulting in diverse molecules and organic compounds accompanied by an extensive range of physical and chemical properties.

For a long time, elemental carbon was known to exists in nature only in three allotropic forms: as diamond, graphite and amorphous carbon. Each form has their own unique physical properties such as thermal conductivity, hardness or

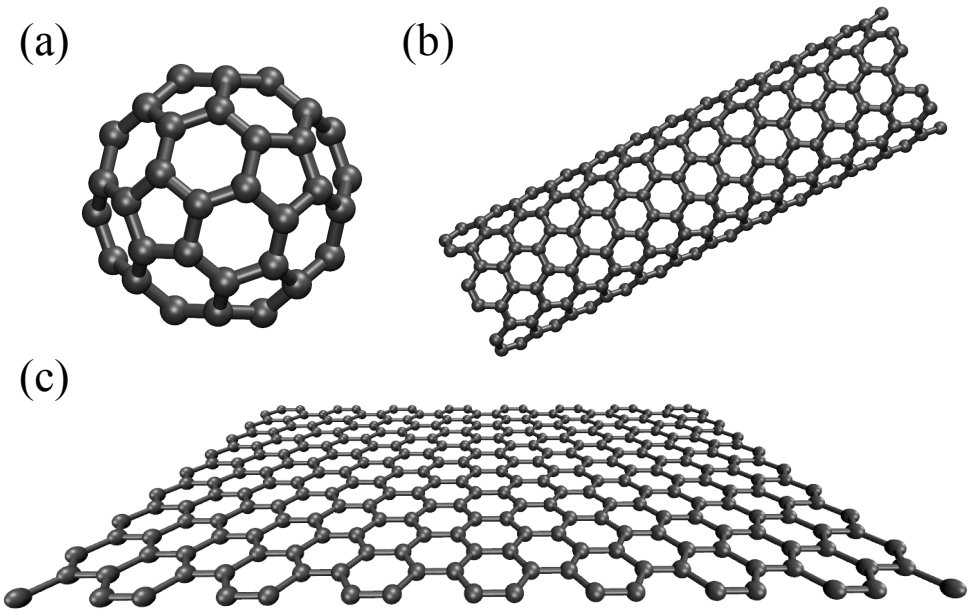

Fig. 5.1 Atomistic representation of the three most known allotropic carbon nanostructures: (a) fullerene (OD), (b) carbon nanotube (1D) and (c) graphene (2D).

electrical conductivity. The extended network of carbon atoms of each allotropic form was responsible of their properties. In theory, by altering the periodic arrangement of the carbon network, new structures, some of them crystalline, with remarkable properties would emerge, which, in consequence, opened the research in the preparation of such materials in macroscopic quantities. After several years, new allotropic forms of carbon were discovered in the nanoscale.[189–191]

In the last decades, carbon nanomaterials have been one of the focus centers of research due to their unique mechanical, electronic, optical, thermal and chemical properties, altogether with the high abundance of the element carbon in the earth, provide scientists the tools for a significant advance in fundamental and applied science and the promising development of breakthrough carbon-based technology. The main carbon-allotropic nanomaterials are graphene (2D),[192] carbon nanotubes (1D)[193] and fullerenes (0D)[194] (Figure 5.1), but other forms such as graphyne[195, 196] are under research in theoretical and experimental work.

The first alotropic non-natural form of carbon was discovered in 1985, corresponding to the Buckminsterfullerene, or just fullerene, by Harold Kroto's group. [197] In his experiments, graphite was vaporized by laser irradiation, producing stable clusters consisting of 60 carbon atoms in the shape of an icosahedron. Inspired by the fullerene finding, in 1991, carbon nanotubes (CNT) were first discovered by a research group lead by Iijima.[198] The length and diameter of CNT are very characteristics, hence, they became an influential parameter in

the theory of research and application perspective. Its length go up to a micron, but the diameter is in the range of nanometers, which results in a large length/diameter ratio. CNT's structure reassembles a cylindrical molecule with a hexagonal arrangement of carbon atoms that are sp^2 hybridization, with a inner hollow structure. It can be seen as a sheet of graphene rolled up. Depending of the number of sheets, CNT can be classified as single walled CNT when is composed of one graphene sheet whereas multiwalled CNT when is composed of more than one sheet. In the experiments of Iijima's group, the multiwalled CNTs were first spotted, and later on, by the addition of a metal catalyst in the experimental setup, the synthesis product would lead to the formation of single-walled CNTs.[198, 199]

The CNT properties largely depend on its structure, from which three main geometries can be classified according to their diameter and helicity, described by their chiral vector. This vector, specified with the indexes n and m, is defined as the vector that connects crystallographycally two equivalent sites of a graphene sheet and along it "wraps itself" to form the CNT, *i.e.*, a chiral vector describes the circumference vector of the CNT. The CNT with the chiral vector (n,0) are defined as zigzag, (n,n) as armchair and (n,m) as chiral. Moreover, electronic band structure calculations predict that the chiral indexes determine CNT's electronic behaviour, where it is metallic if $n - m = 3q_c$, otherwise it is a semiconductor, with q_c as an integer.

In regard to the electronic properties of CNT, their electronic structure is described on the basis of graphene's band structure, in which the valence and conduction bands touch at six points at the Fermi energy, forming the Dirac cones.[200] Moreover, an individual feature of one-dimensional materials is that their electronic density of states is not continuous in function of energy, but rather consists of discontinuous spikes, which are known as Van Hove singularities, as a consequence of quantum confinement effects.[201] The energy difference between the Van Hove singularities is correlated to the diameter of the CNT, hence, CNT's bandgap depends on diameter and chiral indexes. CNT can carry an electrical current flow density of 4×10^9 A/cm^2 which is larger than current flow density in metals like copper.[202] Besides the interesting electronic properties, thermal properties in CNT are also of interest for the scientific community. CNT exhibit a property known as ballistic conduction, has a thermal conductance of 2.4 nW/K and its thermal conductivity is nearly 3500 W/mK at room temperature. [203]

The exceptional mechanical, electronic and thermal properties of CNT unlock a diverse range of application such as transistors, fibers, membranes, transparent conductors and thermal interfaces. The application is sometimes influenced by

the synthesis method, since this one dictates the properties of the CNT, like length, helicity, alignment, diameter and density. For other cases, the synthesis method plays a passive role to determine their applications since the parameters controlled by the synthesis do not relate to the performance or processing requirements of making a device or applications.[204]

In the field of transistors, experimental studies of CNT in realistic conditions of field effect transistors have shown outstanding properties, in particular interest the high current carrying capacity, ultrafast carrier velocity and excellent electrostatics.[205] Compared to thin film transistors constructed from conventional materials, CNT offer the possibility to outperform them by exhibiting higher current-drive, energy-efficiency and sensitivity.[206] On the other hand, in the field of thermal management, the extraordinary high axial thermal conductivity of CNT have made them candidates for low resistance thermal interface materials. This can have an impact in the new technological designs that increase the density of transistors per square area, because a better heat dissipation is demanded. [207]

5.1.2 CNT peapods as hybrid nanomaterials

CNTs have the capability of hosting ions or molecules inside their cavity, as far as the dimensions of the CNT diameter and the hosted molecules do not cause uncomplimentary steric effects.[208] A particular case being is the so called CNT peapods, where CNTs with adequate diameters encapsulates arrays of fullerene molecules distributed along the nanotube axis. Their properties may vary depending on the interaction between the atoms of the CNT wall and the fullerenes. For instance, the electronic structure of the CNT peapods near the Fermi level depends on the space between encapsulated fullerenes and the nanotube, where a shift in the bands of the CNT can be influenced by the π electron states of the fullerenes.[209, 210]

In regard to the thermal properties of CNT peapods, the effect of the fullerene molecules was not yet fully elucidated. Early experimental studies of the thermal conductance of C_{60}@CNT peapods as well as classical Molecular Dynamics simulations of thermal transport in C_{60}@CNT(10,10) systems have stated that there is an enhancement of the thermal conductance, since the C chains provide additional transport channels by an efficient low-frequency C_{60}-C_{60} energy transfer in the axial direction.[211, 212] Nevertheless, a later study carried out by Kodama's group[213] addressed the thermal conductance and thermopower of bundles of CNT peapods, encapsulating normal C_{60} as well as endohedral fullerenes (Gd@C_{82} and Er@C_{82}), and found that the thermal conductance along

the bundles was suppressed by 35-55%, as well as the thermopower increased by about 40% with respect to the pristine CNTs at room temperature. These results are explained by relating the strong local interaction between the fullerenes and the nanotube, which caused local structural deformation in the nanotube walls. Nevertheless, the presented classical Molecular Dynamics simulations were not conclusive since the deformation of the CNT wall was only achieved after artificially increasing the strength of the fullerene-CNT van der Waals interaction.

Following computational studies[214, 215] showed that C_{60} molecules are capable of inducing additional phonon scattering, therefore reducing the phonon mean free path and the thermal conductance. This decrease was mainly seen in the low-frequency region of the spectrum, where CNT(9,9) peapods where considerably reduced compared with its pristine CNT, while this effect was negligible for larger size diameter CNT peapod.[214] This clearly indicates that the impact of the fullerenes on the thermal conductance is related to the CNT radius, which control the strength of the CNT-C_{60} interaction.

5.2 Computational details

5.2.1 CNT peapod model

The main system consisted of an infinite (8,8) metallic single-wall carbon nanotube with C_{60} fullerene molecules encapsulated along its inner section in a periodic array as depicted in Figure 5.2 (a). This combined system is denoted as C_{60}@CNT(8,8) or CNT peapod. The CNT(8,8) was studied in this system to ensure its interaction with the encapsulated C_{60} molecules, hence, proceed with the understanding of its impact on the thermoelectric transport properties.

C_{60}@CNT(8,8) geometry optimization was carried out by using the second-order self-consistent charge density functional tight-binding (DFTB2) method[71, 216] as implemented in the DFTB+ code (version 1.3),[173] employing the Slater-Koster parameter set "matsci-0-3".[72] Intermolecular interactions between C_{60} and CNT were considered by means of Lennard-Jones dispersion correction,[217] employing parameters from the universal Force Field.[218] The structure with minimal energy was computed through the conjugate gradient method, setting a convergence threshold for the forces of 1×10^{-5} atomic units. The system's unit cell was constructed by a C_{60} molecule and four rows of CNT atoms, whose diameter's length is similar as of the fullerene (0.71 nm), as projected in Figure 5.2(b). The reciprocal space was sampled by a grid of (25×1×1) k points.

As a matter of clarity, some preliminary tests on CNT peapods with (9,9) and (10,10) nanotubes showed a strong suppression of the CNT-C_{60} interaction

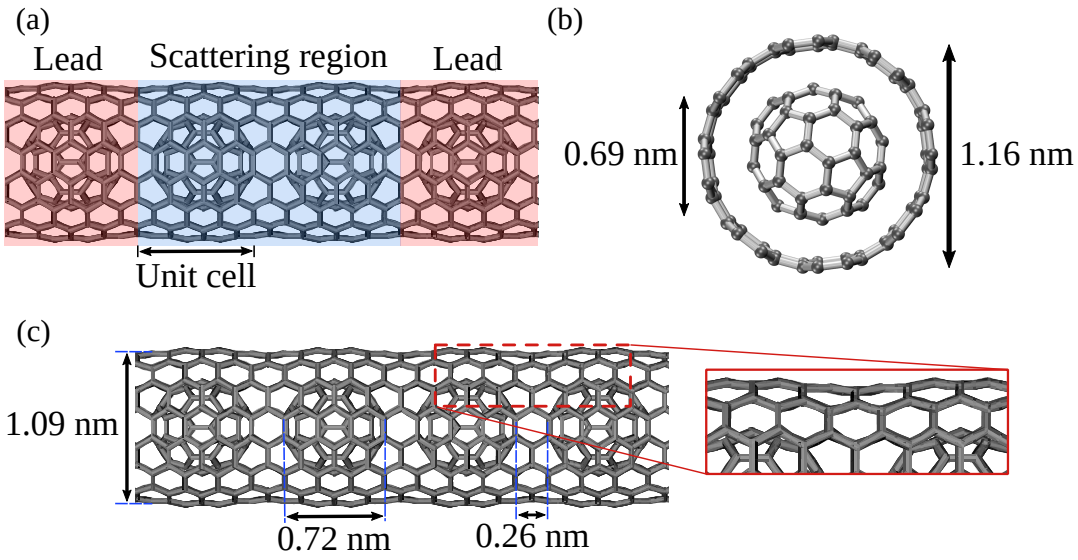

Fig. 5.2 (a) Schematic representation of the common partitioning scheme for the transport calculations. The unit cell (delimited with the black arrow) contains four rows of carbon chains and a C_{60}. Each lead was constructed with two unit cells and the scattering region with three unit cells. (b) C_{60}@CNT(8,8) cross-section perspective, marking the diameters of the C_{60} (0.69 nm) and of the CNT (1.16 nm). The later value correspond to the distorted section due to the presence of the C_{60} molecule. (c) Molecular representation of C_{60}@CNT(8,8) after geometry optimization. The CNT diameter in the section between fullerenes is 1.09 nm, the spacing between the closest consecutive C_{60} molecules is 0.26, and the diameter of the C_{60} along the axial plane is 0.72 nm. The right panel highlights a local bulking of the CNT around the C_{60} molecules. As noticed in the given dimensions of the C_{60} molecules, they are deformed in a slightly ellipsoidal shape.

due to the larger distance between the fullerenes and the atoms of the CNT, making them less relevant for the study of their theremoelectric properties effect (see Appendix C.1). Geometry optimization carried out with more accurate implementation of van der Waals corrections like DftD4[219] and many body dispersions implemented in DFTB+[173] did not show a slight modification of the final structures closer to the obtained by employing the CNT(8,8). Therefore the main discussion is centered in the (8,8) system and sometimes the other two systems are used only for comparison.

5.2.2 Quantum transport methodology

The thermoelectric transport properties of the C_{60}@CNT(N,N) (N=8,9,10) were computed under the non-equilibrium thermodynamics framework along the Landauer approach for transport. The protocol for the calculations was as described in Section 4.2. For sake of clarity, different energy and frequency resolutions were tested to correctly resolve small features in the transmission functions for

electrons and phonons, respectively. The optimal values were set for the results present in this chapter.

5.3 Structural properties of CNT peapods

The first characteristic to evaluate in the C_{60}@CNT(8,8) systems is its mechanical stability. To perform it, C_{60} molecules were initially placed along the nanotube central axis with different intermolecular distances. As a matter of reference, pristine CNT (8,8) diameter was used for comparison (1.09 nm). After geometry optimization, fullerenes adopted a periodic arrangement with an intermolecular distance of 0.26 nm. Additionally, the perfect icosahedron is slightly modified and deviated from their spherical shape, acquiring a semi ellipsoidal shape with dimensions of 0.69 nm in the axial plane and 0.72 nm along the CNT. On the other hand, the nanotube surface displays local deformation around the fullerene location, as a result of the non covalent C_{60}-CNT(8,8) interaction, which leads to a periodic buckling, as can be seen in Figure 5.2(c). An additional test to confirm the optimal C_{60} orientation was made by optimizing the C_{60}@CNT(8,8) geometry with three different C_{60} orientations with respect to the CNT wall.[220] After geometry optimization, the three different geometries ended in the same orientation, where a hexagon-hexagon pair of the C_{60} is facing a hexagon on the CNT surface, as seen in Figure 5.2 (b).

The CNT diameter around the center of the fullerene expands from 1.09 nm to 1.16nm, while the diameter in the fullerene-free region, bottleneck, remains as 1.09 nm. Hence, the local buckling is $\sim$ 0.07 nm. The optimized distance between the nearest atoms of C_{60} and CNT is 0.235 nm, which means that not only van der Waals interactions can take place, but also a direct, though weak, overlap of the electronic molecular orbitals of the two systems may play a role.

The described local expansion of the CNT walls around the fullerenes and the slight compression of the C_{60} molecules get weaker or completely disappear for the C_{60}@CNT(9,9) and C_{60}@CNT(10,10) due to the larger separation between fullerenes and the CNT walls, as displayed in Figure 5.3. A slight buckling of just 0.01 nm is formed in the C_{60}@CNT(9,9) system, meaning that a possible interaction may still exist between the hosted molecules and the CNT. On the other hand, structural changes are not present in the C_{60}@CNT(10,10) system, which may lead to almost unnoticeable effects in their thermoelectric properties. As stated before, the C_{60}@CNT(8,8) contains the optimal dimensions to understand the effect of the fullerene encapsulation in their thermoelectric properties.

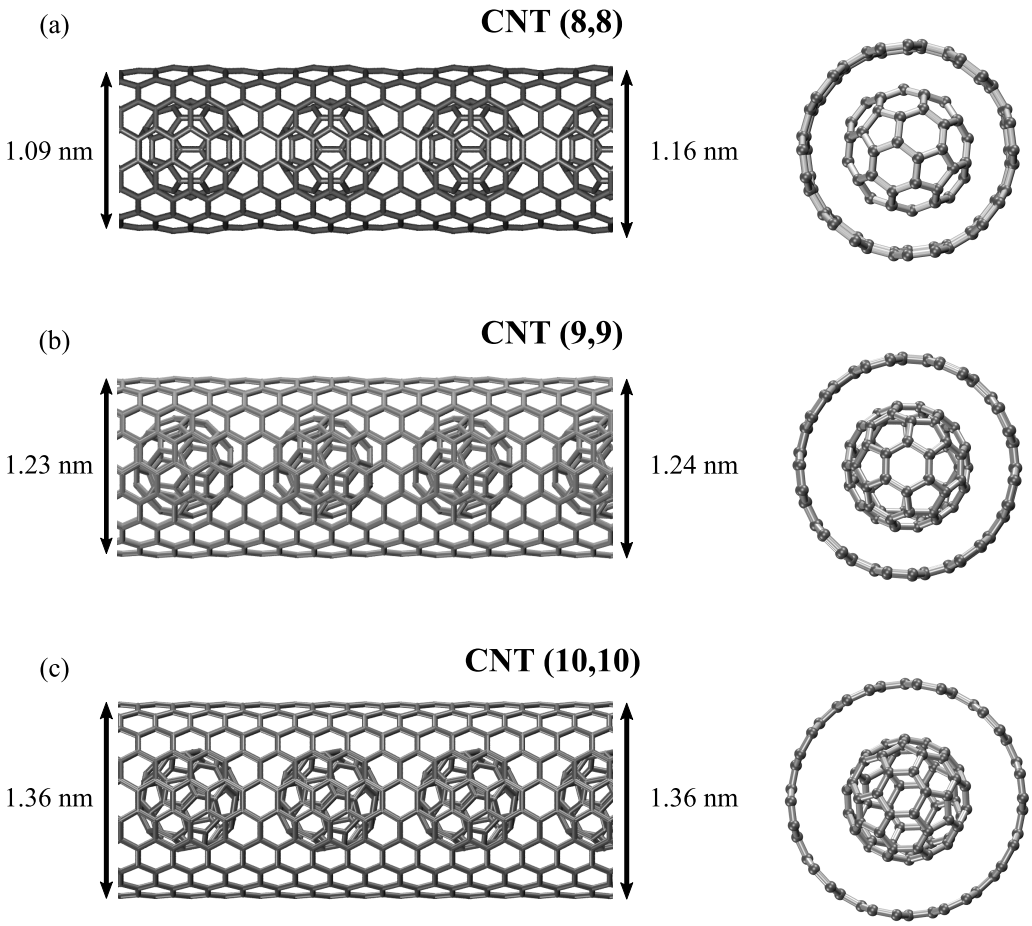

Fig. 5.3 Side perspective and cross section of atomistic representation of (a) C_{60}@CNT(8,8), (b)C_{60}@CNT(9,9) and (c) C_{60}@CNT(10,10) after geometry optimization. The CNT diameters of the bottleneck and around the center of the C_{60} molecules are displayed. An enlargement of the CNT diameter around the fullerenes.

5.4 Electronic properties of CNT peapods

The electronic transmission function τ_{el} of the optimized C_{60}@CNT(8,8) system was computed and displayed in Figure 5.4 (a). As a sake of reference, the τ_{el} of pristine CNT (8,8) was computed (gray background). Pristine metallic CNT transmission exhibits a typical low-energy plateau around the Fermi energy with $\tau_{\mathrm{el}} = 2$. Under the linear response regime, the corresponding electrical conductance is given by $G = G_0\tau_{\mathrm{el}}$, where $G_0 = e^2/\hbar$ is the conductance quantum. Beyond the lowest conductance plateau, the well known transmission staircase behavior is displayed in the rest of the τ_{el} plot, as additional electronic bands get involved in the transport process.

On the other hand, C_{60}@CNT(8,8) shows a considerably irregular behavior. Even though traces of the CNT staircase pattern can still be spotted in the whole energy spectrum, smaller and larger transmission probability in different energy

windows appear when compared to pristine CNT(8,8). It is of interest to highlight a decrease of the electronic transmission in the energy range -0.7 to -0.9 eV and around 0.5 eV, which decreases from the plateau of the CNT down to ∼1. Contrary to this, within the range from -0.3 eV to -0.6 eV, an enhancement of the transmission is displayed which is larger than pristine CNT, reaching up to 4. Unbinding these effects, the transmission suppression by one channel in the energy range [-0.7,-0.9] eV may be justified to quantum interference effects. This by considering that the C_{60}@CNT(8,8) system can be seen as a conducting channel with a periodic side dot along the transport channel. In this type of setup, it is well-known that quantum interference can lead to different spectral features such as Fano resonances, anti-resonances, etc.[221, 222] Specially the anti-resonances lead to a suppression of the transmission at specific resonant energies. To prove the validity of this qualitative scheme, the electronic transmission of a simplified system consisting of a CNT peapod but with a single fullerene in the scattering region was computed and compared with an empty CNT peapod with the periodic buckling, referred as distorted CNT (see Appendix C.2). A suppression of the transmission around the same energy region was found, with a profile fitting the described anti-resonance situation. This effect disappear in case the of the distorted CNT.

To understand better the second effect, about the transmission enhancement in the interval [-0.6, -0.3] eV, the total and projected density of states (PDOS) of the C_{60}@CNT(8,8) were computed (Figure 5.4 (b)). Only the p-states of the carbon atoms have been considered during the PDOS computation. A strong spectral overlap of the CNT (black line) and fullerene (green line) states is present in the range from -0.3 eV to -0.6 eV, indicating hybridization between the corresponding electronic states, and hinting a strong contribution of C_{60} atoms to the transmission probability at this energy range. Hence, the enhancement in the transmission probability to 4 can be related to additional transport pathways involving the C_{60} molecular chain. Moreover, the fullerenes possess almost zero spectral weight in the energy interval between 0 eV and +0.8 eV, causing that the electronic transmission probability remains at the value of pristine CNT (= 2). To deeper understand the role of the C_{60} in the transmission increase around -0.5 eV, the τ_{el} was computed of a system in which the intermolecular distance along the C_{60} array was fixed at a larger value of 0.49 nm. In consequence, the C_{60}-C_{60} interaction of the array is considerable weakened. The results presented in Appendix C.2 show that now only transmission suppression is visible at various energies ranges along the spectrum, specially around the region [-0.6, -0.3] eV, *i.e.*, there is no enhancement above the CNT plateau τ_{el}. Beyond that region, the

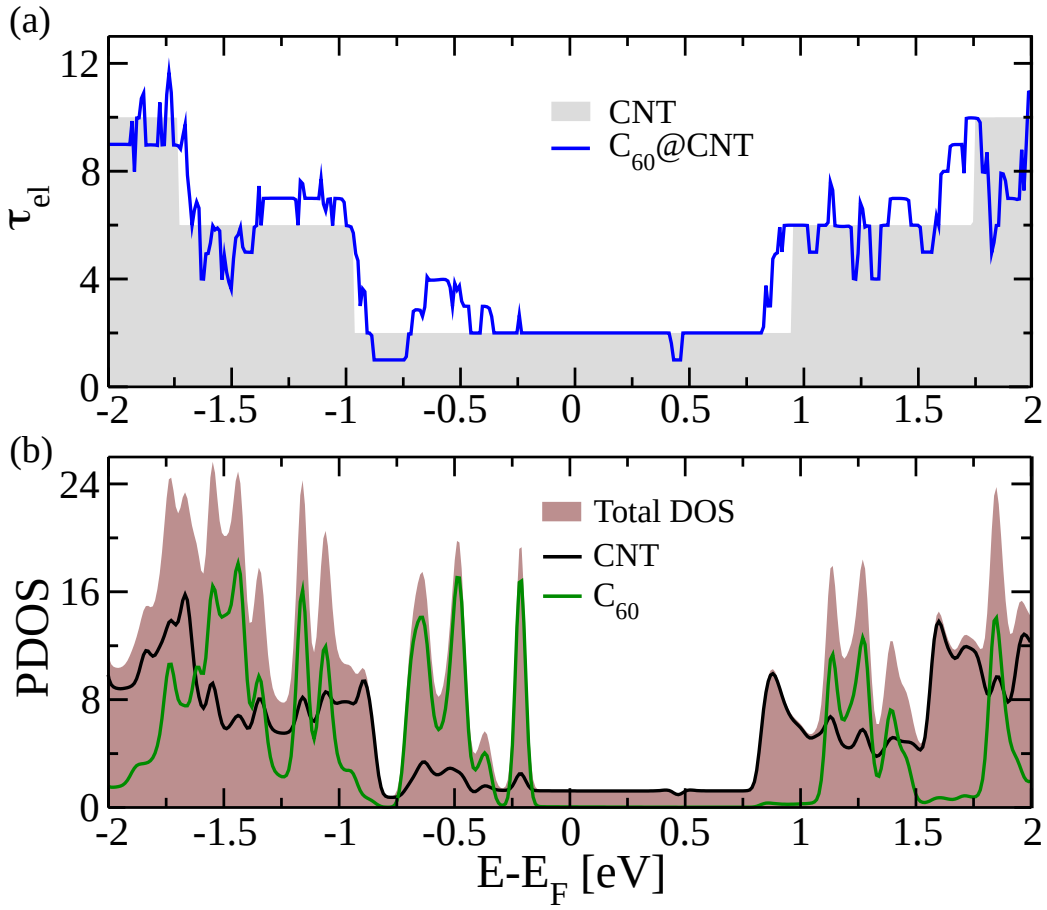

Fig. 5.4 (a) Electronic transmission function τ_{el} of C_{60}@CNT(8,8) and pristine CNT (8,8) displayed with a blue line and a gray background. (b) Projected density of states (PDOS) involving the carbon p-orbitals for CNT and fullerene atoms in black and green lines respectively. The DOS and PDOS correlates with the energy regions where the electronic transmission is most strongly modified.

decreased transmission due to the larger C_{60}-C_{60} distance is displayed between -1.0 and -1.5 eV. These effects indicate that the electronic coupling between the fullerenes plays a major role in the enhancement of the electronic transmission probability.

However, it is difficult to provide an intuitive justification for the enhancement or suppression of transmission for all the energy windows, since a delicate interplay between the emergence of additional transport pathways and local quantum interference effects, both of which are in function of the involved electronic states at specific energies. It is also important to remark that the dip at 0.5 eV in Figure 5.4 (a) is related to a small gap in the electronic band structure of the CNT around the Z-point, as it is shown in the Appendix C.2. Nevertheless, this spectral feature is no expected to affect significantly in the overall thermoelectric transport properties of the CNT peapod.

Further calculations employing larger size CNTs (9,9 and 10,10) are pre-

sented in the Appendix C.2. The results highlight the strong interaction that is presented in the C_{60}@CNT(8,8) and con have an impact in the electronic transmission. The spectral features in the electronic transmission discussed before are weak when the peapod system is constructed with larger diameter CNTs, at the point that such features disappear and the transmission remains more similar as the corresponding pristine CNT.

5.5 Thermal properties of CNT peapods

After discussing the effects of hosting C_{60} molecules in the τ_{el}, in this section the discussion will be centered in the thermal transport properties. The phonon dispersion along the $\Gamma \longrightarrow Z$ path for pristine CNT (as a reference), distorted CNT and C_{60}@CNT(8,8) systems were obtained through using the PHONON tool. The dispersion at low frequency (ω = 0 - 250 cm-1) of the three systems are displayed in Figures 5.5(a-c). In Figure 5.5 (c), dispersionless bands emerges below 50 cm-1, which correspond to local modes, and interact with the CNT acoustic modes, leading to a flattening of the acoustic branches and, thus, to a reduction of the group velocities. These modes can be attributed to the fullerenes, since they are absent in the distorted CNT (Figure 5.5). This type of behaviour has been published in phononic metamaterials research with engineered nanopillars,[223–228] and also found as a result of a substrate deposition of nanomaterials.[229–232]

The phonon transmission τ_{ph} of C_{60}@CNT(8,8), distorted CNT and pristine CNT(8,8) are displayed in Figure 5.5 (d). The peapod system (blue line) displays a considerable suppression of the transmission probability at low-frequency modes below 500 cm-1, reflecting the described effect of the band structure displayed in Figure 5.5 (d), and even stronger suppression for high-frequency modes above 1500 cm-1. In a previous CNT peapod study carried by Wan and Jiang[], through classical molecular dynamics simulations, the transmission suppression at low-frequency range was also found. Although the effect described in Figure 5.5 (d) is stronger than as reported because of the smaller CNT diameter employed in this system.

To distinguish and measure the effect caused by the periodic buckling of the distorted CNT and the presence of the fullerenes in the phonon transmission function, the following quantity is defined:

$$R_X(\omega) = [\tau_{\text{ph}}^{CNT}(\omega) - \tau_{\text{ph}}^{X}(\omega)]/\tau_{\text{ph}}^{CNT}(\omega), \tag{5.1}$$

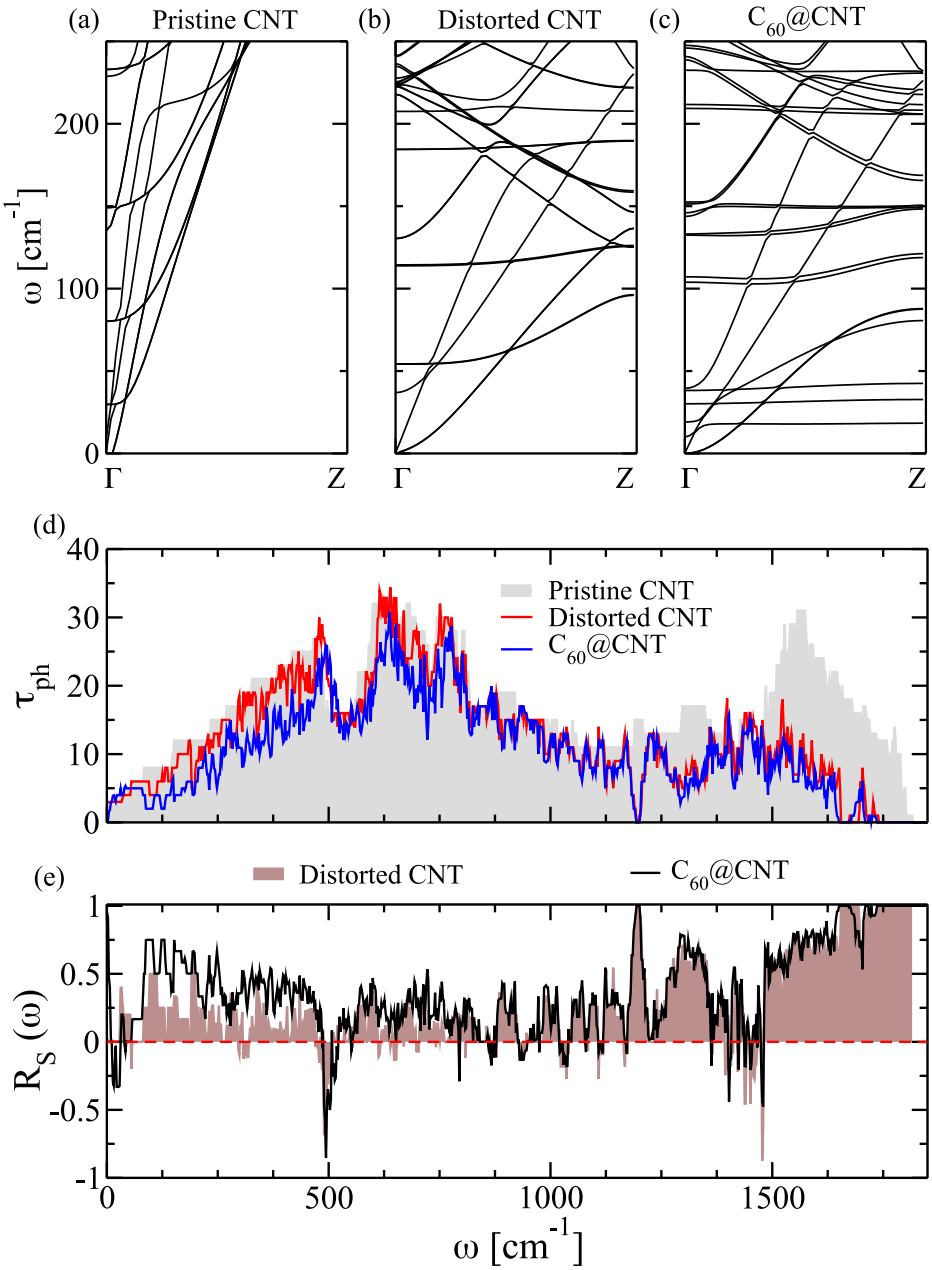

Fig. 5.5 Phonon dispersion along $\Gamma \longrightarrow Z$ (transport direction) of (a) pristine CNT(8,8), (b) distorted CNT (8,8) and (c) C_{60}@CNT(8,8) systems at low frequencies (0-250 cm-1). (d) Phonon transmission $\tau_{\rm ph}$ as a function of the frequency ω for distorted pristine CNT, distorted CNT and C_{60}@CNT(8,8) in gray background and red and blue lines, respectively. Suppression at low and high frequency ranges are noticed. (e) Deviation of the phonon transmission in reference to the pristine phosphorene, described under the function $R_X(\omega) = [\tau_{\rm ph}^{CNT}(\omega) - \tau_{\rm ph}^{X}(\omega)]/\tau_{\rm ph}^{CNT}(\omega)$, where X refers either to the full C_{60}@CNT(8,8) or the distorted CNT, displayed with a black line and a brown background respectively.This R_X function distinguishes the spectral regions where the local distortions of the CNT walls dominate the conductance from those where the contribution from the presence of C_{60} molecules have a stronger effect.

where X refers either to the complete C_{60}@CNT(8,8) system or the distorted CNT. If the ratio $R_X \sim 0$, then the transmission probability is similar to that of the pristine CNT, meaning that the peapod system is not affecting the modes at that frequency rage. While $R_X \sim 1$ indicates a strong suppression of the transmission, eventually leading to the formation of a phonon band gap. But if the $R_X < 0$, it means that additional phonon channels have emerged or a shift of the CNT transmission frequencies took place. By comparing the results between distorted CNT and C_{60}@CNT(8,8) from Figure 5.5 (e), the modes above $\omega > 1500$ cm-1 are suppressed by the local periodic deformation in the nanotube, which is in agreement with he phonon dispersion results. Additionally, the spectral phonon gap around 1200 cm-1 is related to the distorted CNT, even though few flat vibrational bands are display close to the spectral gap (see Appendix C.3) On the other hand, in the low-frequency range of the spectrum ($\omega < 500$ cm-1), the R_X of the distorted CNT differs considerably from the C_{60}@CNT(8,8), indicating that the presence of the C_{60} molecules plays a stronger role in that frequency region. Hence, they are the main source of the transmission reduction (Figure 5.5(d)), and, evidently, this reflects the previous discussion of the vibrational band structure (Figure 5.5(c))

5.6 Thermoelectronic properties of CNT peapods

The following step in the research, after gaining a deepr insight into the electronic and vibrational transport properties of the CNT peapod, is to proceed the discussion into its thermoelectric transport properties. To fulfill a comparison, the pristine CNT is considered as a reference point. Figure 5.6 displays the electronic contribution to the thermal conductance κ_{el}, the Seebeck coefficient S, and the power factor PF of the pristine CNT and C_{60}@CNT(8,8) as a function of the chemical potential μ at 300 K and 600 K. As defined in Chapter 4, n-type doping is represented as a positive μ, while a p-type doping as a negative mu.

Figure 5.6(a, b) displays the κ_{el} at 300K for both systems, which has a similar pattern as the κ_{el} from Figure 5.4(a). At 600 K, the overall κ_{el} increases due to a larger broadening of the Fermi function derivative under the integrals of Λ_m in Eq. 4.5 (see Section 4.2). On the other hand, stronger differences can be seen in the S between both systems. The S of pristine CNT shows a clear electron-hole symmetry for both temperatures, and when the temperature increases only the broadening of the peaks increases. In regard to the C_{60}@CNT(8,8), the S displays a more involved behavior, like the lack of symmetry with respect to the charge neutrality point and the presence of relatively sharp changes in the sign of S of the p-type doping side (negative μ). This behaviour is a consequence of the

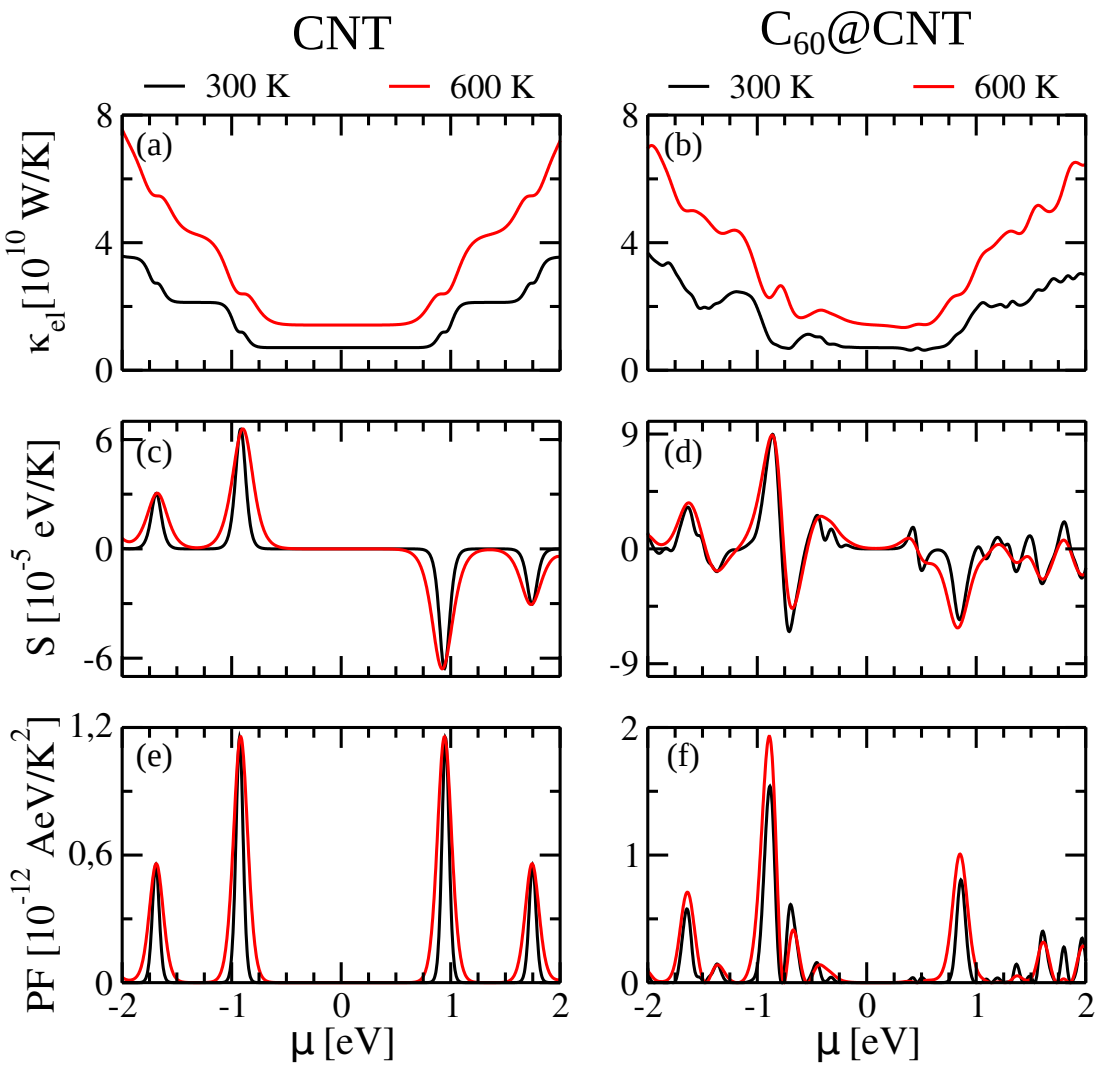

Fig. 5.6 Thermoelectric transport properties of pristine CNT (left side) and C_{60}@CNT(8,8) (right side) at 300 K and 600 K (black and red lines, respectively). Variation in the (a,b) electronic contribution to the thermal conductance (k_{el}), (c,d) the Seebeck coefficient (S), and (e,f) the power factor (PF) as a function of the chemical potential μ are displayed. Here, the C_{60}@CNT(8,8) system displays an asymmetric behaviour with respect to the charge neutrality point ($\mu = 0$ eV).

strong C_{60} molecules influence in the electronic transmission since the distorted CNT almost keeps the same behaviour as the pristine CNT (see Appendix C.4). Moreover, the largest change in S takes place in an energy window around $\sim$ -1 eV, where the influence of the C_{60} is seen most strongly in the electronic transmission spectrum (Figure 5.4. Comparing both systems, C_{60}@CNT(8,8) possesses a larger S_{max} compared to the pristine CNT for both temperatures, where S_{max} is defined as the maximum S value as a function of the μ. The S_{max} of C_{60}@CNT(8,8) is $\sim$8.9x10^5 eV/K at μ = -0.86 eV and the S_{max} of CNT $\sim$ 6.58x10^5 eV/K at μ = -0.9 eV at 600 K.

Regarding the PF results (Figure 5.6 (e, f)), pristine CNT, similarly as its S,

retains the same electron-hole symmetry. But the behaviour of C_{60}@CNT(8,8) is, again, asymmetric with respect to the charge neutrality point, however, it reaches a higher PF_{max} value than the pristine system. That is it, at 600 K, the PF_{max} of C_{60}@CNT(8,8) is $\sim$1.93x10^{-12} AeV/K^2 at $\mu = -0.88eV$ and of CNT is $\sim$1.15x10^{-12} AeV/K^2 at $\mu = \pm 10.91$ eV. Summing up all the discussed electronic contributions to the thermoelectric figure of merit, the C_{60}@CNT(8,8) system displays a better efficiency in a wider range of temperatures (T = [250, 100] K), where the maximal efficiency is presented at 575 K (See Appendix C.4).

The electronic and phonon contribution (κ_{el} and κ_{ph}, respectively) to the total thermal conductance for pristine CNT and C_{60}@CNT(8,8) as a function of the temperature are displayed in Figure 5.7 (a). The κ_{el} for each temperature is obtained as the maximum value of the electronic thermal conductance at the optimal μ. In general, the κ_{ph} dominates over thermal conductance for both CNT and C_{60}@CNT(8,8) systems. Nevertheless, both contributions become very proximate to each other for C_{60}@CNT(8,8) at the highest temperature in this study (1000 K).

The C_{60} encapsulation displays a larger impact in κ_{ph} compared to κ_{el}, where the latter is only slightly affected when going from the pristine CNT to the peapod, and the former is gradually reduced when increasing the temperature with respect to pristine CNT values. Notwithstanding the fact that a crossover around 650 K in the curves of κ_{el} of both systems is displayed, both systems remain with a small difference for any other temperature, below 5%. Moreover, the κ_{ph} of C_{60}@CNT(8,8) almost saturates after 750 K, denoting that all the relevant vibrational states have been included in its computation, see Eq. 2.81.

The thermoelectric parameters of CNT peapods with larger diameter (9,9 and 10,10) at 200 K and 600 K are included in the Appendix C.4. At difference to the C_{60}@CNT(8,8) results, the reason behind choosing different temperatures for the other systems is justified by the fact that the optimal results for theses systems are found at lower temperatures than for C_{60}@CNT(8,8). Comparing CNT(9,9) and C_{60}@CNT(9,9), minor differences were found in the κ_{el} between both systems, but regarding S, considerable differences are found, where C_{60}@CNT(9,9) presents more changes and a decrease of S for the p-doping region and an increase of the S for n-doping region. This result contrasts with the discussed C_{60}@CNT(8,8), where a notorious increased S was found in the p-doping region. In terms of PF, the n-doping region of C_{60}@CNT(9,9) at 200 K is 1.2 times the PF of CNT(9,9), achieving a value of $\sim$ 1.44x10^{-12} AeV/K^2. The enhancement of C_{60}@CNT(9,9) in that region corresponds to the increase in electronic transmission shown in the electronic transmission at $\sim$0.8 eV in Figure C.4 in

Appendix C.2, due to the incorporation of the C_{60} molecules. Regardless of this increase, the interaction between the C_{60} molecules and the CNT(9,9) is not as remarkable as it was displayed in the C_{60}@CNT(8,8), and even this becomes more evident when treating the C_{60}@CNT(10,10), in which both parts of the system (C_{60} molecules and CNT) behave as if they were decoupled from each other.

After analyzing the resulting thermoelectric parameters of C_{60}@CNT(8,8) and CNT, the discussion proceeds towards the thermoelectric figure of merit ZT. The heat map in Figure 5.7(b) displays the ZT of C_{60}@CNT(8,8) system as a function of temperature and μ. This type of plot serves to allocate the optimal μ value for each temperature, which leads to a maximum ZT, ZT_{max}. Based on the discussion of the electronic contribution to the ZT (Figure 5.6, an asymmetric behaviour with respect to the neutrality point for the ZT plot is expected and displayed in Figure 5.7(b). The optimal value of μ is situated at $\sim$-0.9 eV, pointing that the maximal performance is located in the p-type doping region. Regarding the n-type doping region, at $\sim$0.9 eV is located other μ region with high performance, but it reaches up to $\sim$ 0.8, just 66% of the maximal performance in the p-type doping region.

The temperature dependence of ZT_{max} can be extracted and plotted for C_{60}@CNT(8,8) system from Figure 5.7(b), as it can be seen in Figure 5.7(c). Similar to the PF_{max} trend displayed in Figure C.7 in Appendix C.4, the ZT_{max} of C_{60}@CNT(8,8) is also larger compared to the value of pristine CNT over the whole displayed temperature range. At 575 K is reached the highest thermoelectric performance with $ZT_{max} = \sim$0.12. This correspond to an enhancement of the thermoelectric efficiency by a factor of 2.2 using the ZT of CNT as a reference, which weakly depends on the temperature. This indicates that hosting fullerenes may lead to a more sensitive temperature control of the thermoelectric response. The performance of CNT peapods with larger CNT diameter are displayed in Figure 5.7(c), where C_{60}@CNT(9,9) shows a small enhancement of ZT at low temperatures, which represents a sim1.3 factor larger than the pristine CNT(9,9) at 200 K ($ZT_{max} \approx 0.074$). On the other hand, the C_{60}@CNT(10,10) displays a similar ZT profile as pristine CNT(10,10), as a consequence of the almost negligible influence of C_{60} molecules in their electron and phonon transport properties.

5.7 Summary

In this chapter, a detailed computational study of the thermoelectric properties of a hybrid one-dimensional system, C_{60}@CNT(8,8) system, was carried

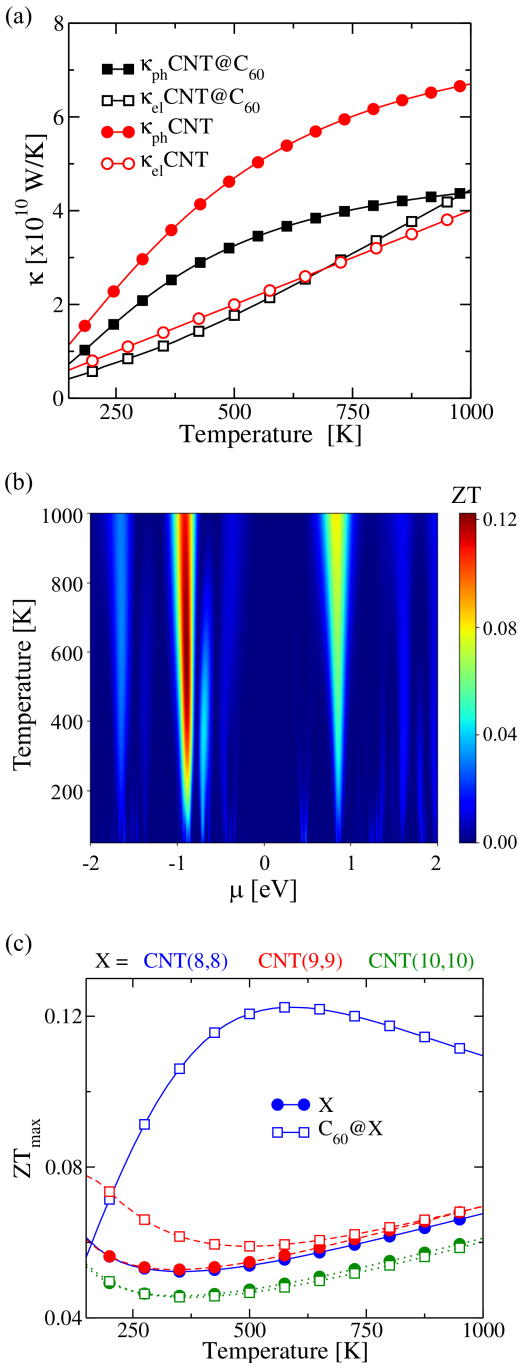

Fig. 5.7 (a) Thermal conductance of CNT and C_{60}@CNT(8,8) (red circles and black squares, respectively) as a function of temperature. The curves with filled symbols correspond to the phonon thermal conductance κ_{ph}, while the empty symbols correspond to the electronic thermal conductance κ_{el} (for each temperature its maximum value when plotted as a function of the chemical potential μ is taken). (b) Heat map plot of the figure of merit ZT in function of the temperature and chemical potential μ for C_{60}@CNT(8,8). (c) Temperature dependence of the maximum value of ZT for pristine CNT(n,n) and C_{60}@CNT(n,n) (circles and squares, respectively) for different CNT diameters (n = 8 blue, = 9 red, = 10 green). The thermoelectric performance of C_{60}@CNT(8,8) is enhanced by a factor of 2.2 compared to pristine CNT(8,8) at 575 K, where $ZT_{max} \approx 0.12$.

out using the DFTB-NEGF framework. These findings indicate that the presence of C_{60} molecules along the inner cavity of the CNT and the related local buckling induced by their mutual interaction display a significantly role in the electronic and thermal properties of the system. Among others, a strong modification of the low-energy (around the Fermi level) electronic conductance was presented, demonstrating both conductance suppression and conductance enhancement when compared with the pristine CNT case, which displays a constant conductance plateau with $G = 2G_0$. Regarding the phononic transmission, a decrease at low and high frequencies were displayed as a consequence of the hybridization of local C_{60}-derived modes with acoustic modes (in the low-frequency range) and also from the periodic buckling along the CNT surface (in the high-frequency range). Even though the total thermal conductance is still dominated by the vibrational contributions, the previously mentioned suppression of the phononic transmission over various spectral windows leads to an overall reduction of the thermal conductance for C_{60}@CNT(8,8) when compared with pristine CNT. This, combined with a large power factor, resulted in an improved thermoelectric figure of merit for the CNT peapod. The resulting values of ZT are still small compared with other thermoelectric materials, however, this hybrid system ended in an enhancement by a factor of 2.2 when compared with the individual pristine CNT at 575 K and, additionally, the ZT of the peapod reflects a more pronounced temperature dependence trend. These results highlight the importance of strong CNT-C_{60} intermolecular interactions. On the other hand, the weakened response in the electronic and thermal properties of CNT peapods with larger diameter indicate the importance of the interaction distance when designing hybrid molecular systems.

In fact, the displayed dominant effects on the studied systems of both C_{60}-C_{60} and C_{60}-CNT interactions offer an additional set of variables to influence the thermoelectric transport properties of CNT- and other 1D-based systems. The selection of larger nanotube radii can control the C_{60}-CNT interaction, while the encapsulation of other empty fullerenes or endohedral fullerenes can influence both C_{60} and C_{60}-CNT interactions.[213] Furthermore, the conformational freedom of the fullerene chains in these CNTs may be larger and also adopt arrangements differing from the linear periodic chain presented in this chapter, but this is not the subject of this study. The insights presented here may inspire future experimental and theoretical works for the development of CNT-based thermoelectric devices.

CHAPTER 6

Conclusions and outlook

In the presented thesis, density functional theory and density functional based tight binding methods have been employed to investigate the structural, electronic, magnetic, thermal and thermoelectric properties of low dimensional systems.

The first part focused on the electronic properties of functionalized phosphorene. In Chapter 3, the properties of the mono- or few-layers version of black phosphorus, phosphorene, were introduced, specially its outstanding hole mobility, which makes it a good candidate for transport calculations. The main focus of the chapter was to investigate how the electronic properties of phosphorene change after chemical functionalization, which has been used as a method to protect phosphorene against its degradation in environmental conditions. By means of spin-polarized density functional theory, the electronic and, in consequence, magnetic properties were discussed in terms of coverage and lattice functionalization. One of the key results discussed in this chapter was the introduction of magnetism in phosphorene through the formation of a dangling bond in the P_B atom as a consequence of the P_O-P_B bond breaking followed by the molecular adsorption. Different parameters of the electronic band structure, such as band gap energy and in-gap degeneration, as well as the magnetic ground state of the system can be modulated with the arrangement, coverage and type of the functionalized molecules. Inspired by the induced magnetism in the system, cysteine molecules were employed to functionalize phosphorene to investigate any signatures of chiral discrimination. A correlation between them was not found, but the employment of a mixture of enantiomers could lead to a diversification of the magnetic ground state. As a final result of this chapter, it was suggested that this kind of molecular systems can be engineered to design bipolar magnetic semiconductors, which take advantage of the spin-up and spin-down in-gap states around the Fermi level, leading to the development of spintronic devices.

The second part was centered in the tuning of electronic and thermal properties by mechanical strain in grain boundary systems. In Chapter 4 two types of

phosphorene grain boundaries were studied that included the 5|7 and 4|8 defects. The evolution of the electronic, thermal and thermoelectric properties of the GBs with the applied uniaxial strain was computed by combining a density functional based tight binding approach with the atomistic Green's function method. The change in the IP and OP bond distances, as well as the phosphorene orientation, were correlated with the transport properties through the GB system, showing also that the tuning degree of these properties depend on the linear defects of the GB. Despite the fact that the linear 5|7 defects and applied strain in GB1 cause an enhancement of the electronic transmission and a suppression of the thermal conductance with respect to pristine phosphorene along the zigzag direction larger than the changes generated in GB2 with respect to the pristine phosphorene along the armchair direction, the thermoelectric properties and figure of Merit of GB2 are greater than in GB1. The discussed results of that chapter are of great interest for the development of phosphorene GB based systems towards potential thermoelectric devices.

The topic of the third part goes around studying the electronic, thermal and thermoelectric properties of CNT peapods, a particular type of hybrid nanomaterials. Similarly as with phosphorene GB, in Chapter 5, the transport properties of the CNT peapods were carried out with the density functional based tight binding method and the atomistic Green's functions. In this study, the main system of interest was the C_{60}@CNT(8,8) since it has the largest interaction between the C_{60} molecules and the CNT as a consequence of the small distance between these two components, but also the properties of C_{60}@CNT(9,9) and C_{60}@CNT(10,10) were also computed to serve as a comparison. One of the main factors that is the result of the strong C_{60}-CNT(8,8) interaction and is responsible of several effects in the transport properties of this system is the development of periodic buckling along the CNT wall. With the assistance of some hypothetical systems, such as the distorted CNT or the peapod with a single C_{60} molecule, a deeper understanding was obtained of either the local structural deformation or the C_{60} presence was the key element that modified the transport properties in certain direction. The CNT peapod showed enhancement and suppression at certain energy windows in the electronic transmission as well as suppression of phonon transmission at low and high frequencies, which led to produce a larger thermoelectric figure of merit by a factor of 2.2 with respect to the pristine CNT(8,8). This hybrid system displayed the dominant effect of both C_{60}-C_{60} and C_{60}-CNT interactions, which proved to be an additional path to influence the thermoelectric transport properties of CNT and other 1D-based systems.

Even though plenty of progress has been made through the tuning of transport

properties in low dimensional systems from different perspectives, still several questions remain open to be answered. Regarding the functionalized phosphorene systems, computation of their transport properties should be the next step, since the studied parameters can modify the electronic band structure, hence, it is expected to find a correlation with the electronic conductivity. Furthermore, calculation of the phonon band structure and thermal transmission can be of interest to complement the study in dependence to the functionalization, and later determine the best parameters to improve the thermoelectric figure of merit. An additional degree of freedom to analyze in this regard is the anisotropy of phosphorene, which then compete as additional parameter in the transport properties calculation. The computation of other factors, such as dipole moment or functionalization group of the molecules linked to the phosphorene can provide additional information for tuning further the transport properties of phosphorene. Molecular dynamics studies can be carried to test the optimal orientation of the molecule after functionalization, study the limits of the functionalization coverage without reaching its degradation and prove if the functionalized systems can work as self-assembled monolayers. Phosphorene functionalized with chiral molecules could be tested as a spin valve by taking advantage of its property as a bipolar magnetic semiconductor and the chiral induced spin selectivity effect (See Figure A.2 in Appendix A.2). At difference with other conventional spin valves that works with an external magnetic field, this one changes the spin orientation of the free layer with an external voltage, meanwhile the chirality of the functionalized molecule dictates acts as the fix layer. Hence, the change between high resistance and low resistance states may work with a less complex system.

Regarding Chapter 4, additional calculations considering different type of GB and a mixture between GB and other structural defects such as monovacancies could lead to interesting results. Also, employing more than one GB type in the transmission device could be considered, taking into account phosphorene can be polycrystal with more than two nucleation points. Computation of few-layer phosphorene GB could complement this study, whether all the layers have the same or different GB, allowing to understand if this could play a role in the transport properties. Implementing machine learning algorithms to predict the transport properties of phosphorene and other 2D materials can be useful to optimize computational time towards the engineering do thermoelectric devices.

For last, in the topic of CNT peapods as hybrid systems, computing the thermoelectric properties of CNT peapods but using larger empty or endohedral fullerenes could proof that the presented effects can be presented in also in larger diameter CNT's. Other alternative could be employing C_{60} fullerenes with

larger diameter CNTs and applying radial strain in the system to compress the nanotube, forcing the system the system to interact with the hosted fullerenes and tune their transport properties. This system can be proposed as device that works under a similar principle as a piezoelectric material, possibly mixed the CNT peapods as a part of a composite, that tunes the thermoelectric properties when the material is under external strain. From other perspective, the study of double or multi wall CNT peapod is missing in this work, which is of interest to know if this effect is preserved beyond single wall CNT peapods. Last, extending this study to non-carbon based structure is of interest, either employing hollow 1D materials like BN- or P-based nanotubes, or 0D materials like nanoparticles.

Appendices

Appendix A

Supplementary information to phosphorene functionalization

This Appendix contains supplementary information to the Chapter 3.

A.1 Spin resolved density of states of 1-OH system

The orbital resolved spin density of states was computed for the neighboring atoms of the functionalization site, including the oxygen atom, as depicted in Figure A.1. The P_B, the oxygen atom, the second (P_2) and fourth neighbors (P_4) of P_B have a larg contribution of p_z states, while the P_O and the first neighbors (P_1) of P_B predominate the p_y states. The resulting local magnetization corresponds to the resolved spin DOS, form which the largest magnetic moments are located in P_B, P_O, oxygen and P_2, with 0.076 μ_B/cell in P_B, 0.046 μ_B/cell in P_O, 0.03 μ_B/cell in oxygen and 0.013 μ_B/cell in the atoms P_2.

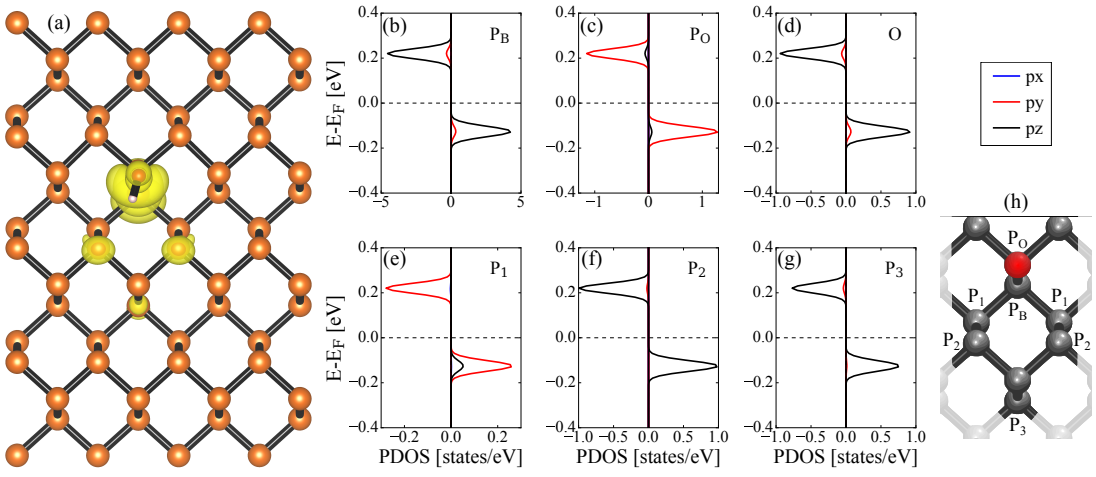

Fig. A.1 (a) Spin density difference of 1-OH system from top perspective. Spin resolved density of states of (b) P_B, (c) P_O, (d) O, (e) P_1, (f) P_2 and (g) P_3, where the orbitals p_x (blue), p_y (red) and p_z (black) are resolved. (h) schematic of atoms around the functionalization site that contribute in the spin density with their corresponding labels.

A.2 Spin valve model

A spin valve consists in a device made of two or more conducting magnetic materials, which electrical resistance can be tuned between two valued in dependence of the relative alignment of the magnetization in the layers. A spin valve has a fixed layer, where the spin orientation of the electrons does not change, and a free layer, where the spin orientation of the electrons can be manipulated, usually with an external magnetic field. Phosphorene functionalized with cysteine can be proposed as a spin valve device by using the CISS effect and the bipolar magnetic semiconductor, where the chirality of the functionalized cysteine defines the fixed layer and the bipolar magnetic semiconductor effect from the surface plays the role of the free layer. There are two main advantage of this model over the conventional spin valves: the system is simplified to molecules and phosphorene, instead of using two magnetic layers, and it does not depends on an external magnetic field.

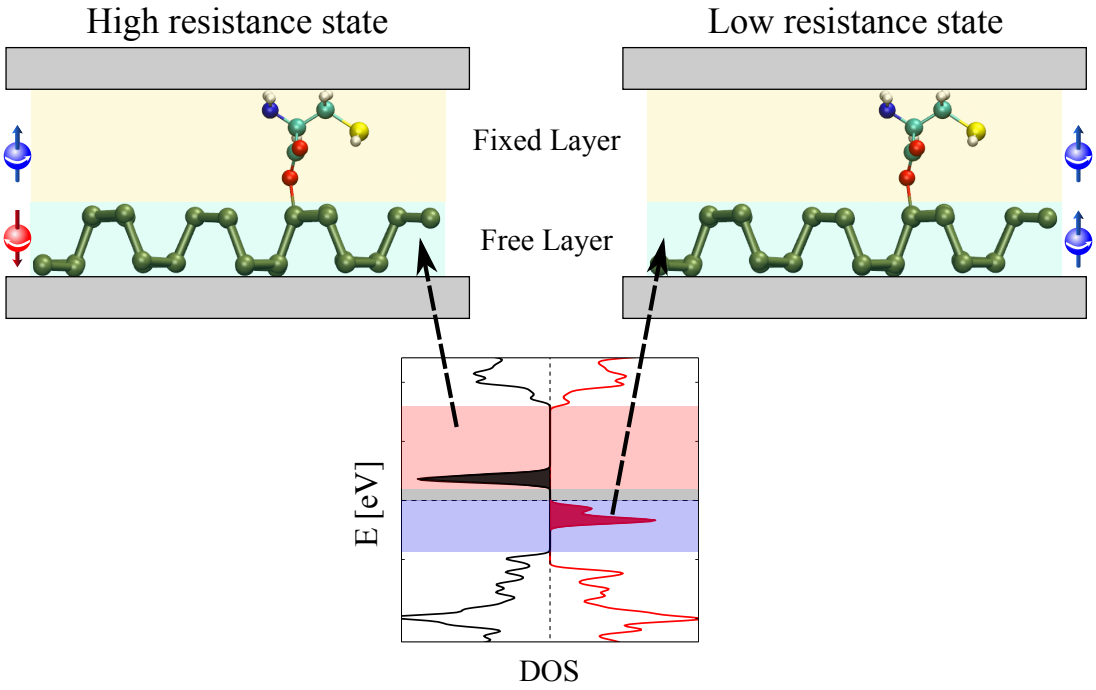

Fig. A.2 Schematic of the cysteine functionalized system as spin valve. The chirality of the cysteine molecule acts as a fixed layer, while the phosphorene, as a bipolar magnetic semiconductor, functions as a free layer by changing the electronic spin orientation with an external electric voltage. By applying a positive or negative voltage along the phosphorene layer, the spin valve changes between a high resistance state (left side) and a low resistance state (right side).

Appendix B

Supplementary information to phosphorene grain boundaries

This Appendix contains supplementary information to the Chapter 4.

B.1 Projected Phonon Density of States in GB1

The projected phonon density of states (PDOS) has been calculated by using Green's function formalism as follow [78]:

$$\mathrm{PDOS}(\omega) = \frac{\mathrm{i}(\mathrm{G}^{\mathrm{r}} - \mathrm{G}^{\mathrm{a}})\omega}{\pi \mathrm{B}_{\mathrm{Fx}}}, \tag{B.1}$$

where $G^{r/a}$ is the retarded/advanced Green's function of the device region with bond length B_{Fx}. This analysis was focused on the frequency range 260-320cm^{-}1 of τ_{ph} for GB1 system to obtain information about the origin of the new transmission resonances that emerge after applying strain (see Figure B.1).

Figures B.1(a-c) show the real-space PDOS of GB1 system under three different cases of strain $s = 0\%$, 3.86%, and 7.82%. The contribution to the vibrational modes is represented with a color code, where *darkblue* and *red* correspond to the atoms with lowest and highest contribution. The values of PDOS are normalized to the highest value between the three devices at different strain levels. The associated frequency-space PDOS is plotted at different strain levels, see Figures B.1(d-f). The result in Figure B.1(a) displays that all atoms in the device region of GB1 system without strain are not contributing to vibrational modes within $\omega \in [260 - 320]$ cm^{-1}, causing the presence of a phonon band gap (see Figure B.1(d)).

The phonon band gap decreased when applying strain due to new vibrational modes originated by the atoms in the surroundings of the GB region (see Figures B.1(b,e)), and it disappears when the strain is above 7.8% (see Figure B.1(f)). The lowest contribution to the PDOS in this frequency region are attributed to the GB atoms, while the rest of the atoms of the device region are the main vibrational source that fill the phonon band gap. Therefore, vibrations associated

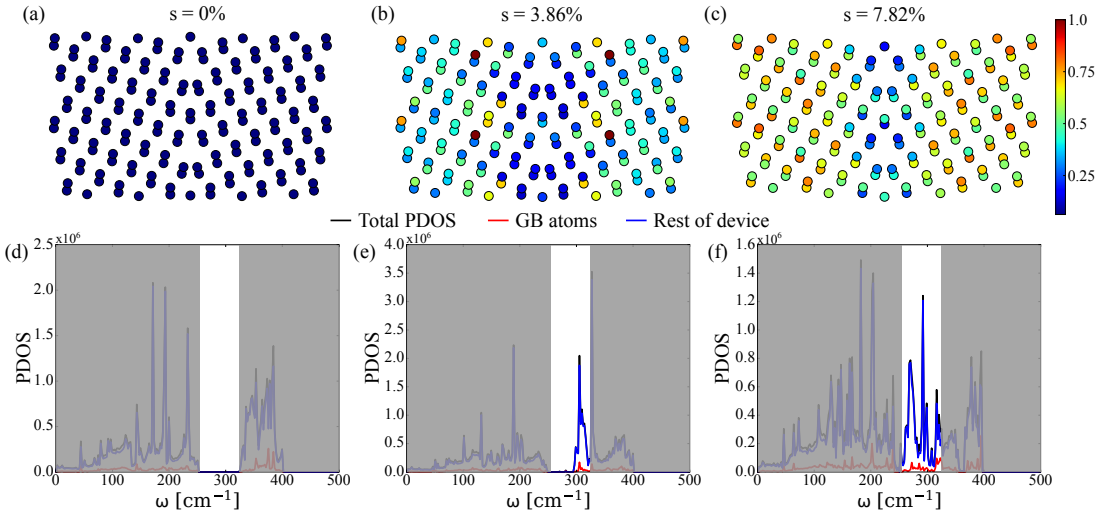

Fig. B.1 Real-space projection of the phonon density of states (PDOS) of the device region in GB1 system with (a) 0%, (b) 3.86% and (c) 7.82% applied strain. The PDOS values are normalized to the highest value between the three systems and the colorbar (right side) scales the contribution of each atom, where *darkblue* means zero contribution and *red* is the highest contribution. The PDOS as a function of the frequency corresponding to the systems analyzed in panels (a-c) are plotted in the panels (d-f). We show the total PDOS (black) together with the contribution from the atoms in the grain boundary (red) and the in the rest of the device (blue). We have added the blocks in grey to highlight the frequency range for this analysis, 260-320 cm^{-1}.

to GB atoms in this frequency range are less susceptible to structural changes compared to the other atoms.

B.2 Thermoelectric transport properties of GB2

The thermoelectric parameters analysis of GB2 is presented in Figure B.2, at 300K and 600K. At difference to GB1, the results of κ_{el} (see Figure B.2 (a, b)) are considerably inferior in the negative side of the μ, but not for high strain value ($s = 17.35\%$), where then approaches similar values as the other systems in GB1. On the other hand, for positive μ, the trend is different, where it decreases in proportion to the applied strain. Notably, regions that are distant from the neutral carrier concentration point ($\mu = 0$) have higher κ_{el} than as it was seen in the GB1 systems, as a consequence of the opening of the bandgap in the GB2 system. with the raise of temperature, κ_{el} also increases, but in smaller proportion compared with GB1 systems, which can be an advantage for their use as thermoelectric systems at higher temperatures, since the not-so large values of κ_{el} will then do not decrease so much the ZT. Moving to S (see Figure B.2 (c, d)), and in contrast to the GB1 system, all the GB2 systems do not have a symmetric profile at low neither at higher temperature. The system with $s =$

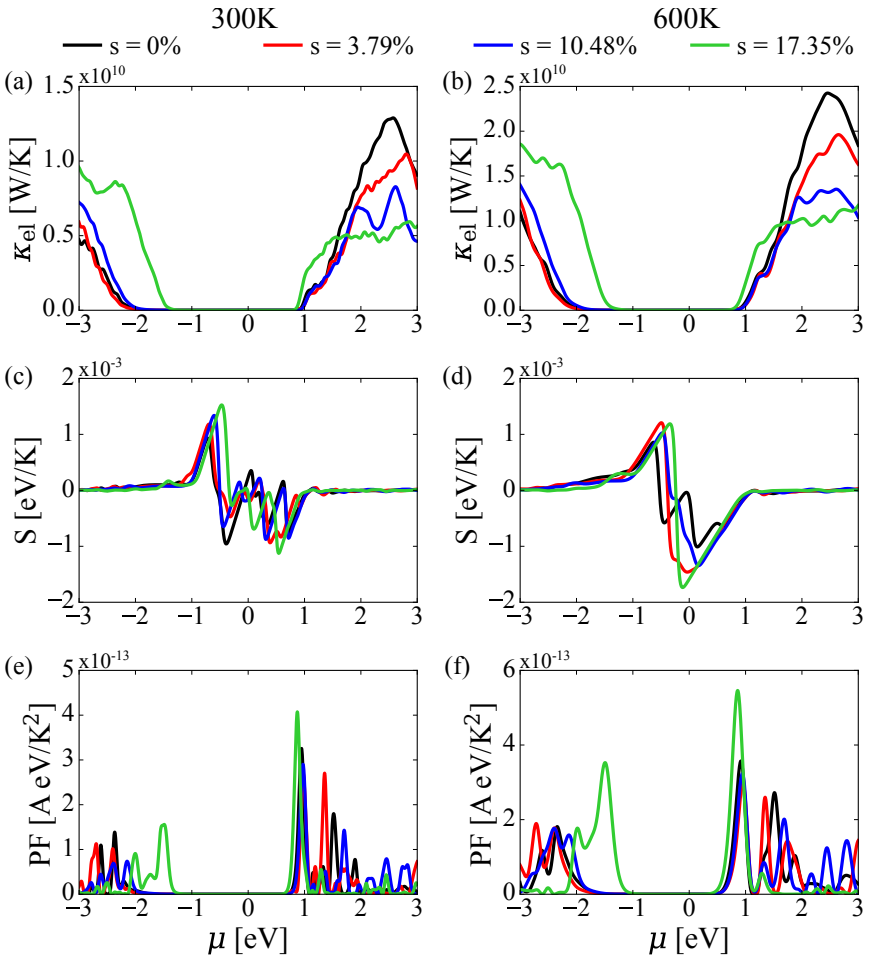

Fig. B.2 Thermoelectric transport properties of GB2 at 300 K (left side) and 600 K (right side) at different values of strain. The variation in the (a, b) electronic contribution to the thermal conductance (κ_{el}), (c, d) the Seebeck coefficient (S), and (e, f) the power factor (PF) as a function of the chemical potential μ is displayed.

17.35% presents the highest peaks in both sides of the plot with values above |1 eV/K|. At 600 K, the S increases in all the systems and the largest values are displaced towards the neutral carrier concentration point, favoring their potential usage for thermoelectric devices. At last, the PF for these systems (see Figures B.2 (e, f)) are very low in the negative side of the μ, meaning that p-type carriers can not be useful for thermoelectric devices. On the other hand, the opposite effect can be seen in the positive side of the plotm which shows good results for the GB2 systems, specially for the GB2 with $s = 17.37\%$, which reaches 4.1 AeV/K^2 at 0.95 eV. Similar results are obtained at 600 K, where an increase in the PF for all the systems is notable. The decrease of κ_{el} and enhancement of PF in function of the strain can open the possibility for strained GB2 devices to be employed for thermoelectric systems.

Appendix C

Supplementary information to CNT peapods

This Appendix contains supplementary information to the Chapter 5.

C.1 Geometry optimization of CNT peapods with larger CNT diameter

The atomistic representation after geometry optimization of CNT peapods with CNT(8,8), CNT(9,9) and CNT(10,10) are displayed in Figure C.1. Each system is represented along the periodic direction and the transversal plane. The CNT diameters of the bottleneck and around the center of the C_{60} molecule are shown. Here, one can notice that large diameter CNT systems present lower deformation around the fullerenes.

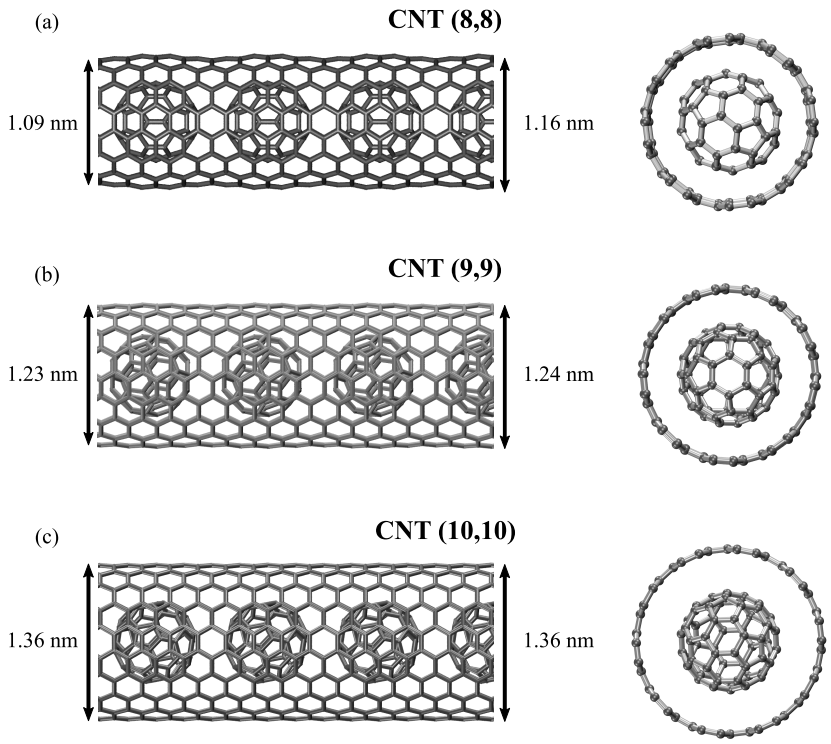

Fig. C.1 Atomistic representation of (a) C_{60}@CNT(8,8), (b) C_{60}@CNT(9,9), and (c) C_{60}@CNT(10,10) after geometry optimization.

C.2 Additional analysis of electron transport properties

Figures C.2 and C.3 display the electronic transmission of artificial cases of CNT peapods to understand the influence in the electronic transmission of the fullerene-CNT and fullerene-fullerene interactions.

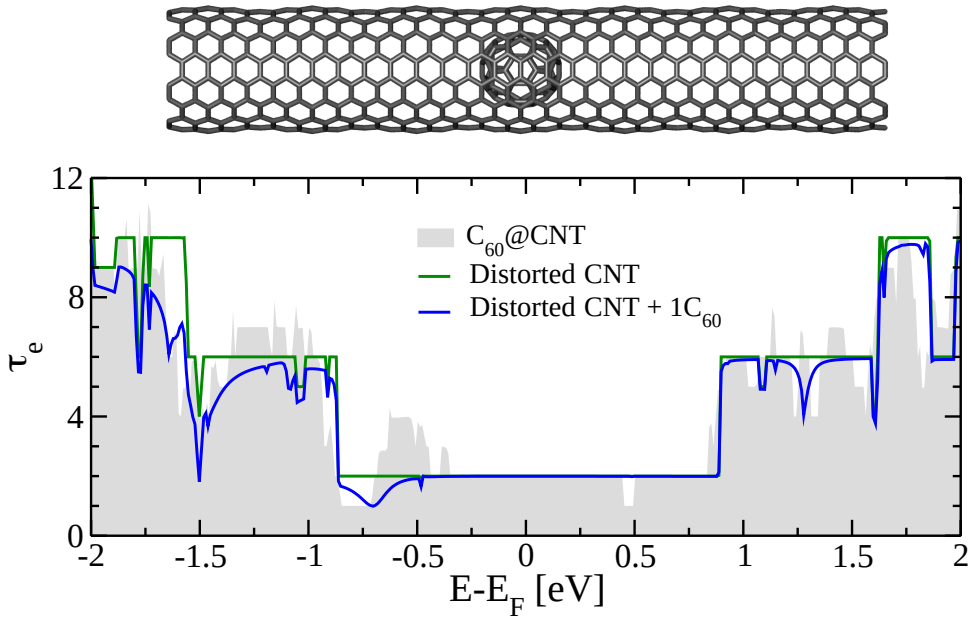

Fig. C.2 Electronic transmission of C_{60}@CNT(8,8) (gray), distorted CNT (green) and an artificial system (blue).

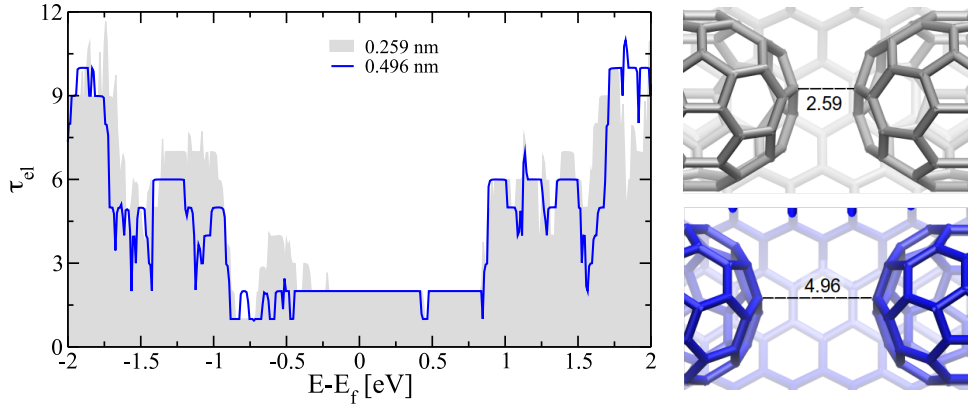

Fig. C.3 Electronic transmission of C_{60}@CNT(8,8) with 0.259 nm (gray) and 0.496 nm (blue) distance between C_{60} molecules.

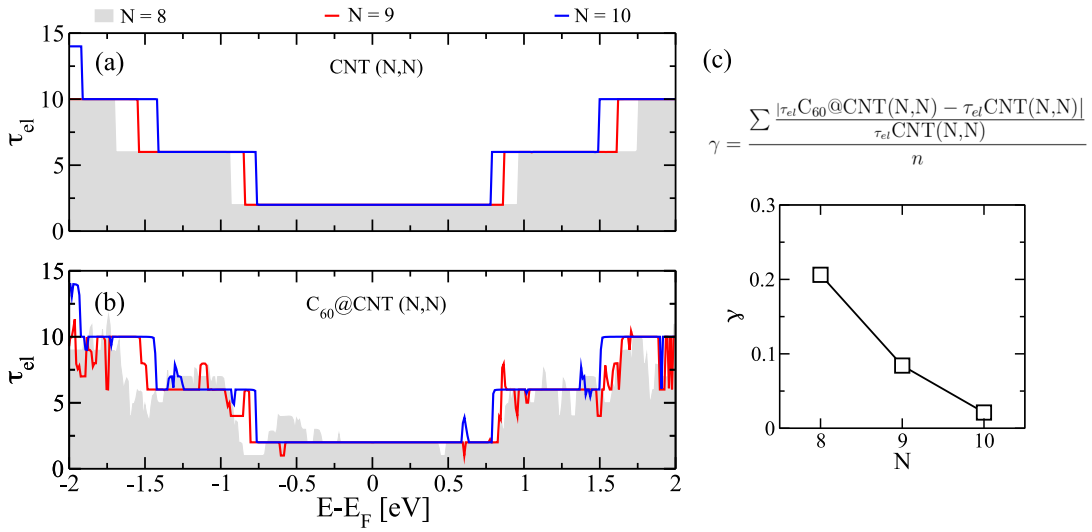

Fig. C.4 Electronic transmission of (a) pristine CNT and (b) C_{60}@CNT for CNT with different diameters. Pristine CNT(N,N) with N = 8 (gray), N = 9 (red) and N = 10 (blue) displays an uniform step-wise electronic transmission.

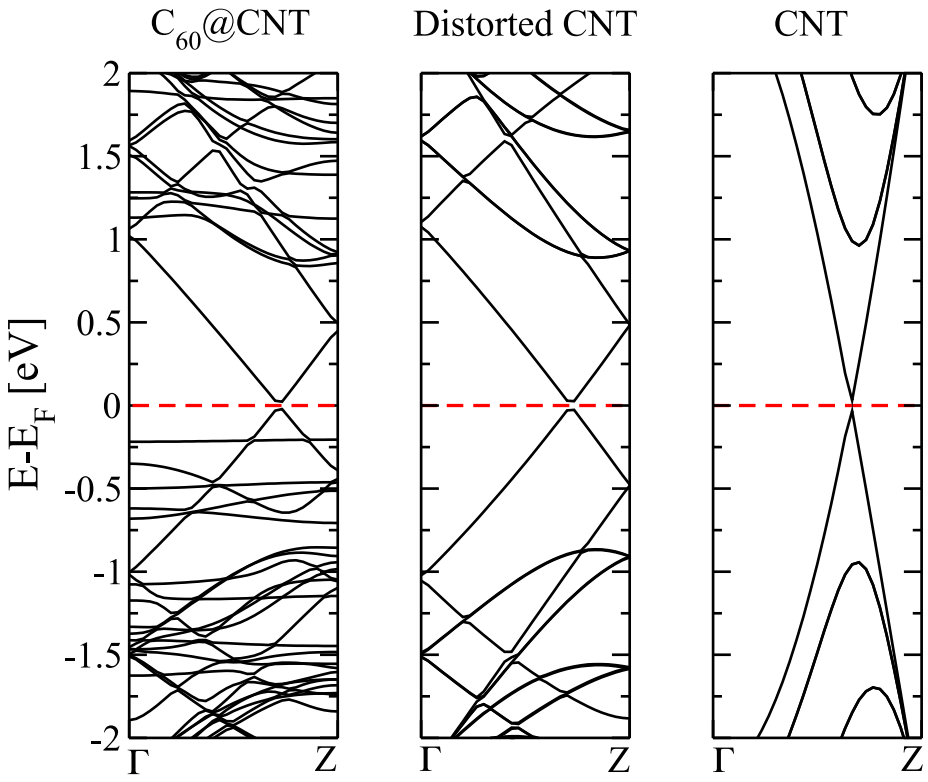

Fig. C.5 Electronic band structure of C_{60}@CNT(8,8), distorted CNT and CNT systems.

C.3 Phonon band structure of different CNT structures

Figure C.6 displays the phonon band structure in the high frequency modes of CNT, distorted CNT and C_{60}@CNT(8,8). It is notorious the emergence of the band gap, denoted with the red area in the plot, once the distortion of the CNT is presented.

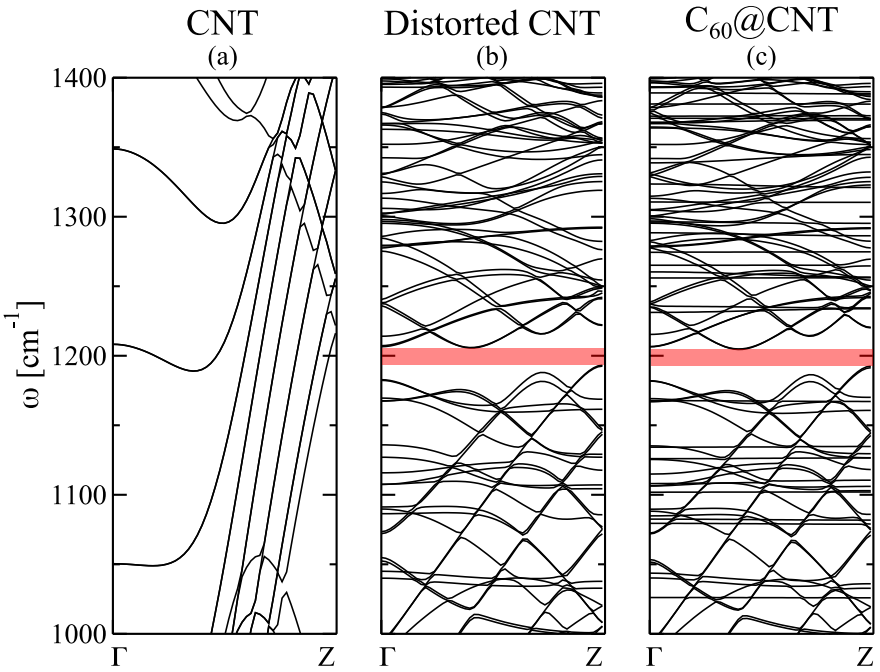

Fig. C.6 Phonon dispersion at high frequency-modes of (a) pristine CNT, (b) distorted CNT and (c) C_{60}@CNT(8,8).

C.4 Additional analysis of thermoelectric performance

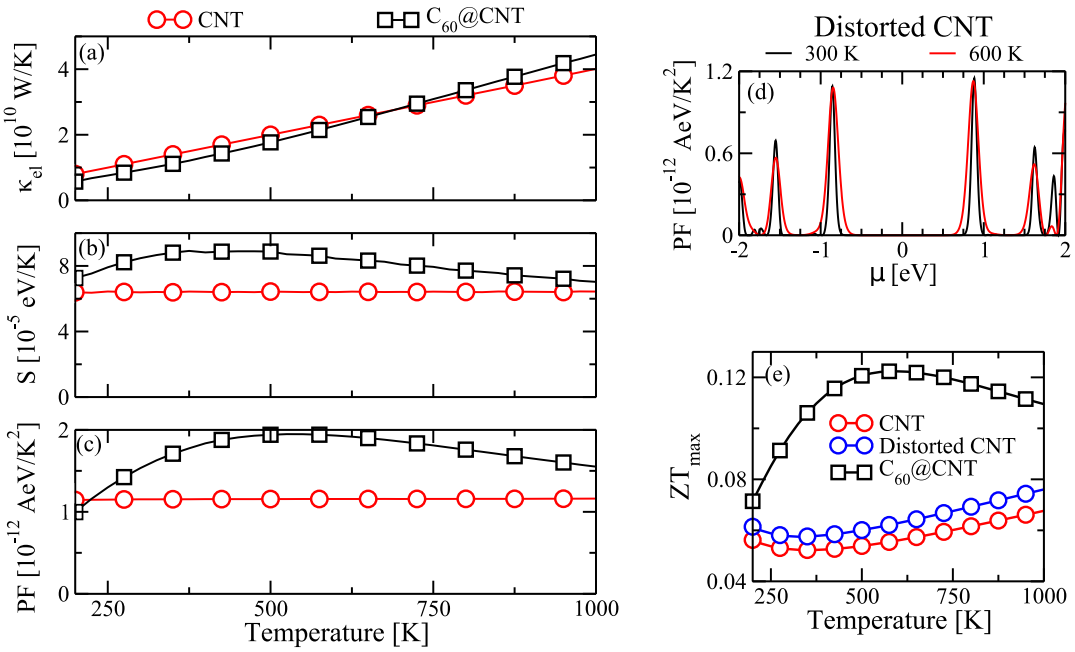

Fig. C.7 (a) Electronic contribution to the thermal conductance (κ_{el}), (b) Seebeck coefficient S and (c) power factor (PF) at ideal μ as a function of the temperature for CNT(8,8) (red curve) and C_{60}@CNT(8,8) (black curve). κ_{el} do not show a notable difference between both systems, but regarding S and PF, a notorious enhancement can be seen in the C_{60}@CNT(8,8), showing a better performance around 450 K and 575 K, respectively. (d) PF as a function of the chemical potential for distorted CNT at 300 K and 600 K. An slight asymmetric behavior w.r.t the charge neutrality point ($\mu = 0$ eV) is observed in the system. (e) Temperature dependence of the maximum value of ZT (ZT_{max}) for pristine CNT(8,8) (red circles), distorted CNT(8,8) (blue circles) and C_{60}@CNT(8,8) (black squares).

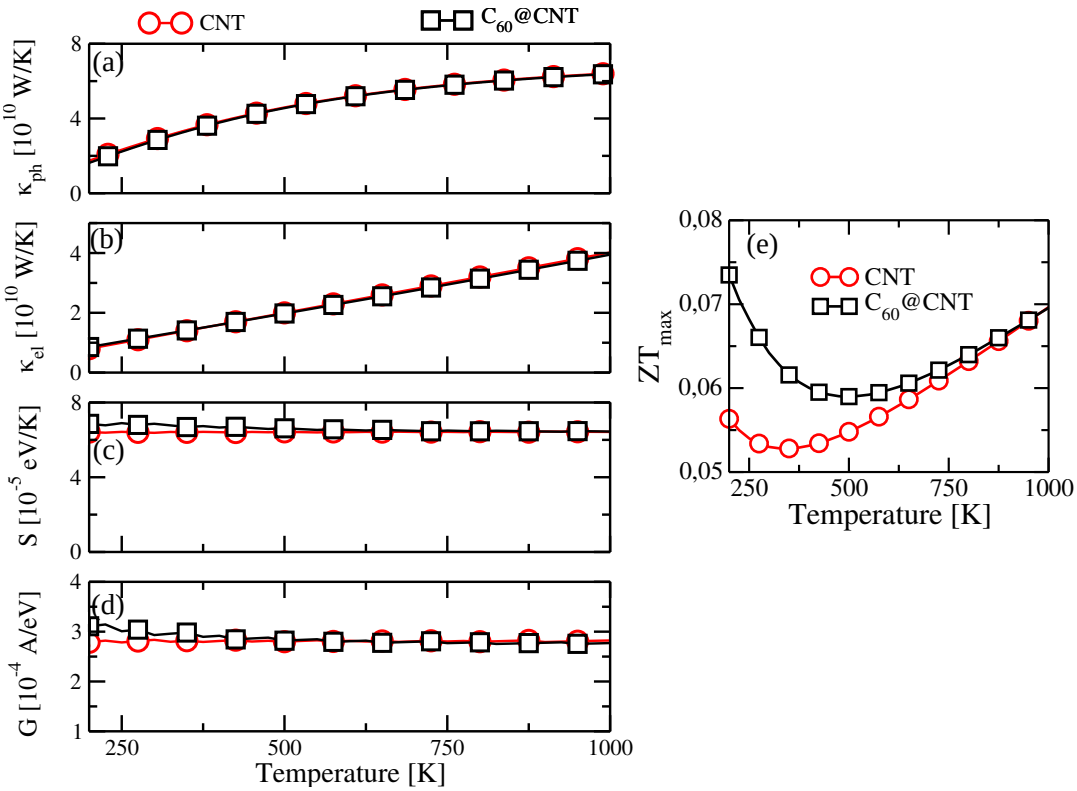

Fig. C.8 Thermoelectric transport properties of pristine CNT(9,9) (left side) and C_{60}@CNT(9,9) (right side) at 200 K (black line) and 600 K (red line). We show the variation in the (a,b) electronic contribution to the thermal conductance (k_{el}), (c,d) the Seebeck coefficient (S), and (e,f) the power factor (PF) as a function of the chemical potential μ.

REFERENCES

[1] TANIGUCHI, N. (1974). On the basic concept of nanotechnology. *Proceeding of the ICPE*.

[2] Feynman, R. P. (1960). *There is Plenty of Room at the Bottom*, volume 23, pages 22–36. Eng. Sci.

[3] Drexler, K. E. (1981). Molecular engineering: An approach to the development of general capabilities for molecular manipulation (molecular machinery/protein design/synthetic chemistry/computation/tissue characterization). *Proc. Natd Acad. Sci. USA*, 78:5275–5278. doi:https://doi.org/10.1073/pnas.78.9.5275.

[4] Abid, N., Khan, A. M., Shujait, S., Chaudhary, K., Ikram, M., Imran, M., Haider, J., Khan, M., Khan, Q., and Maqbool, M. (2022). Synthesis of nanomaterials using various top-down and bottom-up approaches, influencing factors, advantages, and disadvantages: A review. *Advances in Colloid and Interface Science*, 300:102597. doi:https://doi.org/10.1016/j.cis.2021.102597.

[5] Iqbal, P., Preece, J. A., and Mendes, P. M. (2012). *Nanotechnology: The "Top-Down" and "Bottom-Up" Approaches*. John Wiley and Sons, Ltd.

[6] Mag-isa, A. E., Kim, J.-H., Lee, H.-J., and Oh, C.-S. (2015). A systematic exfoliation technique for isolating large and pristine samples of 2d materials. *2D Materials*, 2(3):034017. doi:10.1088/2053-1583/2/3/034017.

[7] Zhang, X., Li, Y., Mu, W., Bai, W., Sun, X., Zhao, M., Zhang, Z., Shan, F., and Yang, Z. (2021). Advanced tape-exfoliated method for preparing large-area 2d monolayers: a review. *2D Materials*, 8(3):032002. doi:10.1088/2053-1583/ac016f.

[8] Pimpin, A. and Srituravanich, W. (2012). Reviews on micro- and nanolithography techniques and their applications. *Engineering Journal*, 16:37–55. doi:10.4186/ej.2012.16.1.37.

[9] Sharma, E., Rathi, R., Misharwal, J., Sinhmar, B., Kumari, S., Dalal, J., and Kumar, A. (2022). Evolution in lithography techniques: Microlithography to nanolithography. *Nanomaterials*, 12(16). doi:10.3390/nano12162754.

[10] Arya, S., Mahajan, P., Mahajan, S., Khosla, A., Datt, R., Gupta, V., Young, S.-J., and Oruganti, S. K. (2021). Review—influence of processing parameters to control morphology and optical properties of sol-gel synthesized zno nanoparticles. *ECS Journal of Solid State Science and Technology*, 10(2):023002. doi:10.1149/2162-8777/abe095.

[11] Navas, D., Fuentes, S., Castro-Alvarez, A., and Chavez-Angel, E. (2021). Review on sol-gel synthesis of perovskite and oxide nanomaterials. *Gels*, 7(4). doi:10.3390/gels7040275.

[12] Gudmundsson, J. T., Anders, A., and von Keudell, A. (2022). Foundations of physical vapor deposition with plasma assistance. *Plasma Sources Science and Technology*, 31(8):083001. doi:10.1088/1361-6595/ac7f53.

[13] Bhowmik, S. and Govind Rajan, A. (2022). Chemical vapor deposition of 2d materials: A review of modeling, simulation, and machine learning studies. *iScience*, 25(3):103832. doi:https://doi.org/10.1016/j.isci.2022.103832.

[14] Kumar, M. and Ando, Y. (2010). Chemical vapor deposition of carbon nanotubes: A review on growth mechanism and mass production. *Journal of Nanoscience and Nanotechnology*, 10:3739–3758. doi:10.1166/jnn.2010.2939.

[15] Liu, W., Karpov, E., Zhang, S., and Park, H. (2004). An introduction to computational nanomechanics and materials. *Computer Methods in Applied Mechanics and Engineering*, 193(17):1529–1578. doi:https://doi.org/10.1016/j.cma.2003.12.008, Multiple Scale Methods for Nanoscale Mechanics and Materials.

[16] Friesner, R. A. (2005). ab initio quantum chemistry: Methodology and applications. *Proceedings of the National Academy of Sciences*, 102(19):6648–6653. doi:10.1073/pnas.0408036102.

[17] Friesner, R. A. (2005). ab initio quantum chemistry: Methodology and applications. *Proceedings of the National Academy of Sciences*, 102(19):6648–6653. doi:10.1073/pnas.0408036102.

[18] Cui, Q. and Elstner, M. (2014). Density functional tight binding: values of semi-empirical methods in an ab initio era. *Phys. Chem. Chem. Phys.*, 16:14368–14377. doi:10.1039/C4CP00908H.

[19] Porezag, D., Frauenheim, T., Köhler, T., Seifert, G., and Kaschner, R. (1995). Construction of tight-binding-like potentials on the basis of density-functional theory: Application to carbon. *Phys. Rev. B*, 51:12947–12957. doi:10.1103/PhysRevB.51.12947.

[20] Seifert, G., Porezag, D., and Frauenheim, T. (1996). Calculations of molecules, clusters, and solids with a simplified lcao-dft-lda scheme. *International Journal of Quantum Chemistry*, 58(2):185–192. doi:https://doi.org/10.1002/(SICI)1097-461X(1996)58:2<185::AID-QUA7>3.0.CO;2-U.

[21] Kedharnath, A., Kapoor, R., and Sarkar, A. (2021). Classical molecular dynamics simulations of the deformation of metals under uniaxial monotonic loading: A review. *Computers and Structures*, 254:106614. doi:https://doi.org/10.1016/j.compstruc.2021.106614.

[22] Hernández, N. C. and Sanz, J. (2006). From periodic dft calculations to classical molecular dynamics simulations. *Computational Materials Science*, 35(3):183–186. doi:https://doi.org/10.1016/j.commatsci.2004.09.052, Proceedings of the 4th International Conference on the Theory of Atomic and Molecular Clusters (TAMC-IV).

[23] Farah, K., Müller-Plathe, F., and Böhm, M. C. (2012). Classical reactive molecular dynamics implementations: State of the art. *ChemPhysChem*, 13(5):1127–1151. doi:https://doi.org/10.1002/cphc.201100681.

[24] Hansson, T., Oostenbrink, C., and van Gunsteren, W. (2002). Molecular dynamics simulations. *Current Opinion in Structural Biology*, 12(2):190–196. doi:https://doi.org/10.1016/S0959-440X(02)00308-1.

[25] Monticelli, L. and Tieleman, D. P. (2013). *Force Fields for Classical Molecular Dynamics*, pages 197–213. Humana Press, Totowa, NJ.

[26] Tersoff, J. (1988). New empirical approach for the structure and energy of covalent systems. *Phys. Rev. B*, 37:6991–7000. doi:10.1103/PhysRevB.37.6991.

[27] Stuart, S. J., Tutein, A. B., and Harrison, J. A. (2000). A reactive potential for hydrocarbons with intermolecular interactions. *The Journal of Chemical Physics*, 112(14):6472–6486. doi:10.1063/1.481208.

[28] Daw, M. S., Foiles, S. M., and Baskes, M. I. (1993). The embedded-atom method: a review of theory and applications. *Materials Science Reports*, 9(7):251–310. doi:https://doi.org/10.1016/0920-2307(93)90001-U.

[29] Stillinger, F. H. and Weber, T. A. (1985). Computer simulation of local order in condensed phases of silicon. *Phys. Rev. B*, 31:5262–5271. doi:10.1103/PhysRevB.31.5262.

[30] Allen, A. E. A. and Tkatchenko, A. (2022). Machine learning of material properties: Predictive and interpretable multilinear models. *Science Advances*, 8(18):eabm7185. doi:10.1126/sciadv.abm7185.

[31] Liu, W., Wu, Y., Hong, Y., Zhang, Z., Yue, Y., and Zhang, J. (2022). Applications of machine learning in computational nanotechnology. *Nanotechnology*, 33(16):162501. doi:10.1088/1361-6528/ac46d7.

[32] Goodall, R. E. and Lee, A. A. (2020). Predicting materials properties without crystal structure: deep representation learning from stoichiometry. *Nature Communications*, 11. doi:10.1038/s41467-020-19964-7.

[33] Schmidt, J., Marques, M. R., Botti, S., and Marques, M. A. (2019). Recent advances and applications of machine learning in solid-state materials science. *npj Computational Materials*, 5. doi:10.1038/s41524-019-0221-0.

[34] Guo, J., Chen, Z., Liu, Z., Li, X., Xie, Z., Wang, Z., and Wang, Y. (2022). Neural network training method for materials science based on multi-source databases. *Scientific Reports*, 12. doi:10.1038/s41598-022-19426-8.

[35] Hong, Y., Hou, B., Jiang, H., and Zhang, J. (2020). Machine learning and artificial neural network accelerated computational discoveries in materials science. *WIREs Computational Molecular Science*, 10(3):e1450. doi:https://doi.org/10.1002/wcms.1450.

[36] Noack, M. M., Doerk, G. S., Li, R., Streit, J. K., Vaia, R. A., Yager, K. G., and Fukuto, M. (2020). Autonomous materials discovery driven by gaussian process regression with inhomogeneous measurement noise and anisotropic kernels. *Scientific Reports*, 10. doi:10.1038/s41598-020-74394-1.

[37] Bishnoi, S., Ravinder, R., Grover, H. S., Kodamana, H., and Krishnan, N. M. A. (2021). Scalable gaussian processes for predicting the optical, physical, thermal, and mechanical properties of inorganic glasses with large datasets. *Mater. Adv.*, 2:477–487. doi:10.1039/D0MA00764A.

[38] Wagner, N. and Rondinelli, J. M. (2016). Theory-guided machine learning in materials science. *Frontiers in Materials*, 3. doi:10.3389/fmats.2016.00028.

[39] Sim, S. and Wong, N. K. (2021). Nanotechnology and its use in imaging and drug delivery (review). *Biomedical Reports*, 14. doi:10.3892/br.2021.1418.

[40] Lee, J., Mahendra, S., and Alvarez, P. J. J. (2010). Nanomaterials in the construction industry: A review of their applications and environmental health and safety considerations. *ACS Nano*, 4(7):3580–3590. doi:10.1021/nn100866w, PMID: 20695513.

[41] Sanchez, F. and Sobolev, K. (2010). Nanotechnology in concrete – a review. *Construction and Building Materials*, 24(11):2060–2071. doi:https://doi.org/10.1016/j.conbuildmat.2010.03.014.

[42] Khin, M. M., Nair, A. S., Babu, V. J., Murugan, R., and Ramakrishna, S. (2012). A review on nanomaterials for environmental remediation. *Energy Environ. Sci.*, 5:8075–8109. doi:10.1039/C2EE21818F.

[43] Rojas, J. P., Singh, D., Inayat, S. B., Sevilla, G. A. T., Fahad, H. M., and Hussain, M. M. (2017). Review—micro and nano-engineering enabled new generation of thermoelectric generator devices and applications. *ECS Journal of Solid State Science and Technology*, 6(3):N3036. doi:10.1149/2.0081703jss.

[44] Sangwan, V. K. and Hersam, M. C. (2020). Neuromorphic nanoelectronic materials. *Nature Nanotechnology*, 15:517–528. doi:10.1038/s41565-020-0647-z.

[45] Moore, G. E. (2006). Cramming more components onto integrated circuits, reprinted from electronics, volume 38, number 8, april 19, 1965, pp.114 ff. *IEEE Solid-State Circuits Society Newsletter*, 11(3):33–35. doi:10.1109/N-SSC.2006.4785860.

[46] Shalf, J. (2020). The future of computing beyond moore's law. *Philosophical Transactions of the Royal Society A: Mathematical, Physical and Engineering Sciences*, 378(2166):20190061. doi:10.1098/rsta.2019.0061.

[47] Nomura, M., Anufriev, R., Zhang, Z., Maire, J., Guo, Y., Yanagisawa, R., and Volz, S. (2022). Review of thermal transport in phononic crystals. *Materials Today Physics*, 22:100613. doi:https://doi.org/10.1016/j.mtphys.2022.100613.

[48] Tritt, T. (2002). Thermoelectric materials: Principles, structure, properties, and applications. In Buschow, K. J., Cahn, R. W., Flemings, M. C., Ilschner, B., Kramer, E. J., Mahajan, S., and Veyssière, P., editors, *Encyclopedia of Materials: Science and Technology*, pages 1–11. Elsevier, Oxford.

[49] Terasaki, I. (2016). Thermal conductivity and thermoelectric power of semiconductors. In *Reference Module in Materials Science and Materials Engineering*. Elsevier.

[50] NASA (2020). Power source of perseverance rover. https://mars.nasa.gov/mars2020/spacecraft/rover/electrical-power/. Accessed: 14.12.2022.

[51] Hicks, L. D., Harman, T. C., Sun, X., and Dresselhaus, M. S. (1996). Experimental study of the effect of quantum-well structures on the thermoelectric figure of merit. *Phys. Rev. B*, 53:R10493–R10496. doi:10.1103/PhysRevB.53.R10493.

[52] Dresselhaus, M. S., Dresselhaus, G., Sun, X., Zhang, Z., Cronin, S. B., and Koga, T. (1999). Low-dimensional thermoelectric materials. In *Phys. Solid State*, volume 41, pages 679–682.

[53] David S., S. and Janice A., S. (2009). *What is Density Functional Theory?*, chapter 1, pages 1–33. John Wiley and Sons, Ltd.

[54] Kohn, W., Becke, A. D., and Parr, R. G. (1996). Density functional theory of electronic structure. *The Journal of Physical Chemistry*, 100(31):12974–12980. doi:10.1021/jp960669l.

[55] Levine, I. (2014). *Quantum Chemistry*. Pearson advanced chemistry series. Pearson.

[56] Peng, D. and Nakashima, P. N. H. (2021). Measuring density functional parameters from electron diffraction patterns. *Phys. Rev. Lett.*, 126:176402. doi:10.1103/PhysRevLett.126.176402.

[57] Born, M. and Oppenheimer, R. (1927). Zur quantentheorie der molekeln. *Annalen der Physik*, 389(20):457–484. doi:https://doi.org/10.1002/andp.19273892002.

[58] Martin, R. M. (2004). *Density functional theory: foundations*, page 119–134. Cambridge University Press.

[59] Dirac, P. A. M. (1930). Note on exchange phenomena in the thomas atom. *Mathematical Proceedings of the Cambridge Philosophical Society*, 26(3):376–385. doi:10.1017/S0305004100016108.

[60] Hohenberg, P. and Kohn, W. (1964). Inhomogeneous electron gas. *Phys. Rev.*, 136:B864–B871. doi:10.1103/PhysRev.136.B864.

[61] Kohn, W. and Sham, L. J. (1965). Self-consistent equations including exchange and correlation effects. *Phys. Rev.*, 140:A1133–A1138. doi:10.1103/PhysRev.140.A1133.

[62] Hofmann, M. and Schaefer, H. F. (2003). Computational chemistry. In Meyers, R. A., editor, *Encyclopedia of Physical Science and Technology (Third Edition)*, pages 487–506. Academic Press, New York, third edition edition.

[63] Perdew, J. P., Burke, K., and Ernzerhof, M. (1996). Generalized gradient approximation made simple. *Phys. Rev. Lett.*, 77:3865–3868. doi:10.1103/PhysRevLett.77.3865.

[64] Finley, J. P. (2004). Using the local density approximation and the lyp, blyp and b3lyp functionals within reference-state one-particle density-matrix theory. *Molecular Physics*, 102(7):627–639. doi:10.1080/00268970410001687452.

[65] Richard, D., Muñoz, E. L., Rentería, M., Errico, L. A., Svane, A., and Christensen, N. E. (2013). *Abinitio* lsda and lsda + U study of pure and cd-doped cubic lanthanide sesquioxides. *Phys. Rev. B*, 88:165206. doi:10.1103/PhysRevB.88.165206.

[66] Koskinen, P. and Mäkinen, V. (2009). Density-functional tight-binding for beginners. *Computational Materials Science*, 47(1):237–253. doi:https://doi.org/10.1016/j.commatsci.2009.07.013.

[67] Spiegelman, F., Tarrat, N., Cuny, J., Dontot, L., Posenitskiy, E., Martí, C., Simon, A., and Rapacioli, M. (2020). Density-functional tight-binding: basic concepts and applications to molecules and clusters. *Advances in Physics: X*, 5(1):1710252. doi:10.1080/23746149.2019.1710252, PMID: 33154977.

[68] Atkins, P. and Friedman, R. (2011). *Molecular Quantum Mechanics*. OUP Oxford.

[69] Kittel, C. (2004). *Introduction to Solid State Physics*. Wiley.

[70] Elstner, M., Porezag, D., Jungnickel, G., Elsner, J., Haugk, M., Frauenheim, T., Suhai, S., and Seifert, G. (1998). Self-consistent-charge density-functional tight-binding method for simulations of complex materials properties. *Phys. Rev. B*, 58:7260–7268. doi:10.1103/PhysRevB.58.7260.

[71] Michael Gaus, Q. C. and Elstner, M. (2012). DFTB3: Extension of the self-consistent-charge density- functional tight-binding method (SCC-DFTB). *J. Chem. Theory Comput.*, 7(4):931–948. doi:10.1021/ct100684s.

[72] Luschtinetz, R., Oliveira, A. F., Frenzel, J., Joswig, J.-O., Seifert, G., and Duarte, H. A. (2008). Adsorption of phosphonic and ethylphosphonic acid on aluminum oxide surfaces. *Surf. Sci.*, 602(7):1347–1359. doi:https://doi.org/10.1016/j.susc.2008.01.035.

[73] Gaus, M., Goez, A., and Elstner, M. (2013). Parametrization and benchmark of dftb3 for organic molecules. *Journal of Chemical Theory and Computation*, 9(1):338–354. doi:10.1021/ct300849w, PMID: 26589037.

[74] Rauls, E., Elsner, J., Gutierrez, R., and Frauenheim, T. (1999). Stoichiometric and non-stoichiometric (1010) and (1120) surfaces in 2h–sic: a theoretical study. *Solid State Communications*, 111(8):459–464. doi:https://doi.org/10.1016/S0038-1098(99)00137-4.

[75] Datta, S. (2005). *Quantum Transport: Atom to Transistor*. Cambridge University Press.

[76] Sancho, M. P. L., Sancho, J. M. L., Sancho, J. M. L., and Rubio, J. (1985). Highly convergent schemes for the calculation of bulk and surface green functions. *Journal of Physics F: Metal Physics*, 15(4):851. doi:10.1088/0305-4608/15/4/009.

[77] Mingo, N. and Yang, L. (2003). Phonon transport in nanowires coated with an amorphous material: An atomistic green's function approach. *Phys. Rev. B*, 68:245406. doi:10.1103/PhysRevB.68.245406.

[78] Zhang, W., Fisher, T. S., and Mingo, N. (2007). The atomistic green's function method: An efficient simulation approach for nanoscale phonon transport. *Numerical Heat Transfer, Part B: Fundamentals*, 51(4):333–349. doi:10.1080/10407790601144755.

[79] Novoselov, K. S., Geim, A. K., Morozov, S. V., Jiang, D., Zhang, Y., Dubonos, S. V., Grigorieva, I. V., and Firsov, A. A. (2004). Electric field effect in atomically thin carbon films. *Science*, 306(5696):666–669. doi:10.1126/science.1102896.

[80] Briggs, N., Subramanian, S., Lin, Z., Li, X., Zhang, X., Zhang, K., Xiao, K., Geohegan, D., Wallace, R., Chen, L.-Q., Terrones, M., Ebrahimi, A., Das, S., Redwing, J., Hinkle, C., Momeni, K., van Duin, A., Crespi, V., Kar, S., and Robinson, J. A. (2019). A roadmap for electronic grade 2d materials. *2d Mater.*, 6(2):022001. doi:10.1088/2053-1583/aaf836.

[81] Xiong, Z., Zhong, L., Wang, H., and Li, X. (2021). Structural defects, mechanical behaviors and properties of two-dimensional materials. *Materials*, 14:1–43. doi:10.3390/ma14051192.

[82] Ares, P. and Novoselov, K. S. (2022). Recent advances in graphene and other 2d materials. *NMS*, 4(1):3–9.

doi:https://doi.org/10.1016/j.nanoms.2021.05.002, Special issue on Graphene and 2D Alternative Materials.

[83] Xu, M., Liang, T., Shi, M., and Chen, H. (2013). Graphene-like two-dimensional materials. *Chem. Rev.*, 113:3766–3798. doi:10.1021/cr300263a.

[84] Mas-Ballesté, R., Gómez-Navarro, C., Gómez-Herrero, J., and Zamora, F. (2011). 2d materials: to graphene and beyond. *Nanoscale*, 3:20–30. doi:10.1039/C0NR00323A.

[85] Fiori, G., Bonaccorso, F., Iannaccone, G., Palacios, T., Neumaier, D., Seabaugh, A., Banerjee, S. K., and Colombo, L. (2014). Electronics based on two-dimensional materials. *Nature Nanotechnology*, 9:768–779. doi:10.1038/nnano.2014.207.

[86] Li, D., Gong, Y., Chen, Y., Lin, J., Khan, Q., Zhang, Y., Li, Y., Zhang, H., and Xie, H. (2020). Recent progress of two-dimensional thermoelectric materials. *Nano-Micro Letters*, 12. doi:10.1007/s40820-020-0374-x.

[87] Hu, G. and Xiang, B. (2020). Recent advances in two-dimensional spintronics. *Nanoscale Research Letters*, 15. doi:10.1186/s11671-020-03458-y.

[88] Ahn, E. C. (2020). 2d materials for spintronic devices. *npj 2D Materials and Applications*, 4. doi:10.1038/s41699-020-0152-0.

[89] Liu, H., Neal, A. T., Zhu, Z., Luo, Z., Xu, X., Tománek, D., and Ye, P. D. (2014). Phosphorene: An unexplored 2d semiconductor with a high hole mobility. *ACS Nano*, 8:4033–4041. doi:10.1021/nn501226z.

[90] Li, L., Yu, Y., Ye, G. J., Ge, Q., Ou, X., Wu, H., Feng, D., Chen, X. H., and Zhang, Y. (2014). Black phosphorus field-effect transistors. *Nature Nanotechnology*, 9:372–377. doi:10.1038/nnano.2014.35.

[91] Brent, J. R., Savjani, N., Lewis, E. A., Haigh, S. J., Lewis, D. J., and O'Brien, P. (2014). Production of few-layer phosphorene by liquid exfoliation of black phosphorus. *Chem. Commun.*, 50:13338–13341. doi:10.1039/C4CC05752J.

[92] Sorkin, V., Cai, Y., Ong, Z., Zhang, G., and Zhang, Y. W. (2017). Recent advances in the study of phosphorene and its nanostructures. *Critical Reviews in Solid State and Materials Sciences*, 42(1):1–82. doi:10.1080/10408436.2016.1182469.

[93] Hultgren, R., Gingrich, N. S., and Warren, B. E. (1935). The atomic distribution in red and black phosphorus and the crystal structure of black phosphorus. *The Journal of Chemical Physics*, 3(6):351–355. doi:10.1063/1.1749671.

[94] Novoselov, K. S., Geim, A. K., Morozov, S. V., Jiang, D., Katsnelson, M. I., Grigorieva, I. V., Dubonos, S. V., and Firsov, A. A. (2005). Two-dimensional gas of massless dirac fermions in graphene. *Nature*, 438:197–200. doi:10.1038/nature04233.

[95] Duan, X., Wang, C., Pan, A., Yu, R., and Duan, X. (2015). Two-dimensional transition metal dichalcogenides as atomically thin semiconductors: opportunities and challenges. *Chem. Soc. Rev.*, 44:8859–8876. doi:10.1039/C5CS00507H.

[96] Island, J. and Castellanos-Gomez, A. (2016). Chapter seven - black phosphorus-based nanodevices. In Iacopi, F., Boeckl, J. J., and Jagadish, C., editors, *2D Materials*, volume 95 of *Semiconductors and Semimetals*, pages 279–303. Elsevier.

[97] Asahina, H. and Morita, A. (1984). Band structure and optical properties of black phosphorus. *Journal of Physics C: Solid State Physics*, 17(11):1839–1852. doi:10.1088/0022-3719/17/11/006.

[98] Cai, Y., Zhang, G., and Zhang, Y. W. (2014). Layer-dependent band alignment and work function of few-layer phosphorene. *Scientific Reports*, 4. doi:10.1038/srep06677.

[99] Tran, V., Soklaski, R., Liang, Y., and Yang, L. (2014). Layer-controlled band gap and anisotropic excitons in few-layer black phosphorus. *Phys. Rev. B*, 89:235319. doi:10.1103/PhysRevB.89.235319.

[100] Carvalho, A., Wang, M., Zhu, X., Rodin, A. S., Su, H., and Neto, A. H. C. (2016). Phosphorene: From theory to applications. *Nature Reviews Materials*, 1. doi:10.1038/natrevmats.2016.61.

[101] Qiao, J., Kong, X., Hu, Z. X., Yang, F., and Ji, W. (2014). High-mobility transport anisotropy and linear dichroism in few-layer black phosphorus. *Nature Communications*, 5. doi:10.1038/ncomms5475.

[102] Marangoni, V. S., Cadore, A. R., Ribeiro, H. B., Hostert, L., de Matos, C. J., Silva, C. C., Seixas, L., and Maroneze, C. M. (2021). Long-term environmental stability of nitrogen-healed black phosphorus. *Applied Surface Science*, 564:150450. doi:https://doi.org/10.1016/j.apsusc.2021.150450.

[103] Pei, J., Gai, X., Yang, J., Wang, X., Yu, Z., Choi, D. Y., Luther-Davies, B., and Lu, Y. (2016). Producing air-stable monolayers of phosphorene and their defect engineering. *Nature Communications*, 7. doi:10.1038/ncomms10450.

[104] Wang, N., Liu, H., Zhou, X., Luo, Q., Yang, X., Yang, H., Shu, H., Xu, H., Zhang, Q., Hildebrandt, D., Liu, X., Qiao, S., Liu, B., and Feng, Q. (2022). Improving harsh environmental stability of few-layer black phosphorus by local charge transfer. *Advanced Functional Materials*, 32(34):2203967. doi:https://doi.org/10.1002/adfm.202203967.

[105] Jain, R., Singh, Y., Cho, S.-Y., Sasikala, S. P., Koo, S. H., Narayan, R., Jung, H.-T., Jung, Y., and Kim, S. O. (2019). Ambient stabilization of few layer phosphorene via noncovalent functionalization with surfactants: Systematic 2d nmr characterization in aqueous dispersion. *Chemistry of Materials*, 31(8):2786–2794. doi:10.1021/acs.chemmater.8b04984.

[106] Wood, J. D., Wells, S. A., Jariwala, D., Chen, K. S., Cho, E., Sangwan, V. K., Liu, X., Lauhon, L. J., Marks, T. J., and Hersam, M. C. (2014). Effective passivation of exfoliated black phosphorus transistors against ambient degradation. *Nano Letters*, 14:6964–6970. doi:10.1021/nl5032293.

[107] Ryder, C. R., Wood, J. D., Wells, S. A., Yang, Y., Jariwala, D., Marks, T. J., Schatz, G. C., and Hersam, M. C. (2016). Covalent functionalization and passivation of exfoliated black phosphorus via aryl diazonium chemistry. *Nature Chemistry*, 8:597–602. doi:10.1038/nchem.2505.

[108] Li, Q., Zhou, Q., Niu, X., Zhao, Y., Chen, Q., and Wang, J. (2016). Covalent functionalization of black phosphorus from first-principles. *Journal of Physical Chemistry Letters*, 7:4540–4546. doi:10.1021/acs.jpclett.6b02192.

[109] Chen, L., Luo, S.-M., Huo, C.-M., Shi, Y.-F., Feng, J., Zhu, J.-Y., Xue, W., and Qiu, X. (2022). New insight into lignin aggregation guiding efficient synthesis and functionalization of a lignin nanosphere with excellent performance. *Green Chem.*, 24:285–294. doi:10.1039/D1GC03651C.

[110] Aladpoosh, R. and Montazer, M. (2022). Functionalization of cellulose fibers alongside growth of 2d ldh platelets through urea hydrolysis inspired taro wettability. *Carbohydrate Polymers*, 275:118584. doi:https://doi.org/10.1016/j.carbpol.2021.118584.

[111] Ibragimova, R., Erhart, P., Rinke, P., and Komsa, H.-P. (2021). Surface functionalization of 2d mxenes: Trends in distribution, composition, and elec-

tronic properties. *The Journal of Physical Chemistry Letters*, 12(9):2377–2384. doi:10.1021/acs.jpclett.0c03710, PMID: 33657317.

[112] Tuček, J., Błoński, P., Ugolotti, J., Swain, A. K., Enoki, T., and Zbořil, R. (2018). Emerging chemical strategies for imprinting magnetism in graphene and related 2d materials for spintronic and biomedical applications. *Chemical Society Reviews*, 47:3899–3990. doi:10.1039/c7cs00288b.

[113] Reed-Lingenfelter, S. N., Wang, M., Williams, N. L., and Cha, J. J. (2022). Surface functionalization for magnetic property tuning of nonmagnetic 2d materials. *Advanced Materials Interfaces*, 9(3):2100463. doi:https://doi.org/10.1002/admi.202100463.

[114] Jeong, J. H., Kang, S., Kim, N., Joshi, R., and Lee, G.-H. (2022). Recent trends in covalent functionalization of 2d materials. *Phys. Chem. Chem. Phys.*, 24:10684–10711. doi:10.1039/D1CP04831G.

[115] Hirohata, A., Yamada, K., Nakatani, Y., Prejbeanu, I.-L., Diény, B., Pirro, P., and Hillebrands, B. (2020). Review on spintronics: Principles and device applications. *Journal of Magnetism and Magnetic Materials*, 509:166711. doi:https://doi.org/10.1016/j.jmmm.2020.166711.

[116] Li, X. and Yang, J. (2013). Bipolar magnetic materials for electrical manipulation of spin-polarization orientation. *Physical Chemistry Chemical Physics*, 15:15793–15801. doi:10.1039/c3cp52623b.

[117] Li, J., Li, X., and Yang, J. (2022). A review of bipolar magnetic semiconductors from theoretical aspects. *Fundamental Research*, 2(4):511–521. doi:https://doi.org/10.1016/j.fmre.2022.04.002.

[118] Li, X., Wu, X., Li, Z., Yang, J., and Hou, J. G. (2012). Bipolar magnetic semiconductors: A new class of spintronics materials. *Nanoscale*, 4:5680–5685. doi:10.1039/c2nr31743e.

[119] Sun, Z., Lv, H., Zhuo, Z., Jalil, A., Zhang, W., Wu, X., and Yang, J. (2018). A new phase of the two-dimensional res2 sheet with tunable magnetism. *Journal of Materials Chemistry C*, 6(5):1248 – 1254. doi:10.1039/c7tc05303g, Cited by: 24.

[120] Zhang, J., Zhao, B., Ma, C., and Yang, Z. (2021). Bipolar ferromagnetic semiconductors and doping-tuned room-temperature half-metallicity in monolayer mox3 (x=cl, br, i): An hse06 study bipolar ferromagnetic semiconductors and ... zhang, zhao, ma, and yang. *Physical Review B*, 103(7). doi:10.1103/PhysRevB.103.075433, Cited by: 8.

[121] ming Zhang, J., zhuang Nie, Y., lin Xia, Q., Xiong, R., and hua Guo, G. (2019). Electronic structures and magnetic properties of cr-site3 single-layer nanoribbons. *Physics Letters A*, 383(19):2346–2351. doi:https://doi.org/10.1016/j.physleta.2019.04.049.

[122] Tan, X., Liu, L., Xiang, H., Du, G.-F., Lou, A., and Fu, H.-H. (2020). One-dimensional transition metal dihalide nanowires as robust bipolar magnetic semiconductors. *Nanoscale*, 12:8942–8948. doi:10.1039/C9NR10849A.

[123] Pan, H., Sun, Y., Zheng, Y., Tang, N., and Du, Y. (2016). $B_4cn_3$and b_3cn_4 monolayers as the promising candidates for metal-free spintronic materials. *New Journal of Physics*, 18(9):093021. doi:10.1088/1367-2630/18/9/093021.

[124] Zhang, S., Zhang, X., Li, M., Zeng, B., Duan, H., Zhang, D., and Long, M. (2018). Study on the electronic structures and transport properties of the polyporphyrin nanoribbons with different edge configurations. *Physics Letters A*, 382(38):2769–2775. doi:https://doi.org/10.1016/j.physleta.2018.07.046.

[125] Guan, Z., Wang, J., Huang, J., Wu, X., Li, Q., and Yang, J. (2014). Metal-free magnetism and half-metallicity of carbon nitride nanotubes: A first-principles study. *The Journal of Physical Chemistry C*, 118(39):22491–22498. doi:10.1021/jp508617k.

[126] Hong-Cai, Z., Jeffrey R., L., and Omar M., Y. (2012). Introduction to metal–organic frameworks. *Chemical Reviews*, 112(2):673–674. doi:10.1021/cr300014x, PMID: 22280456.

[127] Chen, Y., Liu, J., Sun, Q., Kawazoe, Y., and Jena, P. (2018). Bipolar magnetic materials based on 2d ni[tcne] metal–organic coordination networks. *Advanced Electronic Materials*, 4(2):1700323. doi:https://doi.org/10.1002/aelm.201700323.

[128] Wang, P., Jiang, X., Hu, J., Wang, B., Zhou, T., Yuan, H., and Zhao, J. (2020). Robust spin manipulation in 2d organometallic kagome lattices: a first-principles study. *Phys. Chem. Chem. Phys.*, 22:11045–11052. doi:10.1039/D0CP00742K.

[129] Giannozzi, P., Baroni, S., Bonini, N., Calandra, M., Car, R., Cavazzoni, C., Ceresoli, D., Chiarotti, G. L., Cococcioni, M., Dabo, I., Corso, A. D., de Gironcoli, S., Fabris, S., Fratesi, G., Gebauer, R., Gerstmann, U., Gougoussis, C., Kokalj, A., Lazzeri, M., Martin-Samos, L., Marzari, N., Mauri, F., Mazzarello, R., Paolini, S., Pasquarello, A., Paulatto, L., Sbraccia, C., Scandolo,

S., Sclauzero, G., Seitsonen, A. P., Smogunov, A., Umari, P., and Wentzcovitch, R. M. (2009). QUANTUM ESPRESSO: a modular and open-source software project for quantum simulations of materials. *Journal of Physics: Condensed Matter*, 21(39):395502. doi:10.1088/0953-8984/21/39/395502.

[130] Perdew, J. P., Burke, K., and Ernzerhof, M. (1996). Generalized gradient approximation made simple. *Phys. Rev. Lett.*, 77:3865–3868. doi:10.1103/PhysRevLett.77.3865.

[131] Prandini, G., Marrazzo, A., Castelli, I. E., Mounet, N., and Marzari, N. (2018). Precision and efficiency in solid-state pseudopotential calculations. *npj Computational Materials*, 4. doi:10.1038/s41524-018-0127-2.

[132] Monkhorst, H. J. and Pack, J. D. (1976). Special points for brillonin-zone integrations*. *Physical Review B*, 13:5188–5192.

[133] Jeong, J. H., Kang, S., Kim, N., Joshi, R., and Lee, G.-H. (2022). Recent trends in covalent functionalization of 2d materials. *Phys. Chem. Chem. Phys.*, 24:10684–10711. doi:10.1039/D1CP04831G.

[134] Mondal, P. C., Fontanesi, C., Waldeck, D. H., and Naaman, R. (2016). Spin-dependent transport through chiral molecules studied by spin-dependent electrochemistry. *Accounts of Chemical Research*, 49:2560–2568. doi:10.1021/acs.accounts.6b00446.

[135] Pal, C. and Majumder, S. (2022). Manipulating electron-spin polarization using cysteine–dna chiral conjugates. *The Journal of Chemical Physics*, 156(16):164704. doi:10.1063/5.0088346.

[136] Xiao, J., Long, M., Zhang, X., Zhang, D., Xu, H., and Chan, K. S. (2015). First-principles prediction of the charge mobility in black phosphorus semiconductor nanoribbons. *Journal of Physical Chemistry Letters*, 6:4141–4147. doi:10.1021/acs.jpclett.5b01644.

[137] Fei, R. and Yang, L. (2014). Strain-engineering the anisotropic electrical conductance of few-layer black phosphorus. *Nano Letters*, 14:2884–2889. doi:10.1021/nl500935z.

[138] Ledur, C. M., Zanella, I., and Fagan, S. B. (2021). Ab initio simulations of black and blue phosphorene functionalised with chemical groups for biomolecule anchoring. *Journal of Molecular Modeling*, 27. doi:10.1007/s00894-021-04961-4.

[139] Tuček, J., Holá, K., Bourlinos, A. B., Błoński, P., Bakandritsos, A., Ugolotti, J., Dubecký, M., Karlický, F., Ranc, V., Čépe, K., Otyepka, M., and Zbořil, R. (2017). Room temperature organic magnets derived from sp3 functionalized graphene. *Nature Communications*, 8. doi:10.1038/ncomms14525.

[140] Li, J., Cui, R., Chang, Y., Huang, H., Guo, X., Wang, J., Liu, R., Chen, K., Kong, J., Xing, G., and Sun, B. (2020). Preparing dangling bonds by nanoholes on graphene oxide nanosheets and their enhanced magnetism. *RSC Adv.*, 10:36378–36385. doi:10.1039/D0RA05945E.

[141] Song, L. L., Zheng, X. H., Wang, R. L., and Zeng, Z. (2010). Dangling bond states, edge magnetism, and edge reconstruction in pristine and b/n-terminated zigzag graphene nanoribbons. *Journal of Physical Chemistry C*, 114:12145–12150. doi:10.1021/jp1040025.

[142] Kumari, P., Majumder, S., Rani, S., Nair, A. K., Kumari, K., Kamalakar, M. V., and Ray, S. J. (2020). High efficiency spin filtering in magnetic phosphorene. *Phys. Chem. Chem. Phys.*, 22:5893–5901. doi:10.1039/C9CP05390E.

[143] Rodríguez Méndez, A., Medrano Sandonas, L., Dianat, A., Gutierrez, R., and Cuniberti, G. (2022). Electronic and thermal signatures of phosphorene grain boundaries under uniaxial strain. *Phys. Rev. Mater.*, 6:114003. doi:10.1103/PhysRevMaterials.6.114003.

[144] Gourley, P. L. and Wolfe, J. P. (1978). Spatial condensation of strain-confined excitons and excitonic molecules into an electron-hole liquid in silicon. *Phys. Rev. Lett.*, 40:526–530. doi:10.1103/PhysRevLett.40.526.

[145] Lin, J. L. and Wolfe, J. P. (1993). Bose-einstein condensation of paraexcitons in stressed cu_2o. *Phys. Rev. Lett.*, 71:1222–1225. doi:10.1103/PhysRevLett.71.1222.

[146] Li, J., Shan, Z., and Ma, E. (2014). Elastic strain engineering for unprecedented materials properties. *MRS Bulletin*, 39:108–114. doi:10.1557/mrs.2014.3.

[147] Kim, J. M., Haque, M. F., Hsieh, E. Y., Nahid, S. M., Zarin, I., Jeong, K.-Y., So, J.-P., Park, H.-G., and Nam, S. (2022). Strain engineering of low-dimensional materials for emerging quantum phenomena and functionalities. *Advanced Materials*, n/a(n/a):2107362. doi:https://doi.org/10.1002/adma.202107362.

[148] Cocco, G., Cadelano, E., and Colombo, L. (2010). Gap opening in graphene by shear strain. *Phys. Rev. B*, 81:241412. doi:10.1103/PhysRevB.81.241412.

[149] Li, M.-Y., Shi, Y., Cheng, C.-C., Lu, L.-S., Lin, Y.-C., Tang, H.-L., Tsai, M.-L., Chu, C.-W., Wei, K.-H., He, J.-H., Chang, W.-H., Suenaga, K., and Li, L.-J. (2015). Epitaxial growth of a monolayer wse₂-mos₂ lateral p-n junction with an atomically sharp interface. *Science*, 349(6247):524–528. doi:10.1126/science.aab4097.

[150] Yang, S., Wang, C., Sahin, H., Chen, H., Li, Y., Li, S.-S., Suslu, A., Peeters, F. M., Liu, Q., Li, J., and Tongay, S. (2015). Tuning the optical, magnetic, and electrical properties of rese2 by nanoscale strain engineering. *Nano Letters*, 15(3):1660–1666. doi:10.1021/nl504276u, PMID: 25642738.

[151] Scalise, E., Houssa, M., Pourtois, G., Afanas'ev, V., and Stesmans, A. (2012). Strain-induced semiconductor to metal transition in the two-dimensional honeycomb structure of mos2. *Nano Research*, 5:43–48. doi:10.1007/s12274-011-0183-0.

[152] Deng, S., Che, S., Debbarma, R., and Berry, V. (2019). Strain in a single wrinkle on an mos2 flake for in-plane realignment of band structure for enhanced photo-response. *Nanoscale*, 11:504–511. doi:10.1039/C8NR05884A.

[153] Raeisi, M., Ahmadi, S., and Rajabpour, A. (2019). Modulated thermal conductivity of 2d hexagonal boron arsenide: a strain engineering study. *Nanoscale*, 11:21799–21810. doi:10.1039/C9NR06283A.

[154] Nakagawa, K., Satoh, K., Murakami, S., Takei, K., Akita, S., and Arie, T. (2021). Controlling the thermal conductivity of multilayer graphene by strain. *Sci. Rep.*, 11:19533. doi:10.1038/s41598-021-98974-x.

[155] Sandonas, L. M., Gutierrez, R., Pecchia, A., Seifert, G., and Cuniberti, G. (2017). Tuning quantum electron and phonon transport in two-dimensional materials by strain engineering: a green's function based study. *Phys. Chem. Chem. Phys.*, 19:1487–1495. doi:10.1039/C6CP06621F.

[156] Wang, Q., Han, L., Wu, L., Zhang, T., Li, S., and Lu, P. (2019). Strain effect on thermoelectric performance of inse monolayer. *Nanoscale Research Letters*, 14. doi:10.1186/s11671-019-3113-9.

[157] Wong, Z. M., Deng, T., Shi, W., Wu, G., and Yang, S.-W. (2020). Strain effects on the n-type thermoelectric performance of the small-molecule organic

semiconductor 2-5-difluoro-7,7,8,8-tetracyanoquinodimethane. *ACS Applied Energy Materials*, 3(10):10174–10182. doi:10.1021/acsaem.0c01875.

[158] Yang, S.-J., Choi, M.-Y., and Kim, C.-J. (2022). Engineering grain boundaries in two-dimensional electronic materials. *Advanced Materials*, n/a(n/a):2203425. doi:https://doi.org/10.1002/adma.202203425.

[159] Randle, V. (2001). Grain boundary geometry: Measurement. In Buschow, K. J., Cahn, R. W., Flemings, M. C., Ilschner, B., Kramer, E. J., Mahajan, S., and Veyssière, P., editors, *Encyclopedia of Materials: Science and Technology*, pages 3618–3622. Elsevier, Oxford.

[160] Gargiulo, F. (2021). Electronic transport across realistic grain boundaries in graphene. unpublished.

[161] Khalkhali, M., Rajabpour, A., and Khoeini, F. (2019). Thermal transport across grain boundaries in polycrystalline silicene: A multiscale modeling. *Sci. Rep.*, 9:5684. doi:10.1038/s41598-019-42187-w.

[162] Sun, J., Leng, J., and Zhang, G. (2020). The grain boundary effect on mechanical and electronic transport properties of a striped borophene. *Phys. Chem. Chem. Phys.*, 22:21844–21850. doi:10.1039/d0cp04387g.

[163] Guo, Y., Zhou, S., Zhang, J., Bai, Y., and Zhao, J. (2016). Atomic structures and electronic properties of phosphorene grain boundaries. *2D Mater.*, 3:025008. doi:10.1088/2053-1583/3/2/025008.

[164] Zhu, Z.-L., Yu, W.-Y., Ren, X.-Y., Sun, Q., and Jia, Y. (2015). Grain boundary in phosphorene and its unique roles on c and o doping. *EPL*, 109(4):47003. doi:10.1209/0295-5075/109/47003.

[165] Liu, Y., Xu, F., Zhang, Z., Penev, E. S., and Yakobson, B. I. (2014). Two-dimensional mono-elemental semiconductor with electronically inactive defects: The case of phosphorus. *Nano Lett.*, 14:6782–6786. doi:10.1021/nl5021393.

[166] Sorkin, V. and Zhang, Y. W. (2017). Mechanical properties and failure behavior of phosphorene with grain boundaries. *Nanotechnology*, 28(7):075704. doi:10.1088/1361-6528/aa537b.

[167] Guo, Y., Qiao, C., Wang, A., Zhang, J., Wang, S., Su, W.-S., and Jia, Y. (2016). The fracture behaviors of monolayer phosphorene with grain boundaries under tension: a molecular dynamics study. *Phys. Chem. Chem. Phys.*, 18:20562–20570. doi:10.1039/C6CP03655D.

[168] Wang, X., Wang, Q., Liu, X., Huang, Z., and Liu, X. (2022). Phosphorene grain boundary effect on phonon transport and phononic applications. *Nanotechnology*, 33(26):265704. doi:10.1088/1361-6528/ac60db.

[169] Liu, X., Gao, J., Zhang, G., Zhao, J., and Zhang, Y. W. (2020). Remarkable role of grain boundaries in the thermal transport properties of phosphorene. *ACS Omega*, 5:17416–17422. doi:10.1021/acsomega.0c01806.

[170] Kumar, S. B. and Guo, J. (2012). Strain-induced conductance modulation in graphene grain boundary. *Nano Lett.*, 12:1362–1366. doi:10.1021/nl203968j.

[171] Liu, Y., Zou, X., and Yakobson, B. I. (2012). Dislocations and grain boundaries in two-dimensional boron nitride. *ACS Nano*, 6:7053–7058. doi:10.1021/nn302099q.

[172] Zhou, W., Zou, X., Najmaei, S., Liu, Z., Shi, Y., Kong, J., Lou, J., Ajayan, P. M., Yakobson, B. I., and Idrobo, J. C. (2013). Intrinsic structural defects in monolayer molybdenum disulfide. *Nano Lett.*, 13:2615–2622. doi:10.1021/nl4007479.

[173] Aradi, B., Hourahine, B., and Frauenheim, T. (2007). Dftb+, a sparse matrix-based implementation of the dftb method. *J. Phys. Chem. A*, 111:5678–5684. doi:10.1021/jp070186p.

[174] He, C., Liu, G., Zhang, W. X., Shi, Z. Q., and Zhou, S. L. (2015). Tuning the structures and electron transport properties of ultrathin cu nanowires by size and bending stress using dft and dftb methods. *RSC Adv.*, 5:22463–22470. doi:10.1039/C4RA15051A.

[175] Pecchia, A., Latessa, L., Di Carlo, A., Lugli, P., and Neihaus, T. (2003). Electronic transport properties of molecular devices. *Physica E Low Dimens. Syst. Nanostruct.*, 19(1):139–144. doi:https://doi.org/10.1016/S1386-9477(03)00300-X, Fourth International Symposium on Nanostructures and Mesoscopic Systems.

[176] Gaus, M., Cui, Q., and Elstner, M. (2011). Dftb3: Extension of the self-consistent-charge density-functional tight-binding method (scc-dftb). *J. Chem. Theory Comput.*, 7:931–948. doi:10.1021/ct100684s.

[177] Snyder, G. J. and Snyder, A. H. (2017). Figure of merit zt of a thermoelectric device defined from materials properties. *Energy Environ. Sci.*, 10:2280–2283. doi:10.1039/C7EE02007D.

[178] Pecchia, A., Penazzi, G., Salvucci, L., and Carlo, A. D. (2008). Non-equilibrium green's functions in density functional tight binding: method and applications. *New J. Phys.*, 10(6):065022. doi:10.1088/1367-2630/10/6/065022.

[179] Medrano Sandonas, L., Gutierrez, R., Pecchia, A., Croy, A., and Cuniberti, G. (2019). Quantum phonon transport in nanomaterials: Combining atomistic with non-equilibrium green's function techniques. *Entropy*, 21(8):735. doi:10.3390/e21080735.

[180] Yazyev, O. V. and Louie, S. G. (2010). Topological defects in graphene: Dislocations and grain boundaries. *Phys. Rev. B*, 81:195420. doi:10.1103/PhysRevB.81.195420.

[181] Nakanishi, T., Yoshida, S., Murase, K., Takeuchi, O., Taniguchi, T., Watanabe, K., Shigekawa, H., Kobayashi, Y., Miyata, Y., Shinohara, H., and Kitaura, R. (2019). The atomic and electronic structure of 0° and 60° grain boundaries in mos2. *Front. Phys.*, 7:59. doi:10.3389/fphy.2019.00059.

[182] Lu, Y. and Guo, J. (2010). Band gap of strained graphene nanoribbons. *Nano Res.*, 3:189–199. doi:10.1007/s12274-010-1022-4.

[183] Ri, N.-C., Kim, J.-C., and Ri, S.-I. (2021). Effect of strain on mechanical, electronic, and transport properties of hybrid armchair graphane/graphene/fluorographane nanoribbon. *Chem. Phys. Lett.*, 765:138311. doi:https://doi.org/10.1016/j.cplett.2020.138311.

[184] Zhang, Y., Wu, X., Li, Q., and Yang, J. (2012). Linear band-gap modulation of graphane nanoribbons under uniaxial elastic strain: A density functional theory study. *J. Phys. Chem. C*, 116:9356–9359. doi:10.1021/jp301691z.

[185] Zhang, Q. G., Zhang, X., Cao, B. Y., Fujii, M., Takahashi, K., and Ikuta, T. (2006). Influence of grain boundary scattering on the electrical properties of platinum nanofilms. *Appl. Phys. Lett.*, 89(11):114102. doi:10.1063/1.2338885.

[186] Wang, F., Kinloch, I. A., Wolverson, D., Tenne, R., Zak, A., O'Connell, E., Bangert, U., and Young, R. J. (2016). Strain-induced phonon shifts in tungsten disulfide nanoplatelets and nanotubes. *2d Mater.*, 4(1):015007. doi:10.1088/2053-1583/4/1/015007.

[187] Medrano Sandonas, L., Teich, D., Gutierrez, R., Lorenz, T., Pecchia, A., Seifert, G., and Cuniberti, G. (2016). Anisotropic thermoelectric response in

two-dimensional puckered structures. *J. Phys. Chem. C*, 120(33):18841–18849. doi:10.1021/acs.jpcc.6b04969.

[188] Rodríguez Méndez, A., Medrano Sandonas, L., Dianat, A., Gutierrez, R., and Cuniberti, G. (2021). An atomistic study of the thermoelectric signatures of cnt peapods. *The Journal of Physical Chemistry C*, 125(25):13721–13731. doi:10.1021/acs.jpcc.1c02611.

[189] Hirsch, A. (2010). The era of carbon allotropes. *Nature Materials*, 9:868–871. doi:10.1038/nmat2885.

[190] Karfunkel, H. R. and Dressler, T. (1992). New hypothetical carbon allotropes of remarkable stability estimated by mndo solid-state scf computations. *Journal of the American Chemical Society*, 114(7):2285–2288. doi:10.1021/ja00033a001.

[191] Diederich, F. and Rubin, Y. (1992). Synthetic approaches toward molecular and polymeric carbon allotropes. *Angewandte Chemie International Edition in English*, 31(9):1101–1123. doi:https://doi.org/10.1002/anie.199211013.

[192] Allen, M. J., Tung, V. C., and Kaner, R. B. (2010). Honeycomb carbon: A review of graphene. *Chemical Reviews*, 110(1):132–145. doi:10.1021/cr900070d, PMID: 19610631.

[193] Rathinavel, S., Priyadharshini, K., and Panda, D. (2021). A review on carbon nanotube: An overview of synthesis, properties, functionalization, characterization, and the application. *Materials Science and Engineering: B*, 268:115095. doi:https://doi.org/10.1016/j.mseb.2021.115095.

[194] Acquah, S. F. A., Penkova, A. V., Markelov, D. A., Semisalova, A. S., Leonhardt, B. E., and Magi, J. M. (2017). Review—the beautiful molecule: 30 years of c60 and its derivatives. *ECS Journal of Solid State Science and Technology*, 6(6):M3155. doi:10.1149/2.0271706jss.

[195] Baughman, R. H., Eckhardt, H., and Kertesz, M. (1987). Structure-property predictions for new planar forms of carbon: Layered phases containing sp2 and sp atoms. *The Journal of Chemical Physics*, 87(11):6687–6699. doi:10.1063/1.453405.

[196] Desyatkin, V. G., Martin, W. B., Aliev, A. E., Chapman, N. E., Fonseca, A. F., Galvão, D. S., Miller, E. R., Stone, K. H., Wang, Z., Zakhidov, D., Limpoco, F. T., Almahdali, S. R., Parker, S. M., Baughman, R. H., and Rodionov, V. O. (2022). Scalable synthesis and characterization of multilayer

γ-graphyne, new carbon crystals with a small direct band gap. *Journal of the American Chemical Society*, 144(39):17999–18008. doi:10.1021/jacs.2c06583, PMID: 36130080.

[197] Kroto, H. W., Heath, J. R., O'Brien, S. C., Curl, R. F., and Smalley, R. E. (1985). C60: Buckminsterfullerene. *Nature*, 318:162–163. doi:https://doi.org/10.1038/318162a0.

[198] Iijima, S. (1991). Helical microtubules of graphitic carbon. *Nature*, 354:56–58. doi:doi.org/10.1038/354056a0.

[199] Iijima, S. and Ichihashi, T. (1993). Single-shell carbon nanotubes of 1-nm diameter. *Nature*, 363:603–605. doi:https://doi.org/10.1038/363603a0.

[200] Odom, T. W., Huang, J.-L., Kim, P., and Lieber, C. M. (2000). Structure and electronic properties of carbon nanotubes. *The Journal of Physical Chemistry B*, 104(13):2794–2809. doi:10.1021/jp993592k.

[201] Van Hove, L. (1953). The occurrence of singularities in the elastic frequency distribution of a crystal. *Phys. Rev.*, 89:1189–1193. doi:10.1103/PhysRev.89.1189.

[202] DAI, H., JAVEY, A., POP, E., MANN, D., KIM, W., and LU, Y. (2006). Electrical transport properties and field effect transistors of carbon nanotubes. *Nano*, 01(01):1–13. doi:10.1142/S1793292006000070.

[203] Pop, E., Mann, D., Wang, Q., Goodson, K., and Dai, H. (2006). Thermal conductance of an individual single-wall carbon nanotube above room temperature. *Nano Letters*, 6(1):96–100. doi:10.1021/nl052145f, PMID: 16402794.

[204] Rao, R., Pint, C. L., Islam, A. E., Weatherup, R. S., Hofmann, S., Meshot, E. R., Wu, F., Zhou, C., Dee, N., Amama, P. B., Carpena-Nuñez, J., Shi, W., Plata, D. L., Penev, E. S., Yakobson, B. I., Balbuena, P. B., Bichara, C., Futaba, D. N., Noda, S., Shin, H., Kim, K. S., Simard, B., Mirri, F., Pasquali, M., Fornasiero, F., Kauppinen, E. I., Arnold, M., Cola, B. A., Nikolaev, P., Arepalli, S., Cheng, H.-M., Zakharov, D. N., Stach, E. A., Zhang, J., Wei, F., Terrones, M., Geohegan, D. B., Maruyama, B., Maruyama, S., Li, Y., Adams, W. W., and Hart, A. J. (2018). Carbon nanotubes and related nanomaterials: Critical advances and challenges for synthesis toward mainstream commercial applications. *ACS Nano*, 12(12):11756–11784. doi:10.1021/acsnano.8b06511, PMID: 30516055.

[205] Chen, Z., Appenzeller, J., Knoch, J., Lin, Y.-m., and Avouris, P. (2005). The role of metal-nanotube contact in the performance of carbon nanotube field-effect transistors. *Nano Letters*, 5(7):1497–1502. doi:10.1021/nl0508624, PMID: 16178264.

[206] Miyata, Y., Shiozawa, K., Asada, Y., Ohno, Y., Kitaura, R., Mizutani, T., and Shinohara, H. (2011). Length-sorted semiconducting carbon nanotubes for high-mobility thin film transistors. *Nano Research*, 4:963–970. doi:10.1007/s12274-011-0152-7.

[207] Biercuk, M. J., Llaguno, M. C., Radosavljevic, M., Hyun, J. K., Johnson, A. T., and Fischer, J. E. (2002). Carbon nanotube composites for thermal management. *Applied Physics Letters*, 80(15):2767–2769. doi:10.1063/1.1469696.

[208] Manzetti, S. (2013). Molecular and crystal assembly inside the carbon nanotube: Encapsulation and manufacturing approaches. *Adv. Manuf.*, 1(3):198–210. doi:10.1007/s40436-013-0030-5.

[209] Okada, S., Otani, M., and Oshiyama, A. (2003). Electron-state control of carbon nanotubes by space and encapsulated fullerenes. *Phys. Rev. B*, 67:205411. doi:10.1103/PhysRevB.67.205411.

[210] Hornbaker, D. J., Kahng, S. J., Misra, S., Smith, B. W., Johnson, A. T., Mele, E. J., Luzzi, D. E., and Yazdani, A. (2002). Mapping the one-dimensional electronic states of nanotube peapod structures. *Science*, 295(5556):828–831. doi:10.1126/science.1068133.

[211] Vavro, J., Llaguno, M. C., Satishkumar, B. C., Luzzi, D. E., and Fischer, J. E. (2002). Electrical and thermal properties of C60-filled single-wall carbon nanotubes. *Appl. Phys. Lett.*, 80(8):1450–1452. doi:10.1063/1.1452788.

[212] González Noya, E., Srivastava, D., Chernozatonskii, L. A., and Menon, M. (2004). Thermal conductivity of carbon nanotube peapods. *Phys. Rev. B*, 70:115416. doi:10.1103/PhysRevB.70.115416.

[213] Kodama, T., Ohnishi, M., Park, W., Shiga, T., Park, J., Shimada, T., Shinohara, H., Shiomi, J., and Goodson, K. E. (2017). Modulation of thermal and thermoelectric transport in individual carbon nanotubes by fullerene encapsulation. *Nat. Mater.*, 16(9):892–897. doi:10.1038/nmat4946.

[214] Wan, J. and Jiang, J. W. (2018). Modulation of thermal conductivity in single-walled carbon nanotubes by fullerene encapsulation: enhancement or reduction? *Nanoscale*, 10(38):18249–18256. doi:10.1039/c8nr05188g.

[215] Dong, H., Fan, Z., Qian, P., Ala-Nissila, T., and Su, Y. (2020). Thermal conductivity reduction in carbon nanotube by fullerene encapsulation : A molecular dynamics study. *Carbon*, 161:800–808.

[216] Seifert, G. (2007). Tight-binding density functional theory: An approximate Kohn-Sham DFT scheme. *J. Phys. Chem. A*, 111(26):5609–5613. doi:10.1021/jp069056r.

[217] Zhechkov, L., Heine, T., Patchkovskii, S., Seifert, G., and Duarte, H. A. (2005). An efficient a posteriori treatment for dispersion interaction in density-functional-based tight binding. *J. Chem. Theory Comput.*, 1(5):841–847. doi:10.1021/ct050065y.

[218] Rappé, A. K., Casewit, C. J., Colwell, K. S., Goddard, W. A., and Skiff, W. M. (1992). UFF, a Full Periodic Table Force Field for Molecular Mechanics and Molecular Dynamics Simulations. *J. Am. Chem. Soc.*, 114(25):10024–10035. doi:10.1021/ja00051a040.

[219] Caldeweyher, E., Ehlert, S., Hansen, A., Neugebauer, H., Spicher, S., Bannwarth, C., and Grimme, S. (2019). A generally applicable atomic-charge dependent london dispersion correction. *J. Chem. Phys.*, 150(15):154122. doi:10.1063/1.5090222.

[220] Zou, Y., Liu, B., Wang, L., Liu, D., Yu, S., Wang, P., Wang, T., Yao, M., Li, Q., Zou, B., Cui, T., Zou, G., Wågberg, T., Sundqvist, B., and Mao, H.-K. (2009). Rotational dynamics of confined c60 from near-infrared raman studies under high pressure. *PNAS*, 106(52):22135–22138. doi:10.1073/pnas.0911963106.

[221] Nozaki, D., Avdoshenko, S. M., Sevinçli, H., and Cuniberti, G. (2014). Quantum interference in thermoelectric molecular junctions: A toy model perspective. *J. Appl. Phys.*, 116(7):074308–074315. doi:10.1063/1.4893475.

[222] Nozaki, D., Sevinçli, H., Avdoshenko, S. M., Gutierrez, R., and Cuniberti, G. (2013). A parabolic model to control quantum interference in t-shaped molecular junctions. *Phys. Chem. Chem. Phys.*, 15:13951–13958. doi:10.1039/C3CP44578J.

[223] Li, B., Tan, K. T., and Christensen, J. (2018). Heat conduction tuning by hyperbranched nanophononic metamaterials. *J. Appl. Phys.*, 123(20):205105. doi:10.1063/1.5023487.

[224] Anufriev, R. and Nomura, M. (2018). Phonon and heat transport control using pillar-based phononic crystals. *Sci. Technol. Adv. Mater.*, 19(1):863–870. doi:10.1080/14686996.2018.1542524, PMID: 30479674.

[225] Anufriev, R., Gluchko, S., Volz, S., and Nomura, M. (2018). Quasi-ballistic heat conduction due to lévy phonon flights in silicon nanowires. *ACS Nano*, 12(12):11928–11935. doi:10.1021/acsnano.8b07597.

[226] Davis, B. L. and Hussein, M. I. (2014). Nanophononic metamaterial: Thermal conductivity reduction by local resonance. *Phys. Rev. Lett.*, 112(5):055505–055509. doi:10.1103/PhysRevLett.112.055505.

[227] Ma, D., Wan, X., and Yang, N. (2018). Unexpected thermal conductivity enhancement in pillared graphene nanoribbon with isotopic resonance. *Phys. Rev. B*, 98:245420. doi:10.1103/PhysRevB.98.245420.

[228] Nomura, M., Shiomi, J., Shiga, T., and Anufriev, R. (2018). Thermal phonon engineering by tailored nanostructures. *Jpn. J. Appl. Phys*, 57(8):080101. doi:10.7567/jjap.57.080101.

[229] Seol, J. H., Jo, I., Moore, A. L., Lindsay, L., Aitken, Z. H., Pettes, M. T., Li, X., Yao, Z., Huang, R., Broido, D., Mingo, N., Ruoff, R. S., and Shi, L. (2010). Two-dimensional phonon transport in supported graphene. *Science*, 328(5975):213–216. doi:10.1126/science.1184014.

[230] Correa, G. C., Foss, C. J., and Aksamija, Z. (2017). Interface thermal conductance of van der waals monolayers on amorphous substrates. *Nanotechnology*, 28(13):135402. doi:10.1088/1361-6528/aa5e3d.

[231] Zhang, X., Bao, H., and Hu, M. (2015). Bilateral substrate effect on the thermal conductivity of two-dimensional silicon. *Nanoscale*, 7:6014–6022. doi:10.1039/C4NR06523A.

[232] Medrano Sandonas, L., Cuba-Supanta, G., Gutierrez, R., Dianat, A., Landauro, C. V., and Cuniberti, G. (2017). Enhancement of thermal transport properties of asymmetric graphene/hbn nanoribbon heterojunctions by substrate engineering. *Carbon*, 124:642 – 650.

LIST OF PUBLICATIONS

1. **Rodriguez Mendez, A**, Medrano Sandonas, L., Dianat, A., Gutierrez, R., and Cuniberti, G. (2021). An atomistic study of the thermoelectric signatures of cnt peapods. The Journal of Physical Chemistry C, 125(25): 13721–13731.

2. **Rodriguez Mendez, A**, Medrano Sandonas, L., Dianat, A., Gutierrez, R., and Cuniberti, G. (2022). Electronic and thermal signatures of phosphorene grain boundaries under uniaxial strain. Phys. Rev. Mater., 6:114003.

3. **Rodriguez Mendez, A**, Dianat, A., Medrano Sandonas, L., Gutierrez, R., and Cuniberti, G. (2023). Functionalization induced local magnetization in black phosphorene. The Journal of Physical Chemistry C, submitted.

PRESENTATIONS

1. German Physics Society 2019
   Phonon filters in molecular junctions, Regensburg, Germany

2. Conference on Nanophononics, Bridging Statistical Physics, Molecular Modeling and Experiments 2019
   Engineering nanoscale thermal devices: Phonon filter and Ranque-Hilsch vortex tube, Trieste, Italy

3. IMPRS Summer School 2019
   Engineering Nanoscale Thermal Devices: Phonon filter and Ranque-Hilsch Vortex Tube, Karpacz, Poland.

4. Chem2Dmat 2021
   Electronic and Thermal Transport in Black Phosphorene tunned by Grain Boundaries and Strain, Bologne, Italy.

5. German Physics Society 2021
   An Atomistic Study of Thermoelectric Signatures of CNT Peapods, online, Germany.

6. American Physics Society 2022
   In-silico study of the electronic and magnetic properties of Functionalized Phosphorene, Chicago, USA.

7. Max-Planck Institute seminar 2022
   Electronic and Thermal Transport in Phosphorene Grain Boundaries, Dresden, Germany